E-740

Transverse Energy and Cone Size Dependence of the Inclusive Jet Cross Section at a Center-of-Mass Energy of 1.8 TeV

A thesis presented
by
Mrinmoy Bhattacharjee

to

The Department of Physics and Astrophysics

in partial fulfillment of the requirements
for the degree of
Doctor of Philosophy
in the subject of
Physics
University of Delhi
Delhi 110007, India

December, 1996

Abstract

The transverse energy and cone size dependence of the inclusive jet cross section in $p\bar{p}$ collisions at a center-of-mass energy of 1.8 TeV and in the central unit of pseudorapidity ($|\eta| \leq 0.5$) are presented in this thesis. These measurements are based on a $13.7 pb^{-1}$ sample taken during the 1992-93 data run of the DØ experiment at the FNAL Tevatron Collider. Comparisons with Next-to-leading Order (NLO) Quantum Chromodynamics (QCD) are also presented.

Dedicated to my parents,

Neelima and Chandi Charan Bhattacharjee.

Acknowledgement

I consider myself very fortunate for getting a chance to work in a big and excellent experiment like DØ at the Fermi National Accelerator Laboratory. It is a privilege to have been a part of this collaboration. During my three and half or so years of stay at and involvement with the DØ experiment, I have worked with many people. Although it is not possible for me to name everybody, I thank all who worked so hard to build and keep this machine running. This work would not have been possible without their effort and dedication. I thank Prof. Paul D. Grannis and Dr. Hugh Montgomery for the guidance they have given to the experiment as co-spokespersons.

I am specially grateful to my advisor Professor Ram K. Shivpuri, for giving me the chance to work at Fermilab. I am indebted to him for his guidance and help all throughout my days as a graduate student.

During my early days as a graduate student in Delhi, Dr. Sanjeev Soni taught me particle physics. I was very lucky to have been able to work with him and learn from him.

I have learnt a lot from Prof. Gerald C. Blazey. Be it analysis, understanding the data, my thesis, without his help it would have been very hard. I am grateful to him for all the help he extended towards me in all these years. I am also indebted to Dr. Victor D. Elvira. From the very early days, when I started my analysis until today I have learnt a lot from him and it was really a pleasure working with him. All the members of the QCD group were very helpful towards me and I thank all of them for their help. I also thank Soon Yung for the many interesting discussions we had over coffee, and also for his friendly advice.

Also, I would like to take this opportunity to thank all my friends at Fermilab. I will always remember all the lively parties, discussions we had. All of them have helped me in some way or the other during difficult times. I would like to thank all of them, Prem, Prajakta, Sailesh, Balamurali, Ashutosh, Vipin, Shankar, Stayadev, Brajesh, Ajay, Harpreet, keep up the good work guys!

All this work would have not been possible without the love and support of my parents and my sister, Sujata. During this long student life they have always encouraged me. I hope this thesis will make them proud. Finally I would like to thank my wife, Bornali, for her support and understanding all these years.

Contents

List of Tables

List of Figures

Chapter 1

Introduction

What is matter made of? This is a question that has stimulated the minds of human beings since time immemorial. People have tried to answer this question in different ways. The concept of molecules and atoms as the elementary building blocks of nature came in during the late nineteenth and the early twentieth century. Since then, our understanding of elementary particles and their interactions have increased manifold.

At present, our understanding of the elementary particle world and the fundamental forces are most precisely described by the Standard Model of elementary particles first proposed by Salam, Weinberger and Glashow. In this model, all matter is considered to be made up of two types of fundamental particles, the quarks and the leptons. The quarks are spin $\frac{1}{2}$ particles with fractional charge of $+\frac{2}{3}e$ or $-\frac{1}{3}e$, where e is the electron charge. There are six types of quarks. The leptons are also spin $\frac{1}{2}$ particles and they are of six types. The quarks undergo strong and weak interactions while the leptons undergo both electromagnetic and weak interactions. The interactions are transmitted through spin 1 particles known as bosons. The strong force is transmitted through neutral gluons, the electromagnetic force is transmitted through neutral photons, and the weak force is transmitted either through charged W bosons or through neutral Z bosons. In this model all particles have antiparticles.

The complete theory of interaction of quarks and gluons is Quantum Chromodynamics (QCD). One of the consequences of QCD theory is that quarks and gluons do not manifest themselves as free particles. The experimental signatures for quarks and gluons are collimated sprays of hadrons known as jets. The azimuthal angle (ϕ) gives the position of the jet around the beam and the pseudorapidity (η), related to the polar angle (θ), gives the position of the jet in a plane parallel to the beam. Energy of the jet transverse to the beam direction (E_T) along with the two position variables complete the kinematic description of a jet.

Leading Order (LO) or $O(\alpha_s^2)$ QCD gives a fair description of the inclusive jet cross section, $\sigma(p\bar{p} \rightarrow jet + X)$, in central pseudorapidities, $|\eta| \leq 1.0$, and over a wide range of center-of-mass (CMS) energies, 0.063 TeV $< \sqrt{s} <$ 1.8 TeV [1, 2, 3]. However, LO comparisons include a $30 - 50\%$ theoretical normalization uncertainty. Next-to-leading order (NLO) QCD or $O(\alpha_s^3)$ predictions of the inclusive jet cross section [18, 19, 6] reduce theoretical uncertainties to $10 - 20\%$ [3, 8, 7]. At NLO, QCD predicts the inclusive jet cross section decreases with jet cone size, $R=\sqrt{(\delta\eta)^2 + (\delta\phi)^2}$ at a fixed E_T.

Data taken at DØ during the 1992-93 run at the Fermilab Tevatron Collider, corresponding to an integrated luminosity of $13.7pb^{-1}$ can be used to study the dependence of the inclusive jet cross section on jet transverse energy and jet cone size. Jets have been reconstructed with four different cone sizes, R = 1.0, 0.7, 0.5 and 0.3. The cone size dependence of the inclusive jet cross section for $|\eta| \leq 0.5$ and 80 GeV $\leq E_T \leq$ 480 GeV constitutes a new test of NLO QCD.

Chapter 2

Theory

2.1 Introduction

The theory of Quantum Chromodynamics (QCD) predicts the rate of quark and gluon interactions in high energy hadron-hadron collisions. In these high energy hadron-hadron collisions quarks and gluons manifest themselves as highly collimated sprays of particles known as jets. The transverse energy of these jets can reach several hundred GeV. Experimental measurements of the inclusive jet cross section can be used as a direct test of QCD predictions. In this chapter a brief introduction to QCD theory is given, also discussed are the theoretical motivations for measuring the inclusive jet cross section. The available NLO QCD theoretical predictions used for this analysis along with associated uncertainties are described in this chapter.

2.2 The Quark-Parton Model

Until the 1960's the proton was thought to be a point-like particle. Deep inelastic scattering (DIS) experiments ($e + p \rightarrow e + X$) at the Stanford Linear Accelerator (SLAC) showed that the proton is actually composed of hard point-like particles. These particles were named partons by Feynman. Bjorken suggested that at very high energies the proton structure functions (which describes the structure of the proton) are not dependent on momentum transfer squared, Q^2, rather they are only dependent on the parton momentum fraction x [9]. This is known as Bjorken scaling and was experimentally confirmed in a series of experiments at SLAC. Based upon Bjorken scaling it was also predicted that these constituents of the proton carry 1/2 spin, which was also confirmed by DIS experiments [10]. These experiments, which gave the first evidence for the presence of quarks inside protons, are the basis for the naive quark-parton model. The model regards the proton as a collection of point-like partons that can be treated as free particles at high energies.

Many DIS experiments have been performed using e, μ and ν beams as probes and with various targets. These experiments have shown that the sum of momentum of all the charged quarks inside the proton account for only 50% of the total proton momentum. This indicated that protons include neutral partons [11] known as gluons. In the QCD quark-parton model, the proton includes point-like quarks undergoing color interaction through the exchange of gluons.

2.3 Quantum Chromodynamics (QCD) and the Factorization Theorem

Strong interactions are described by a local non-abelian gauge theory of quarks and gluons, in which the gauge group is SU(3) and the gauge boson is the gluon [12]. According to this theory called quantum chromodynamics (QCD), each quark is a triplet under color SU(3). Since SU(3) has eight generators, there are eight gauge vector bosons called gluons. Quarks carry a quantum number called color and gluons carry a combination of one color and one anticolor. Thus, color enters into the theory as a new degree of freedom. Because of this color degree of freedom, the strong forces transmitted through gluons differ considerably from electromagnetic forces.

As in Quantum Electrodynamics (QED), the QCD coupling constant between quarks and gluons, depends on the momentum transfer, Q^2. To low order, the strong coupling,

$\alpha_s(Q^2)$, is given by:

$$\alpha_s(Q^2) = \frac{12\pi}{(33 - 2N_f)log(Q^2/\Lambda_{QCD})}, \tag{2.1}$$

where Λ_{QCD} is a fundamental QCD parameter to be determined experimentally and N_f is the number of quark flavors [11]. Higher order corrections to the quark-gluon coupling causes α_s to diverge. These divergences can be removed by a process called renormalization, which requires definition of the coupling at some arbitrary scale. This arbitrary scale, μ, is known as the renormalization scale and $\alpha_s(\mu^2)$ has a slow dependence on μ. Typically μ is of the scale of the momentum transfer, Q.

As can be seen from Equation 2.1, as Q^2 increases, which is equivalent to a reduction in distance, α_s decreases. In the limit $Q^2 \to \infty$, α_s becomes zero and the effective color charge of the quarks vanish and they behave as free particles. This is called Asymptotic Freedom. Thus in the asymptotic limit, $Q^2 \to \infty$, QCD becomes a perturbative theory. On the other hand, if Q^2 becomes too small, α_s diverges and perturbative QCD breaks down. This leads to confinement of quarks and gluons in colorless hadrons. This is known as color confinement which states that free quarks and gluons can not exist. The limit between color confinement and asymptotic freedom is set by the parameter Λ_{QCD}.

Hadronic collisions involving a hard scattering (high Q^2) can be factorized into two subprocesses. The incoming hadron can be represented as k partons with momentum fractions x_k $(0 \leq x_k \leq 1)$. A short distance process, characterized by a hard scale Q^2 describes the primary hard scattering. Long distance processes characterized by the hadronization scale Λ_{QCD} describes how the scattered partons split from parent hadrons and how final state partons hadronize. This factorization process simplifies the complex hadron collision into several manageable parts [13].

Suppose hadron A collides with another B and produces a hadron h in the following inclusive reaction:

$$A + B \to h + X. \tag{2.2}$$

According to the quark parton model, parton a (b) of hadron A (B) carrying a momentum fraction of x_a (x_b) takes part in the actual scattering. The parton density of parton a (b) in hadron A (B) is given by $f_{a/A}(x_a)$ ($f_{b/B}(x_b)$), the parton density function (pdf). By the factorization theorem, the cross section for this process can obtained by multiplying the cross section for the hard parton-parton scattering, $\sigma(ab \to cX)$:

$$a + b \to c + X, \tag{2.3}$$

by $dx_a f_{a/A}(x_a)$ and $dx_b f_{b/B}(x_b)$, summing over parton and antiparton types a and b and integrating over x_a and x_b. The subsequent hadronization of parton c into hadron h is incorporated through the inclusion of the fragmentation function $D_{h/c}(z)$ which gives the probability of finding hadron h with a momentum fraction z among all hadrons fragmented from parton c. The cross section can be represented as a convolution of one short distance and two long distance processes:

$$\sigma(AB \to hX) = \sum_{a,b} \int dx_a dx_b f_{a/A}(x_a) f_{b/B}(x_b) \sigma(ab \to cX) D_{h/c}(z) dz. \tag{2.4}$$

The short distance portion can be calculated perturbatively, while the long distance part is non-perturbative. The parton distributions and the fragmentation functions are measured experimentally. Factorization is a simple consequence of the quark parton model.

DIS experiments in the Q^2 range of $5 < Q^2 < 800$ GeV^2, allow us to explore the parton densities [11]. Three valance quarks (uud) along with a sea of $q\bar{q}$ pairs and numerous gluons form the proton. The quark densities must satisfy:

$$\int_0^1 [u(x) - \bar{u}(x)] = 2,$$

$$\int_0^1 [d(x) - \bar{d}(x)] = 1,$$

$$\int_0^1 [h(x) - \bar{h}(x)] = 0, \tag{2.5}$$

where, $u(x)$ and $d(x)$ are parton densities for u and d quarks and $h(x)$ is for the sea. As only a 50% of the proton momentum is accounted for by the quark distributions, the remaining 50% must come from neutral particles, the gluons. The gluon distribution functions can be obtained from many processes such as $pp \to \gamma + X$ or $pp \to \psi X$. However, the naive parton model does not describe the full picture. Gluon radiation from quarks, as predicted by QCD provides for the violation of Bjorken scaling [11]. Even at high energies, the pdf's are dependent on both x and Q^2. The Q^2 evolution of the pdf's is given by the Altarelli-Parisi evolution equations [14]. This allows use of the pdf's at Q^2 much higher than 800 GeV^2.

2.4 Jet Production

Jet production was first observed in e^+e^- colliders in 1975. Up to a CM energy of 3 GeV, the dominant final states were resonances, however, at higher energies final state quarks started to appear as back-to-back jets. The first jet events were observed at the SPEAR experiment at CM energies of 6-8 GeV. At 30-40 GeV CM energies at PEP and PETRA, it was found to be the dominant feature of hadron production [12].

In hadron-hadron collisions, jets were first observed at the CERN ISR pp collider at a CM energy of 63 GeV. At the Fermilab Tevatron Collider, protons and antiprotons collide at a CM energy of 1.8 TeV. At these energies, a $p\bar{p}$ interaction at large Q^2 is well described by perturbative QCD [12].

Asymptotic freedom of QCD states that, during a hard collision the quarks and the gluons in the colliding hadrons can be considered as free particles. Thus, the running coupling α_s is small and QCD becomes a perturbative theory. As shown in Fig. 2.1, in a high energy hadron-hadron collision, only a pair of partons from the parent hadrons take part in a hard scattering, the rest of the partons are "spectators". Just after the hard collision, when distances are still small compared to the physical size of the hadron, the scattered partons emit gluons and these gluons produce $q\bar{q}$ pairs. This process is known as parton showering. The parton showering process is considered a part of the hard scattering. These processes can be calculated from first principles by treating QCD as a perturbative theory.

At later times, however, α_s becomes large and color confinement requires the free particles to form bound states. As the scattered partons separate, they are still connected with the partons that did not take part in the hard scattering (spectators) by gluon exchange. In the process of separation, gluons and $q\bar{q}$ pairs are produced. These quarks (antiquarks) along with the quarks and gluons produced in the parton showering process combine to produce hadrons. Since the scattered quarks fly away from each other at high energies they are well separated and hence the regrouping into hadrons take place locally. Thus, the parent partons fragment nearly independently. This process of producing a spray of hadrons from the partons is known as fragmentation or hadronization. Hadronization which follows parton showering is a non-perturbative process and is responsible for the regrouping of quark antiquark pairs into collimated sprays of hadrons called jets. These are the experimental signatures of the hard collision.

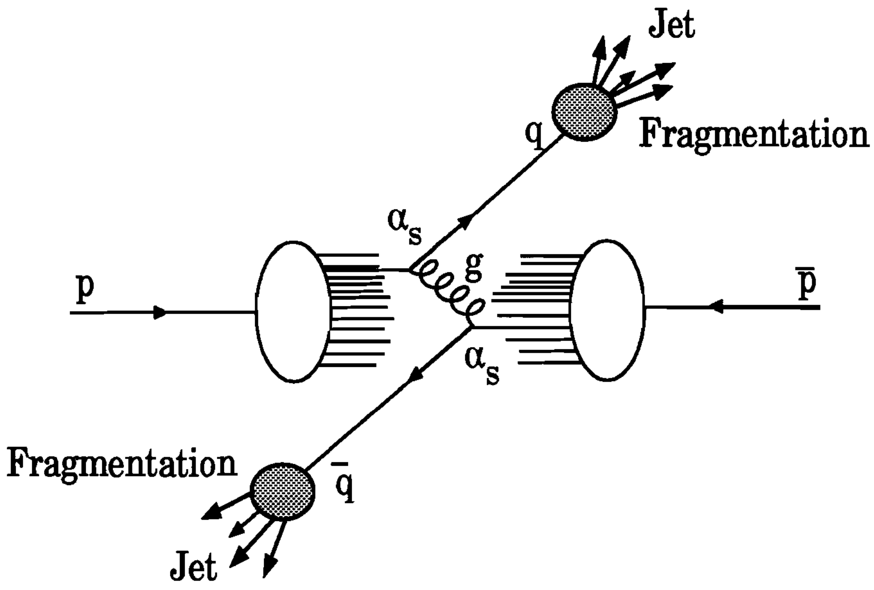

Figure 2.1: Jet production in hadron-hadron collisions.

This non-perturbative part of jet production can not be calculated from first principles, but can be described semi-empirically just as parton distribution functions describe distribution of partons in initial state hadrons. If a parton k of energy E_k produces a hadron h of energy E_h among its other fragmentation products, then the fraction of energy of the parent parton carried by this hadron is given by:

$$z = \frac{E_h}{E_k}, \qquad 0 \leq z \leq 1. \tag{2.6}$$

The probability of finding this hadron in the range z and $z + dz$ is defined to be $D_k^h(z)dz$, with D_k^h known as the fragmentation function, which depend on z only. The cross section for inclusive hadron production is related to the cross section for producing parent partons through D_k^h:

$$\frac{d\sigma}{dE_h}(AB \to hX) = \sum_k \int \frac{d\sigma}{dE_k}(AB \to kX) D_k^h(z) \frac{dE_k}{E_k}, \tag{2.7}$$

since, $dz = E_k^{-1} dE_h$.

Because, the parent partons fragment independently, the properties of a jet depend only on that of the final state parent quark and gluons. Fragmentation affects the momentum distribution of the final state hadrons only and it does not affect the cross section of the process. Integration over the whole phase space of the parent parton fragmentation function should equal unity. The final state jets are therefore direct remnants of the final state partons in a hard scattering and carry information about the parton-parton hard scattering in high energy $p\bar{p}$ collisions.

2.5 Jet Cross Section

A large portion of the cross section in hadron-hadron collisions is due to underlying soft processes which can not be calculated from first principles. But in select kinematic regions, the hard scattering of underlying partons can be compared to perturbative QCD calculations. In soft hadronic processes, the mean particle multiplicity rises logarithmically with the square of the center-of-mass energy (s) and the mean p_T depends very little on s, so the soft cross section for producing a given $\sum p_T$ rises very slowly with s. But in hard parton-parton collisions, the cross section for producing a large $\sum p_T$ of scattered partons rises very rapidly with s, because in each hadron the required momentum fraction becomes smaller and the number of partons with this momentum fraction increases. So parton-parton hard scattering will not only produce jets but also will dominate the cross section for sufficiently large $\sum p_T$ at sufficiently high energies. In calorimeter measurements, p_T is replaced by E_T.

In perturbative QCD, the jet cross section can be expanded to all powers in α_s. The lowest order QCD diagrams, or the Leading Order diagrams, describe parton-parton hard scattering producing two jet (2→2) final states. Some examples of these types of diagrams are shown in Fig. 2.2. These subprocesses contribute $O(\alpha_s^2)$ terms to the cross section. Table 2.1 summarizes all the lowest order subprocesses that contribute to the jet cross section together with their squared matrix elements. Notice gg exchange dominates all other processes.

The total cross section for two jet production in $p\bar{p}$ collisions can be described by an

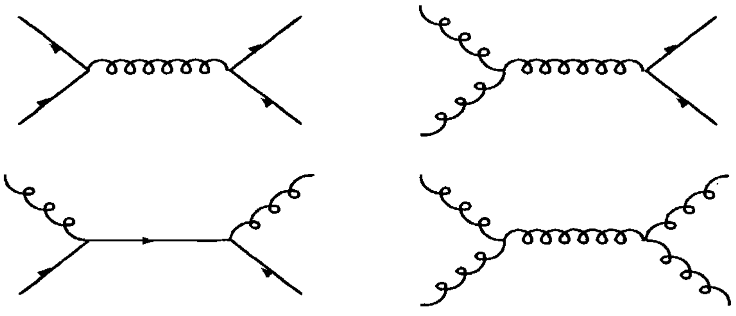

Figure 2.2: Examples of 2→2 subprocesses contributing to jet cross section. The straight lines represent quarks, the curly lines gluons.

application of Equation 2.4:

$$\sigma(p\bar{p} \to 2jets) = \sum_{abcd} \int\int dx_p dx_{\bar{p}} f_{a/p}(x_p) f_{b/\bar{p}}(x_{\bar{p}}) \sigma(ab \to cd), \tag{2.8}$$

where, a, b are the initial state partons and c, d are the final state partons and $\sigma(ab \to cd)$ is the cross section for the subprocess $ab \to cd$. Here, $f_{a/p}$ and $f_{b/\bar{p}}$ are the parton distribution functions giving the probability of finding parton a (b) in a hadron type p ($\bar{p}$) carrying a momentum fraction x_p ($x_{\bar{p}}$).

Higher order QCD subprocesses give more elaborate parton configurations. For example, a gluon may be radiated by an incoming or outgoing parton. Three high p_T partons can be produced by 2→3 subprocesses in QCD, or Next-to-Leading Order QCD calculations, which contribute terms $O(\alpha_s^3)$ to the cross section. The third jet may originate from either the incoming or the outgoing parton. Some Feynman diagrams of 2→3 processes are given in Fig. 2.3. Table 2.2 summarizes all possible 2→3 subprocesses that contribute to the jet cross section.

The total cross section for all 2→3 subprocesses in $p\bar{p}$ collisions is given by:

$$\sigma(p\bar{p} \to 3jets) = \sum_{abcde} \int\int dx_p dx_{\bar{p}} f_{a/p}(x_p) f_{b/\bar{p}}(x_{\bar{p}}) \sigma(ab \to cde). \tag{2.9}$$

The total inclusive jet cross section is given by:

$$\sigma(p\bar{p} \to jet + X) = \sum_{abc} \int\int dx_p dx_{\bar{p}} f_{a/p}(x_p) f_{b/\bar{p}}(x_{\bar{p}}) \sigma(ab \to c + X), \tag{2.10}$$

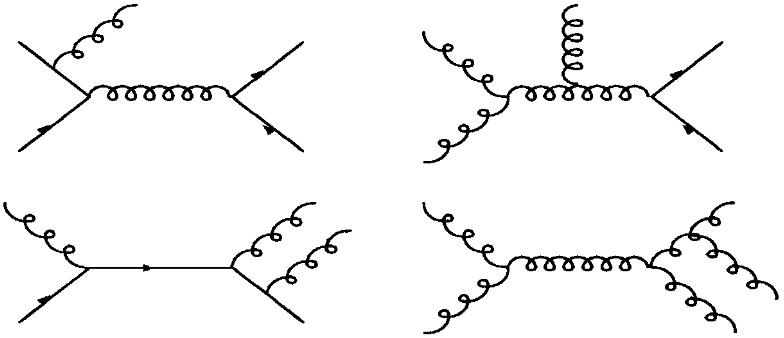

Figure 2.3: Examples of 2→3 subprocesses contributing to jet cross section. The straight lines represent quarks, the curly lines gluons.

where X can be any number and any type of particle, including another jet, produced along with parton c. The LO QCD calculations take into account all the second order terms in α_s, while NLO QCD calculations include all the terms third order in α_s. The theoretical calculation used for this analysis is an order α_s^3 calculation.

Experimentally it is next to impossible to measure the total inclusive jet cross section in $p\bar{p}$ collisions. Jets produced near the beam pipe are lost because of limited detector coverage in the forward pseudorapidities. Also, there is a large contribution from low E_T jets to the jet cross section which are very hard to measure due to trigger and reconstruction inefficiencies. Also, at low E_T there is contamination from soft processes. However, the differential inclusive jet cross section averaged over a restricted range in η and E_T can be measured and is defined as:

$$\frac{d^2\sigma}{dE_T d\eta}(p\bar{p} \to jet + X). \tag{2.11}$$

The experimentally measured differential jet cross section can be compared to available NLO QCD theory predictions. By calculating the theoretical cross section with different sets of pdf's, the sensitivity of the measured cross section to the input pdf in the theory can be tested. Hopefully, the cross section can contribute directly to the determination of the pdf's. Since the NLO calculations carry a small dependence on the renormalization scale μ, comparison to the data may suggest a preferred value of μ for other calculations [12, 17].

Table 2.1: All 2→2 subprocesses contributing to the jet cross section along with the relative magnitude of their squared matrix elements at 90^o in the center-of-mass. Here q and q' denote different quark flavors.

Subprocesses	$\lvert M(90^0)\rvert^2/16\pi^2\alpha_s^2$
$qq' \rightarrow qq'$	2.2
$q\bar{q}' \rightarrow q\bar{q}'$	2.2
$qq \rightarrow qq$	0.2
$q\bar{q} \rightarrow q\bar{q}$	2.6
$q\bar{q} \rightarrow gg$	1.0
$gg \rightarrow q\bar{q}$	0.1
$qg \rightarrow qg$	6.1
$gg \rightarrow gg$	30.4

Table 2.2: All 2→3 subprocesses contributing to the jet cross section. Here q and q' denote different quark flavors.

$qq' \rightarrow qq'g$
$qg \rightarrow qq'\bar{q}'$
$q\bar{q}' \rightarrow q\bar{q}'g$
$q\bar{q} \rightarrow \bar{q}'q'g$
$qq \rightarrow qqg$
$qg \rightarrow qq\bar{q}$
$q\bar{q} \rightarrow q\bar{q}g$
$q\bar{q} \rightarrow ggg$
$qg \rightarrow qgg$
$gg \rightarrow q\bar{q}g$
$gg \rightarrow ggg$

At NLO, QCD also predicts the inclusive jet cross section decreases with jet cone size, $R = \sqrt{(\delta\eta)^2 + (\delta\phi)^2}$ at a fixed E_T. LO QCD, which includes only 2 → 2 processes, cannot model the dependence of jet cross sections on cone size. However, NLO QCD, with additional 2 → 3 processes can model the dependence. This is illustrated in Fig. 2.4. Notice only one jet is found in the upper event hemisphere with a 0.7 cone, but two with 0.3. The cone size is sensitive to higher order radiation.

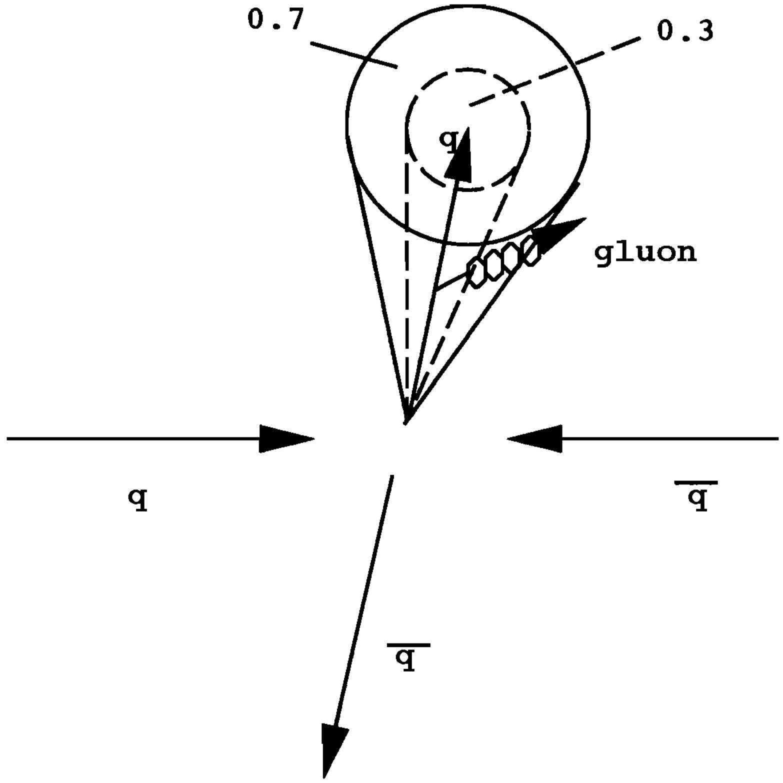

Figure 2.4: NLO QCD prediction of production of a jet at partonic level.

One of the most important roles played by the jet cross section is a test of the Standard Model at small distances. If quarks have constituents, their coupling will be described by additions, ΔL, to the Lagrangian of the Standard Model,

$$\Delta L = \frac{g^2}{\Lambda^2}\bar{\psi}\gamma^{\mu}\psi\bar{\psi}\gamma_{\mu}\psi, \tag{2.12}$$

where g^2 is the coupling in the new theory, Λ is a large mass characteristic of short distances and ψ represent the constituent fields. The effect of such a term in the Lagrangian is to enhance the inclusive jet cross section at high E_T. The jet excess can be characterized as $g^2\frac{E_T^2}{\Lambda^2}$ [17].

2.6 Theoretical Predictions and Uncertainties

Analytic NLO QCD predictions for the inclusive jet cross section has been published by Ellis, Kunszt and Soper(EKS) [18]. Giele, Glover and Kosower [19] have written a NLO program called JETRAD. This program generates "events" with final state partons up to terms of $O(\alpha_s^3)$. These two predictions agree within 1% for small pseudorapidities and over all E_T. For this analysis JETRAD is used for NLO QCD predictions.

JETRAD clusters partons into jets using the Snowmass accord [21] in which the jet direction (η, ϕ) and transverse energy (E_T) are given by

$$\eta_{jet} = \frac{\sum_i E_T^i \eta^i}{\sum_i E_T^i}; \phi_{jet} = \frac{\sum_i E_T^i \phi^i}{\sum_i E_T^i}; E_T = \sum_i E_T^i = \sum_i E_i sin(\theta_i) \tag{2.13}$$

where, i runs over all partons in a jet for a partonic generator or cells for calorimeter. Each parton forms a jet by itself or is merged with another one to form a jet, depending on the E_T weighted distance condition:

$$\sqrt{(\eta_i - \eta_j)^2 + (\phi_i - \phi_j)^2} < \frac{E_{T_i} + E_{T_j}}{MAX(E_{T_i}, E_{T_j})} \times R, \tag{2.14}$$

where R is the radius of the jet cone. According to this clustering condition, two partons as far as $2R$ apart can be included in a jet. Studies have shown jets a distance of $1.3R$ apart are resolved by calorimeter level jet reconstruction [20]. As a result we modify the Snowmass definition by clustering only those partons that satisfy condition 2.15 and are within $1.3R$ of each other.

Two different families of parton distribution functions were used in the NLO QCD predictions: (1) The MRS family uses an input scale of 4 GeV^2 and the MRSD0' set is obtained by using a flat input density at small x, $f_g(x) \sim f_{sea}(x) \sim constant$ [22]. MRSD0' does not include HERA data. (2) The CTEQ family also uses an input scale of 4 GeV^2, but has steep input densities, $f_g(x) \sim x^{-0.38}\log(1/x)^{0.09}$ and $f_{sea}(x) \sim x^{-0.27}$.

CTEQ2M uses the DIS data from the Chicago-Columbia-Fermilab-Rockefeller Collaboration (CCFR), the New Muon Collaboration (NMC) and HERA data, while CTEQ2ML uses the same data as CTEQ2M but with the LEP value of Λ_{QCD} (220 - 240 MeV) [23, 24]. CTEQ3M uses all measurements used for CTEQ2M along with the NA51 and CDF asymmetry measurements [24].

Fig. 2.5 shows the inclusive jet cross section from JETRAD for 1.0, 0.7, 0.5 and 0.3 cone sizes in the central pseudorapidity bin ($|\eta| \leq 0.5$). The parton distribution function (pdf) used is CTEQ2M and the perturbative expansion was evaluated at the renormalization scale of $E_{T_{max}}/2$ where $E_{T_{max}}$ is the maximum jet E_T in an event. Fig. 2.6 shows the ratio of cross sections of jets with different cone sizes to the 0.7 cone jet cross section. As can be seen from the figure, the cross section does decrease with cone size.

The theoretical predictions depend on the choice of pdf's, renormalization scale μ (because the NLO calculation is truncated at order α_s^3 there is some residual dependence on μ), and the clustering algorithm used to cluster partons into a "jet". Each of these dependencies generates a $\sim$ 10-20% uncertainty on the cross section at any η, E_T and cone size. The effect of the pdf on the inclusive jet cross section at various cone sizes is shown in Fig. 2.7. This figure shows the ratio of cross section at given cone size evaluated with CTEQ2M to the cross section evaluated with MRSD0'. Fig. 2.8 shows the effect of the renormalization scale ($\mu = E_T$ and $E_T/2$) on the inclusive jet cross section at various cone sizes. The ratio of cross section at a given cone size evaluated with a μ scale of E_T or $E_T/2$ to the cross section evaluated with $\mu = E_T$ is shown in this figure. Fig. 2.9 shows the effect of the choice of the clustering algorithm (R_{sep}=1.3 and 2.0) used to cluster partons on the cross section. Table 2.3 lists the magnitudes of each effect on the inclusive jet cross section at different cone sizes in $|\eta| \leq 0.5$.

Figs. 2.10, 2.11 and 2.12 show the effect of pdf, renormalization scale and clustering algorithm choices on the ratio of jet cross sections in $|\eta| \leq 0.5$. Each cross section has been normalized by the cross section for 0.7 cone jets. The magnitudes of each effect are listed in Table 2.4. In general, theoretical uncertainties are greatly reduced for the ratio of cross sections. As can be seen from Fig. 2.10, the ratio is not sensitive to the pdf. Fig. 2.12 shows variations due to the choice of clustering algorithm is vanishingly small (2-3%). A $\sim$7% variation due to the choice of the μ scale remains, see Fig. 2.11. A comparison of the measured ratio of cross sections to NLO QCD calculations evaluated at different values of the μ scale will indicate the preferred renormalization scale for the inclusive jet cross section.

Table 2.3: Variations of the theoretical predictions (in percentage) for the inclusive jet cross section for different cone sizes (R).

Source	R=1.0	R=0.7	R=0.5	R=0.3
pdf	20%	20%	20%	20%
μ Scale	10%	10%	20%	40%
Clustering Algorithm	7.8%	4.1%	3.7%	2.7%

Table 2.4: Variations of the theoretical predictions (in percentage) for the ratio of cross sections of different cone sizes to the cross section for 0.7 cone jets.

Source	1.0/0.7	0.5/0.7	0.3/0.7
pdf	0	0	0
μ Scale	7%	7-2%	7%
Clustering Algorithm	2-3%	2-3%	2-3%

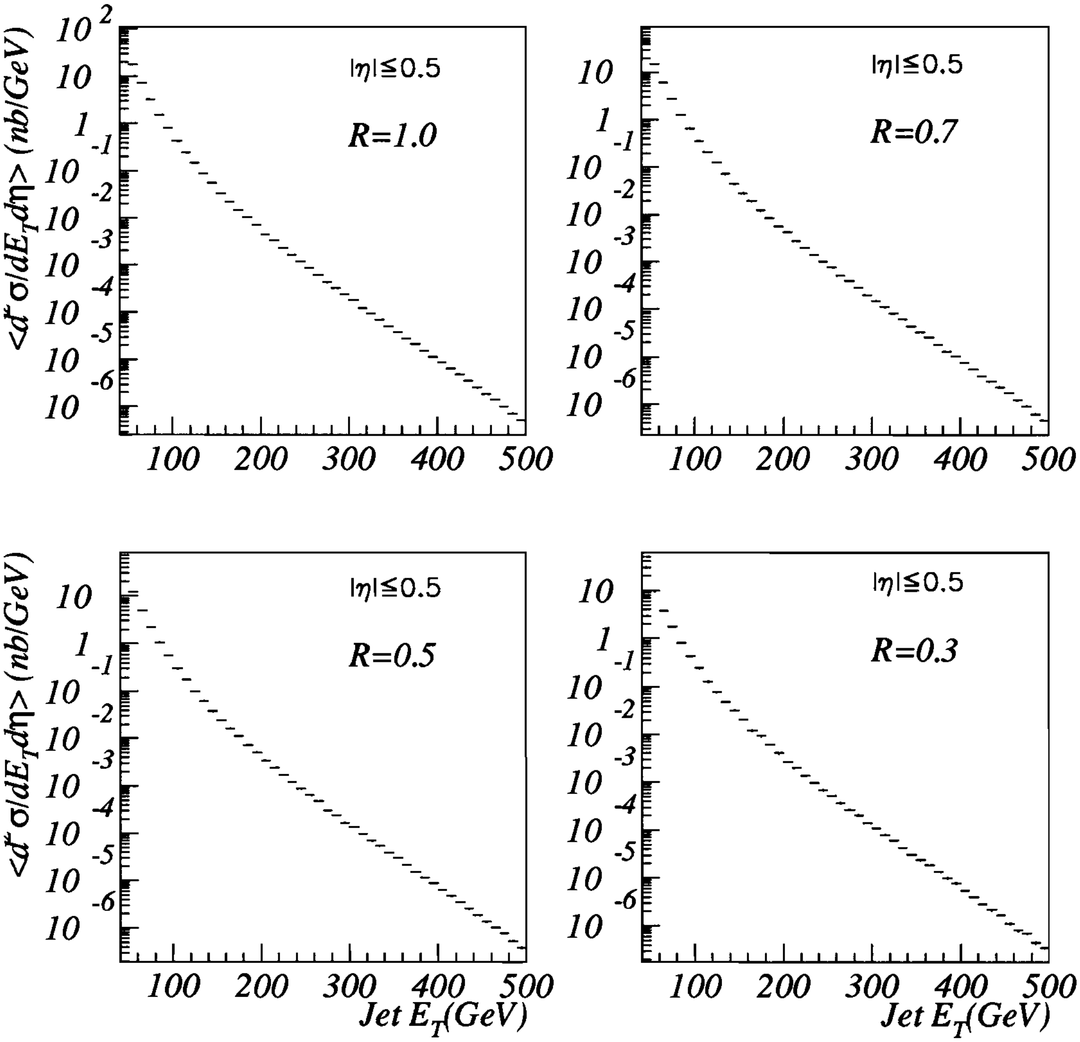

Figure 2.5: JETRAD (NLO QCD) prediction for different cone sizes, with CTEQ2M and $\mu = E_T/2$ of the leading jet.

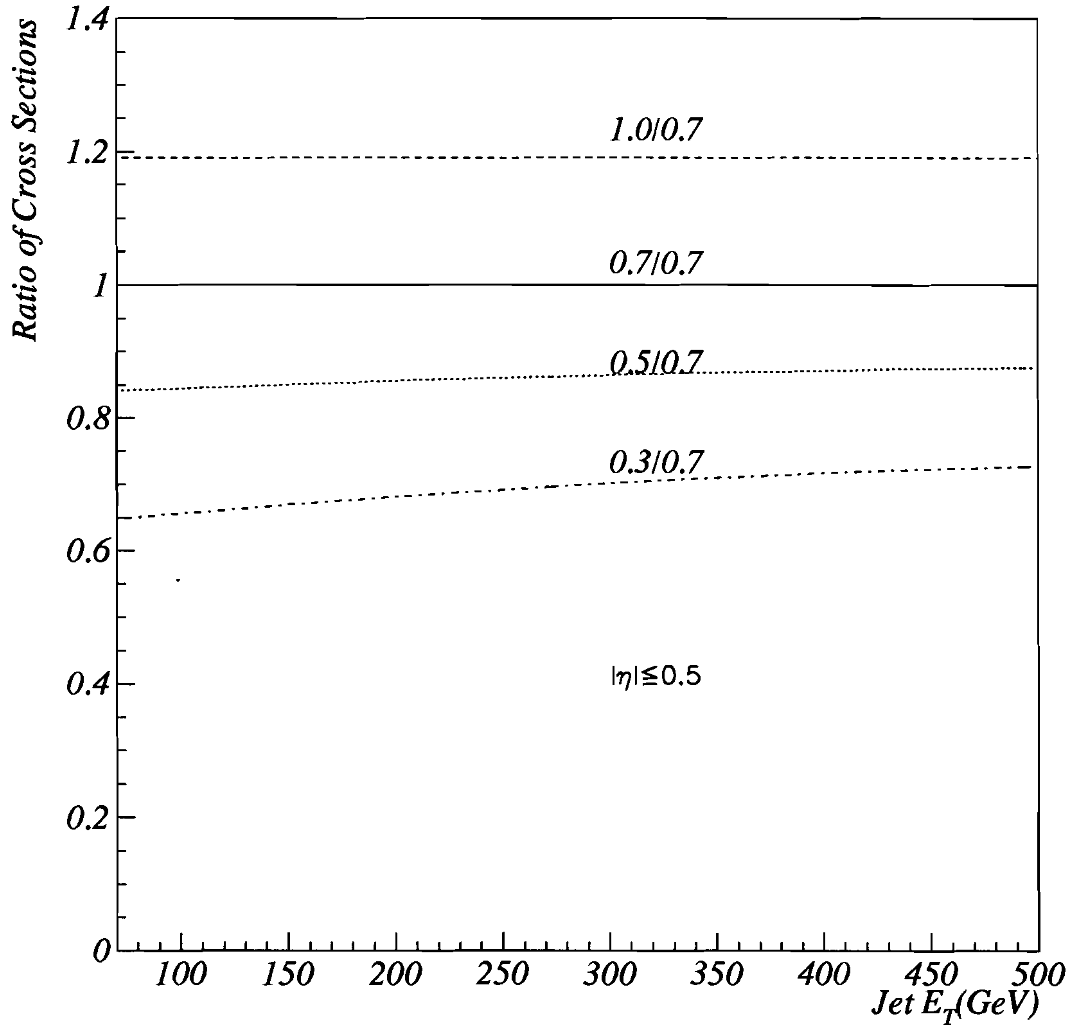

Figure 2.6: Ratio of the cross sections for different cone sizes to that of the cross section for 0.7 jets, from JETRAD (NLO QCD), with CTEQ2M and evaluated at $\mu = E_T/2$ of the leading jet.

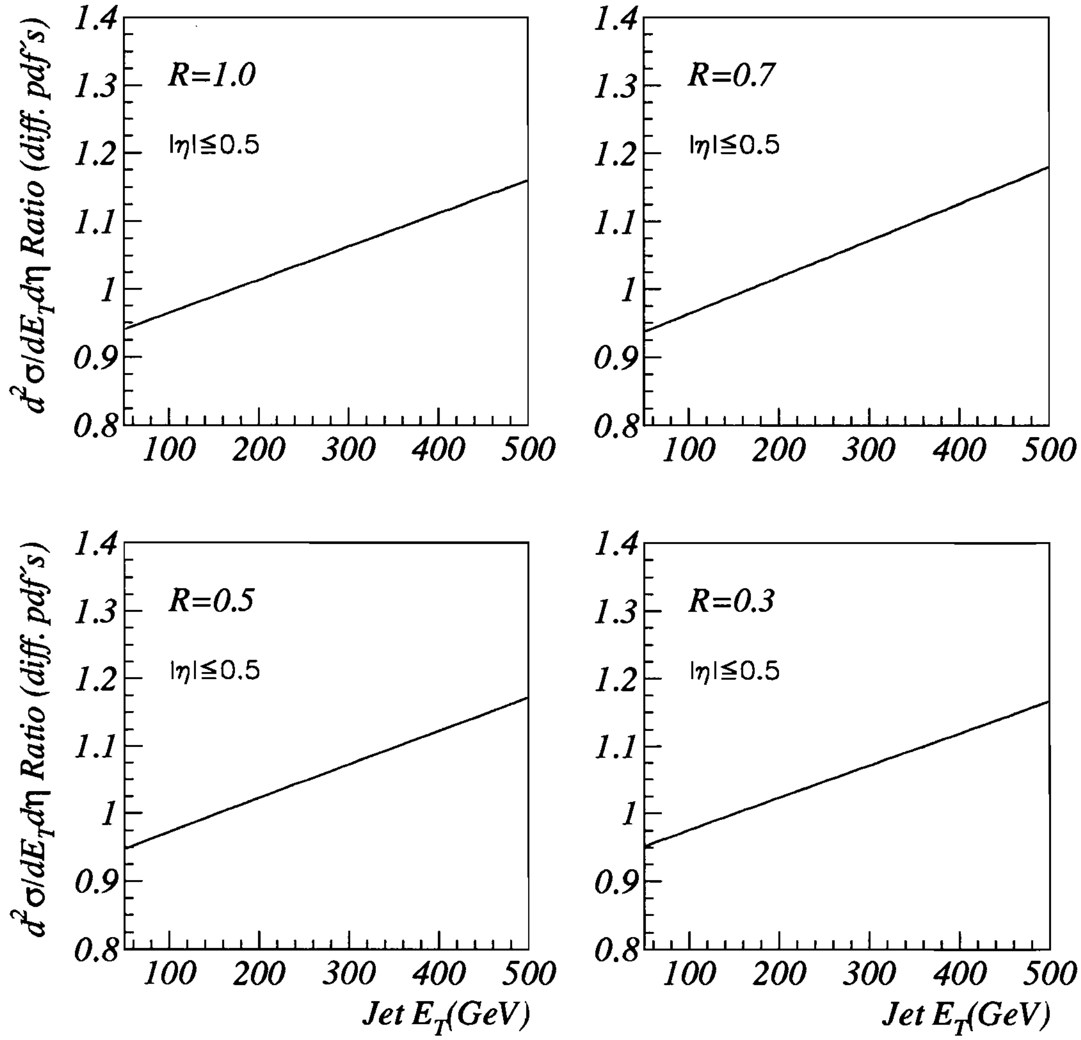

Figure 2.7: The ratio of the cross section at a given jet cone size, evaluated with CTEQ2M to the cross section evaluated with MRSD0'.

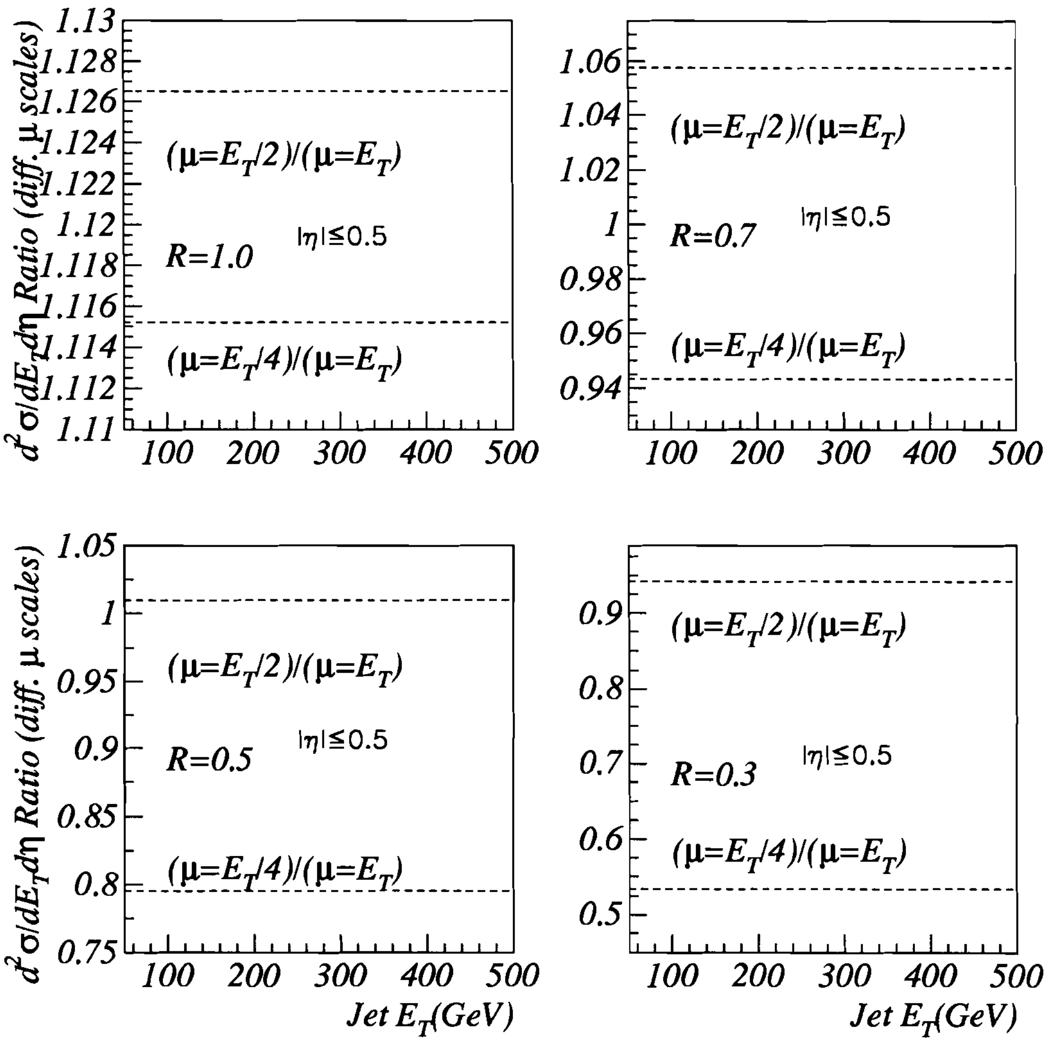

Figure 2.8: The ratio of the cross section at a given jet cone size, evaluated with $\mu = E_T/2$ or $E_T/4$ to the cross section evaluated with $\mu = E_T$ of the leading jet in the event.

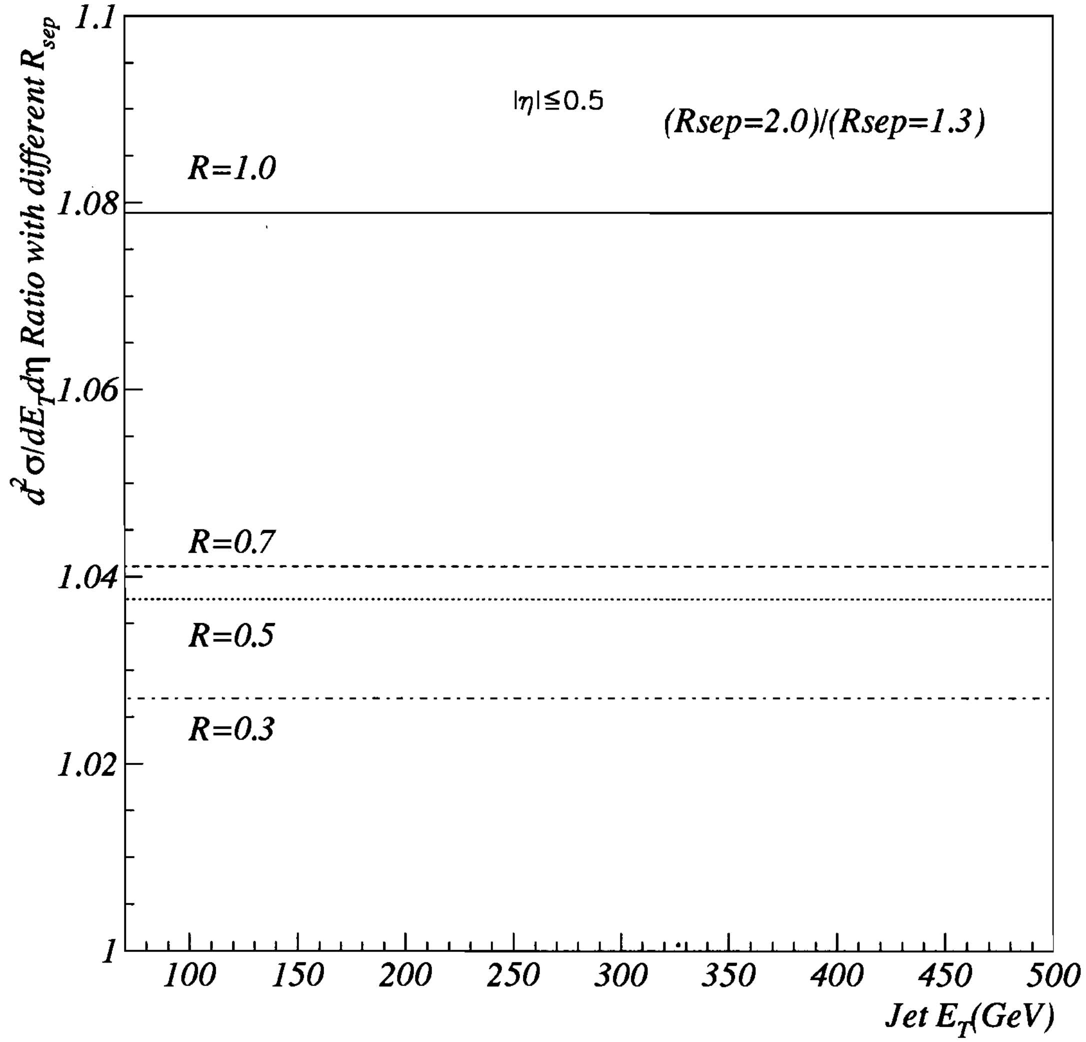

Figure 2.9: The ratio of the cross section at a given jet cone size evaluated with two different clustering algorithms.

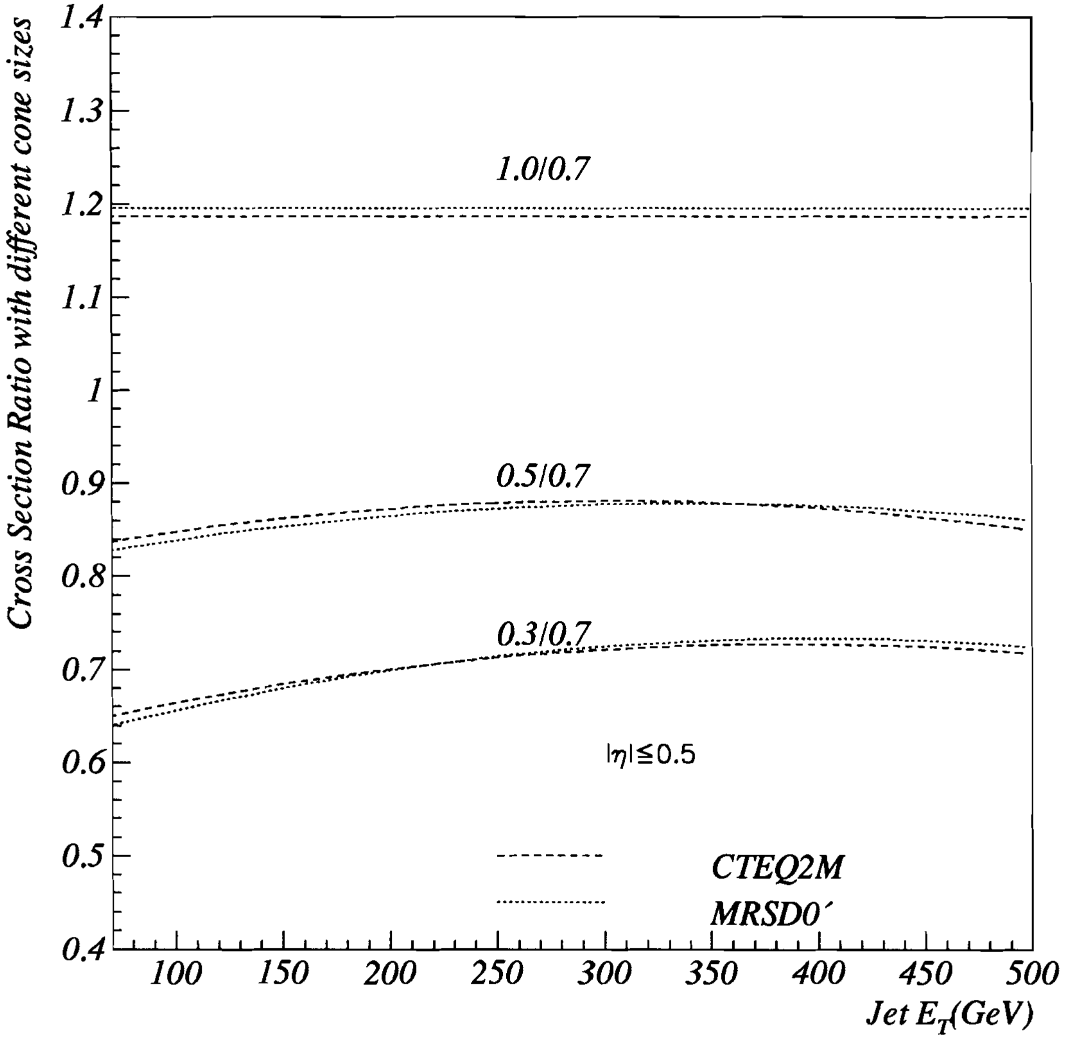

Figure 2.10: Ratio of the cross sections of different cone sizes to the cross section for 0.7 cone jets evaluated with CTEQ2M and MRSD0'.

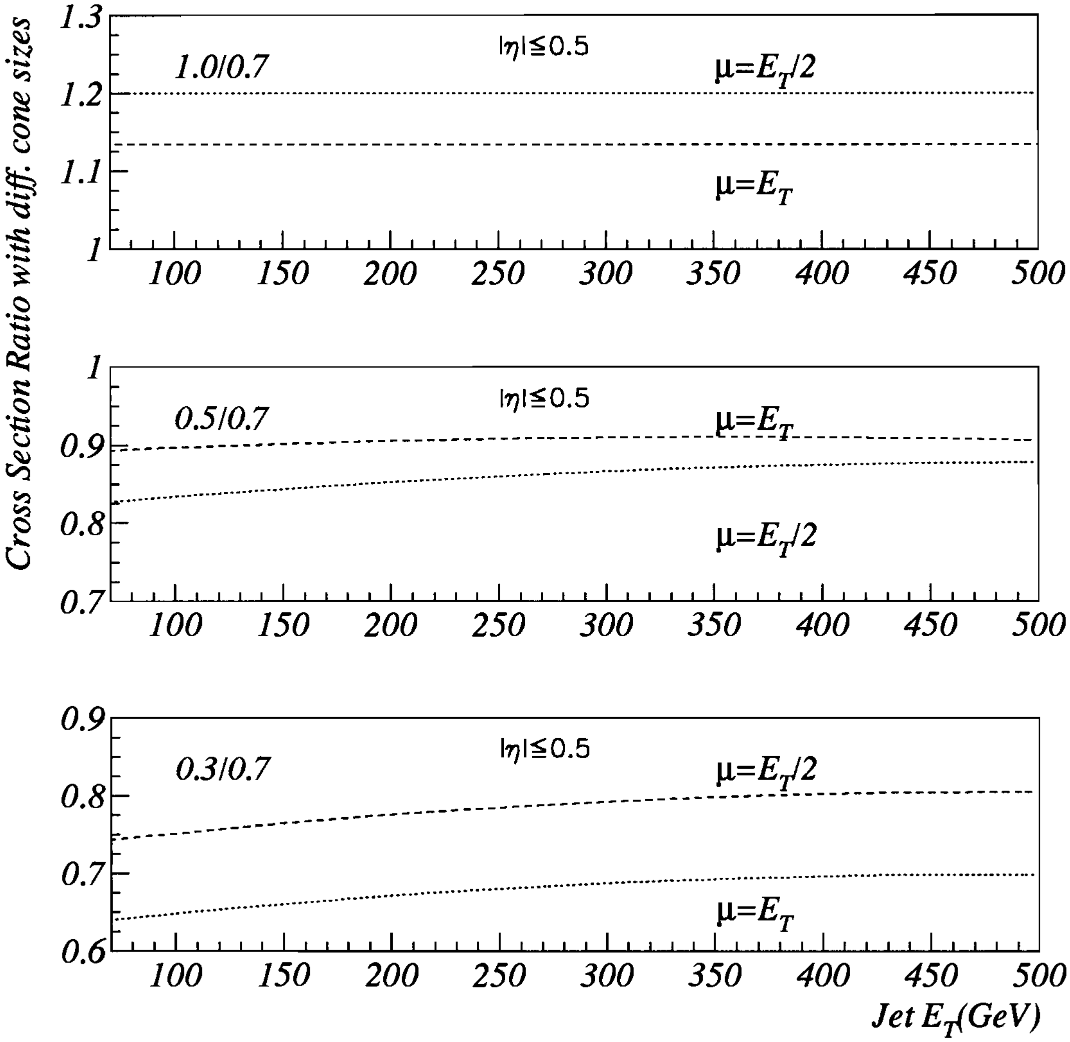

Figure 2.11: Ratio of the cross sections of different cone sizes to the cross section for 0.7 cone jets evaluated with $\mu = E_T/2$ and E_T of the leading jet in the event.

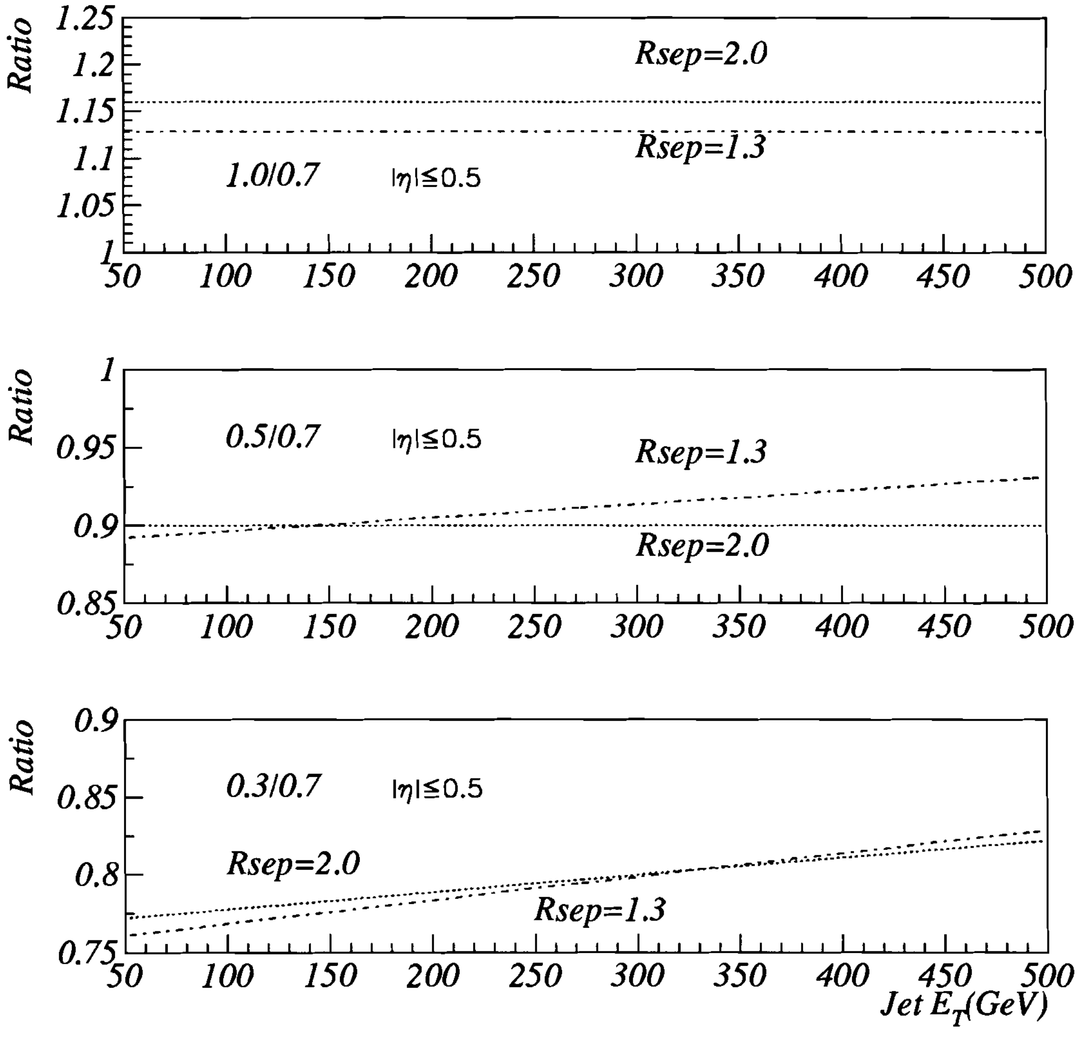

Figure 2.12: The ratio of the cross sections with different jet cone sizes to the cross section for 0.7 cone jets evaluated with two different clustering algorithms.

Chapter 3

The Experimental Setup

3.1 The Collider

The proton-antiproton ($p\bar{p}$) collider at Fermi National Accelerator Laboratory (Fermilab) in Chicago, is the highest energy hadron collider in the world. This machine, which started operation in 1985, also known as the Tevatron, provides $p\bar{p}$ collisions at a center-of-mass (CM) energy of 1.8 TeV. The Tevatron is a storage ring composed of superconducting magnets. A schematic diagram of the entire Fermilab collider complex is shown in Fig. 3.1. Acceleration of protons and antiprotons is achieved in different stages, which will be discussed in this section.

The first stage of acceleration is a Cockroft-Walton accelerator, which accelerates negative hydrogen ions (H^-) to 750 KeV. These H^- ions then enter a 150 meter linear accelerator (Linac) which boosts their energy to 200 MeV. In the next stage, the ions are stripped of their electrons by passage through a carbon foil, leaving only bare protons. These protons then enter a 151 meter diameter synchrotron called the Booster which increases their energy to 8 GeV. In the next stage, the Main Ring, which has a radius of 1000 meters and is made of 1000 conventional magnets, the protons are accelerated to an energy of 150 GeV. After acceleration in the Main Ring the protons are used to produce antiprotons or are injected into the Tevatron for final acceleration to 900 GeV.

The Tevatron, located 65 cm below the Main Ring, is a proton synchrotron made of superconducting magnets and can accelerate protons (antiprotons) to 900 GeV [25, 26, 27]. This machine can be used in two modes: (1) the beam can be extracted after it has attained the desired energy and directed to fixed target experiments; or (2) proton and antiproton bunches can be accelerated in opposite directions and made to collide with each other at the B0 and D0 experimental areas. There are six bunches of protons and six bunches of antiprotons, travelling in opposite directions in the Tevatron.

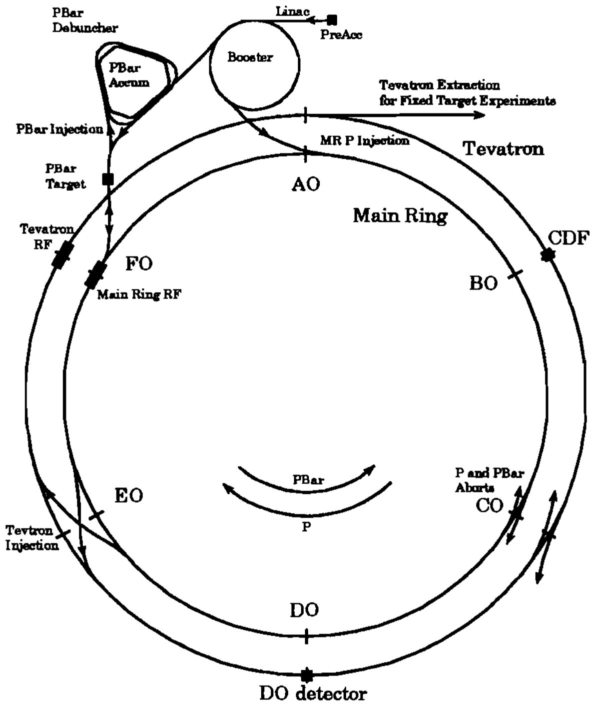

Figure 3.1: Schematic diagram of the Fermilab accelerator complex.

The antiprotons are produced by the Main Ring at the rate of one bunch every 2.4 seconds [26, 28]. Protons of energy 120 GeV, extracted from the Main Ring, illuminate a nickel target, which produces a spray of nuclear debri and antiprotons. The negatively charged particles with energies more than 8 GeV are selected and passed to the

Debuncher, which is a antiproton storage ring. The Debuncher reduces the momentum spread of the antiprotons by the process of stochastic "cooling" [28, 29]. The antiprotons are then moved to the Accumulator, another storage ring, where cooling continues for several hours until antiprotons settle into a dense core near the inner radius of the Accumulator. Once, a sufficient number of $\bar{p}$'s have been accumulated, they are extracted and accelerated to 150 GeV in the Main Ring and then injected into the Tevatron in bunches. Some of the parameters of the Tevatron for the 1992-93 Run (Run 1A) are listed in Table 3.1.

Table 3.1: Run IA Tevatron parameters.

Accelerator radius	1000 m
Maximum beam energy	900 GeV
Injection energy	150 GeV
Peak luminosity	$\sim 10 \times 10^{30}$ cm^{-2}s^{-1}
Number of bunches	6 p, 6 $\bar{p}$
Intensity per bunch	$\sim 100 \times 10^{9}$ p, 50×10^{9} $\bar{p}$
Bunch length	50 cm
Transverse beam radius	43 μm
RF frequency	53 MHz
$\bar{p}$ stacking rate	$\sim 3.5 \times 10^{10}$/hour
Beam crossing frequency	290 kHz
Period between crossings	3.5 μs

The instantaneous luminosity or the interaction rate is given by:

$$L = \frac{f N_b N_p N_{\bar{p}}}{4\pi\sigma^2}, \tag{3.1}$$

where, f is the crossing frequency, N_b is number of bunches, N_p and $N_{\bar{p}}$ are the number of protons and antiprotons and $\pi\sigma^2$ is the cross section of the beam. L can be increased by the reducing the beam cross section. The typical instantaneous luminosity during Run 1A was 5×10^{30} cm^{-2} sec^{-1} .

3.2 The D0 Detector

The D0 detector, which has been operating at the Fermilab Tevatron since 1992, is a multipurpose device designed to study $p\bar{p}$ collisions at a CM energy of 1.8 TeV. The detector has been designed and optimized for the study of high-p_t physics, high mass states, identification and measurement of electrons and muons, measurement of direction and total energy of high-p_t jets, and the determination of missing transverse energy [30]. Fig. 3.2 shows a general view of the D0 detector. The components of the detector are described below.

A right handed coordinate system is adopted for D0 with the positive z-axis along the beam and an upward positive y-axis. For cylindrical coordinates r is the distance from the beam axis.

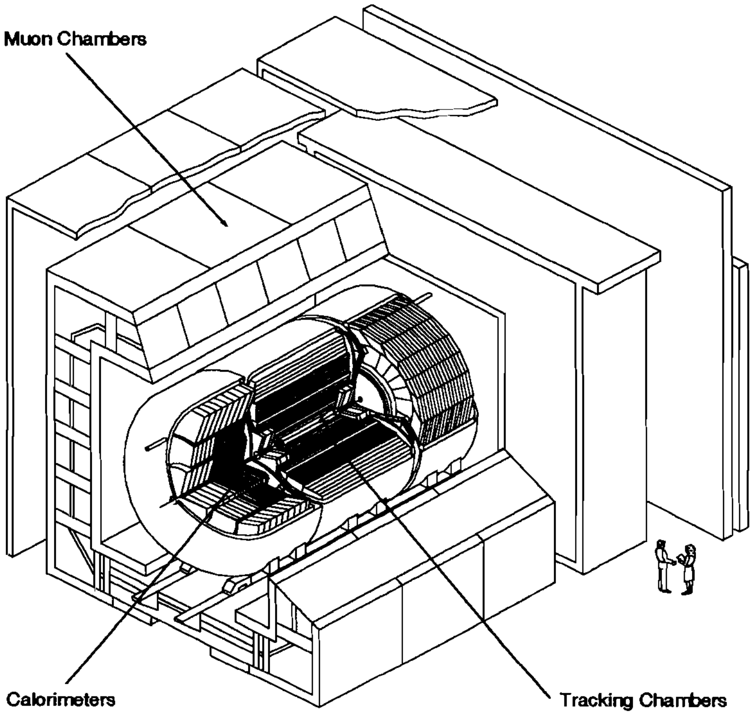

Figure 3.2: The D0 Detector.

3.2.1 The Central Detector

The central detector (CD) consists of a vertex drift chamber (VTX), a transition radiation detector (TRD), a central drift chamber (CDC) and two forward drift chambers (FDC). The CD is bounded radially by $r = 78$ cm and the inner radius of the calorimeter, and $z = \pm 135$ cm. The CD is used to reconstruct the three dimensional trajectory of charged particles. Fig. 3.3 shows a schematic diagram of the central detector. The VTX, TRD and CDC are concentric with the beam pipe, while the FDCs are perpendicular to the beam axis. Without a central magnetic field, momentum measurement of charged particles was not possible, but the CD was designed for good spatial resolution of individual particles and good ionization energy measurement. The tracking system can determine the primary z-vertex to within 1 cm. The different parts of the CD are described below and summarized in Table 3.2. The DØ tracking and TRD detectors have 6080 channels in total [30].

The Vertex Chamber (VTX)

The VTX chamber is the innermost tracking device with an inner radius of 3.7 cm and an outer radius of 16.2 cm. The VTX samples tracks near the interaction vertex and can be used to determine vertex position. The chamber has three independent, concentric cell layers (16 cells in azimuth in the innermost layer and 32 each in the outer two), each cell consisting of 8 staggered sense wires parallel to the beam pipe to provide a measurement of track position in the $r - \phi$ plane. The z-coordinate of the interaction vetrex is determined by charge division [31]. For good spatial resolution and track pair resolving power, a slow gas was chosen which gives an average drift velocity of 7.3 μm/ns. In the drift plane, a typical drift resolution of 50 μm was obtained [30].

The Transition Radiation Detector (TRD)

The TRD is situated just outside the VTX and is surrounded by the CDC. It's function is to distinguish between electrons and charged pions, by a process called transition radiation, where x-rays are emitted when a highly relativistic charged particle ($\gamma > 10^3$)

crosses the boundary between two media with different dielectric constants [32]. The energy of the emitted x-rays depends on the mass of the traversing particle. The TRD consists of three separate layers each containing one radiator followed by an x-ray detection chamber. Pion rejection factors of approximately 50 are found for 90% electron detection efficiency [30].

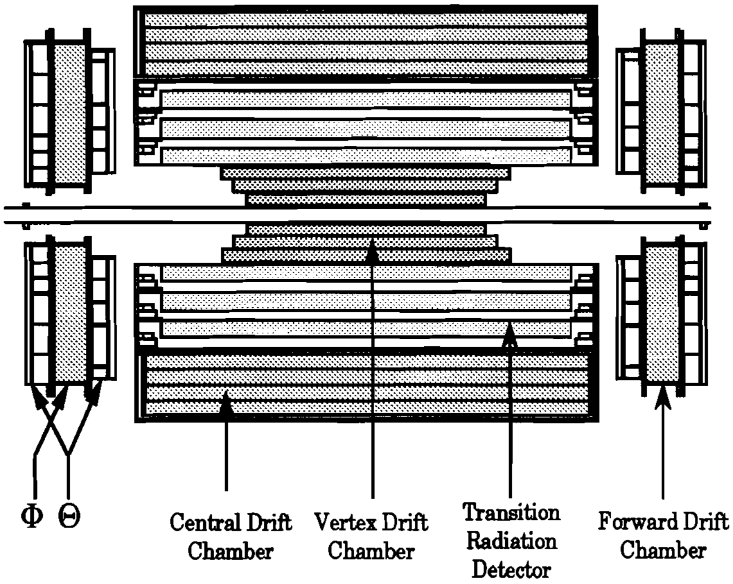

Figure 3.3: The D0 tracking system.

The Central Drift Chamber (CDC)

The CDC, located just outside the TRD, is bounded by the inner radius of the calorimeter and has inner and outer radii of 49.5 and 74.5 cm respectively. It has four independent layers of cells, each cell containing seven staggered sense wires. There are 32 cells per layer. The CDC samples tracks just prior to their entrance into the central calorimeter. A fast gas is used to fill this chamber with a drift velocity of 34 μm/sec. The hit resolution is 150-200 μm and two hit resolution is achieved with 90% efficiency for $\sim$ 2 mm separation.

Table 3.2: Central Detector parameters.

VTX	Sense wire resolution Charge division resolution Pair resolution	60 μm 1 cm 0.7 mm
TRD	e/π discrimination at 90% efficiency	50:1
CDC	Sense wire resolution Delay line resolution Pair resolution	200 μm 2 mm 2 mm
FDC	Sense wire resolution Delay line resolution Pair resolution	200 μm 4mm(Θ), 20mm(Φ) 2 mm

The Forward Drift Chambers (FDC)

The FDCs are used to extend the tracking coverage to very forward regions ($|\eta_d| \sim 3$, where η_d is the detector pseudorapidity). They are placed perpendicular to the beam pipe, upstream and downstream of the concentric barrels containing the VTX, TRD and the CDC. Each FDC has three separate chambers, one Φ module and two Θ modules. These modules are used to determine the ϕ and θ coordinates.

3.2.2 The Calorimeter

The D0 sampling calorimeter determines the energy of electrons, photons and jets. Basically, a calorimeter measures energy by stopping a particle and sampling the energy deposited in the calorimeter material. D0 has a sampling calorimeter which uses liquid argon (LAr) and depleted uranium (DU) as active and passive mediums, respectively. As shown in Fig. 3.4, the calorimeter requires three cryostats, a central calorimeter (CC) covering $|\eta| < 1$ and two end calorimeters (EC) which extends the coverage to $|\eta| \sim 4$. The CC is seven nuclear absorption lengths (λ_A) deep while the EC, nine.

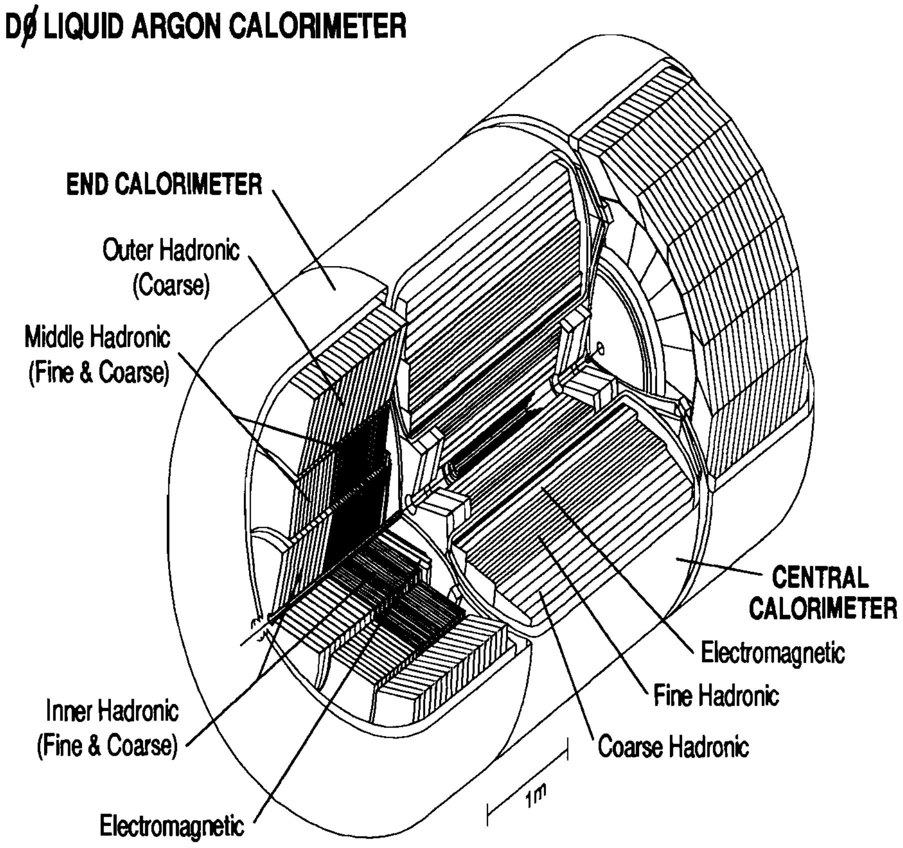

Figure 3.4: The DØ Calorimeter.

Calorimeter Operating Principles

The typical unit cell of the DØ calorimeter, as shown in Fig. 3.5, has a uranium plate and a readout board submerged in LAr. The readout board is made of two separate G-10 boards, the outer faces are coated with a resistive epoxy and the faces carry copper readout plates. The metal absorber plate is grounded and the resistive surfaces are connected to a positive high voltage of 2.0-2.5 kV. This creates an electric field between the absorber and the resistive surface, while the readout board itself acts as a capacitor. High energy particles lose energy in uranium by producing an electromagnetic or hadronic shower. These particles ionize the active material, i.e. LAr, and electrons drift to the anodes producing an image charge on the inner copper surface. This charge is then routed to preamplifiers and then the signal is shaped and amplified before being digitized and sent to the data aquisition system. If the signal values are within $\pm 2\sigma$ of their pedestal values, these channels are suppressed (zero suppression) to reduce the size of output data.

Both the CC and the EC have three distinct calorimeter modules, (1) the electromagnetic section (EM) consisting of thin uranium absorber plates, (2) the fine hadronic section (FH) consisting of thicker uranium plates and (3) the coarse hadronic section (CH) consisting of thick copper in the CC and stainless steel plates in the EC. The calorimeter modules are pseudo-projective, that is, the readout cells are grouped in towers which project to $z = 0$ (see Fig. 3.6). The transverse size of the cells, $\Delta\eta \times \Delta\phi = 0.1 \times 0.1$, was chosen to be comparable to the transverse shower size, which is ~1-2 cm for EM-showers and ~10 cm for hadronic showers. The DØ calorimeter has more than 50,000 channels. The three types of calorimeter modules are discussed below. Some of the parameters of the DØ calorimeter in Run 1A are summarized in Tables 3.3 and 3.4 [30].

Table 3.3: Central Calorimeter parameters.

Module type	EM	FH	CH
Rapidity coverage	±1.2	±1.0	±0.6
Number of modules	32	16	16
Absorber	DU	DU-Nb	Cu
Absorber thickness (mm)	3	6	46.5
Argon gap (mm)	2.3	2.3	2.3
Number of signal boards	21	50	9
Number of readout layers	4	3	1
Cells per readout layer	2,2,7,10	20,16,14	9
Total radiation lengths (X_0)	20.5	966.0	32.9
Total nuclear absorption lengths (λ)	0.76	3.2	3.2
Sampling fraction (%)	11.79	6.79	1.45

Table 3.4: End Calorimeter parameters.

Module type	EM	IFH	ICH	MFH	MCH	OH
Rapidity coverage	1.3-3.7	1.6-4.5	2.0-4.5	1.0-1.7	1.3-1.9	0.7-1.4
No. of modules	1	1	1	16	16	16
Absorber	DU	DU-Nb	SS	DU-Nb	SS	SS
Absorber thickness (mm)	4	6	6	6	46.5	46.5
Argon gap (mm)	2.3	2.1	2.1	2.2	2.2	2.2
Signal boards	18	64	12	60	14	24
R.O. layers	4	4	1	4	1	3
Cells/R.O. layer	2,2,6,8	16	14	15	12	8
Total rad. len.	7 20.5	121.8	32.8	115.5	37.9	65.1
Total abs. len.	0.95	4.9	3.6	4.0	4.1	7.0
Samp. frac. (%)	11.79	5.7	1.5	6.7	1.6	1.6

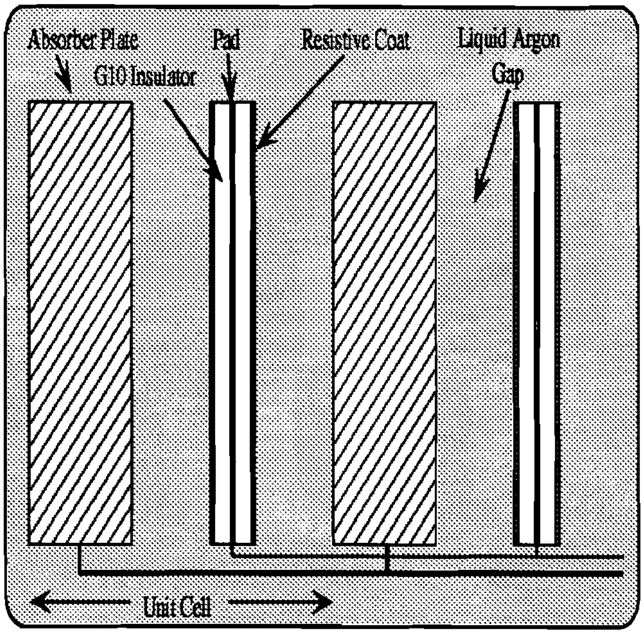

Figure 3.5: A calorimeter unit cell.

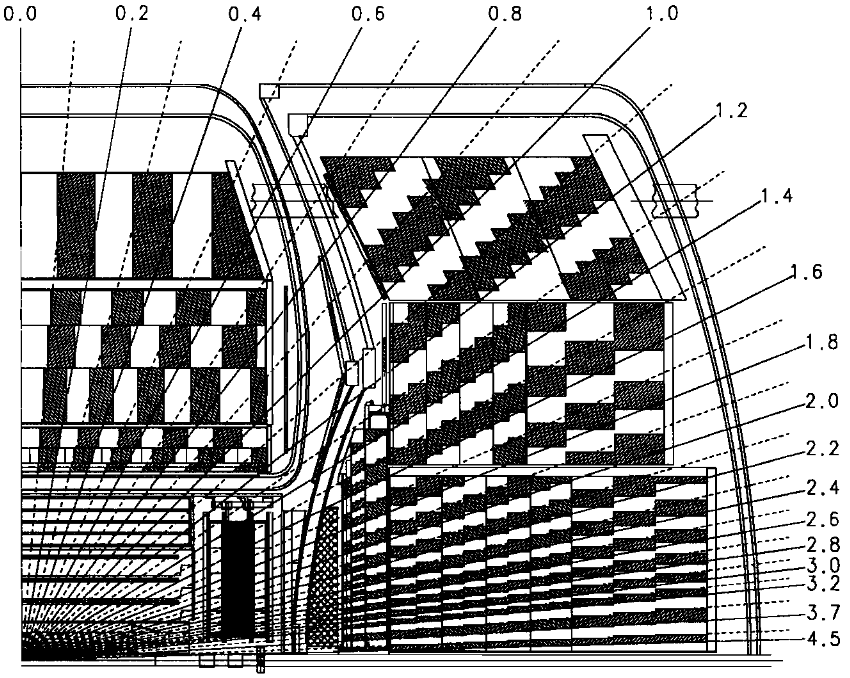

Figure 3.6: Pseudoprojective structure of the D0 calorimeter.

Electromagnetic modules (EM)

The innermost calorimeter component is the EM section which is located just outside the tracking system. In this section, there are four sampling layers of 2, 2, 7 and 10 radiation lengths (X_0) in thickness, each of which contain depleted uranium plates of 3-4 mm thickness. The third layer is at the EM shower maximum and has a transverse segmentation of $\Delta\eta \times \Delta\phi = 0.05 \times 0.05$ for precise measurement of the shower centroid.

The fourth layer has large calorimetric depth to contain the entire EM shower.

Fine Hadronic modules (FH)

The FH section is located between the EM and CH sections. This section has three or four longitudinal layers of 1.3, 1.0 and 0.9 λ_A in thickness, each containing plates of uranium-niobium alloy 6 mm thick. The transverse segmentation is $\Delta\eta \times \Delta\phi = 0.1 \times 0.1$ and was designed to contain most of the energy of hadronic showers.

Coarse Hadronic modules (CH)

This section lies outside the FH section and has only one longitudinal segment of thick copper (in the CC) or stainless steel (in the EC) absorber plates. The thickness of this section is 3-4 λ_A and the segmentation is 0.1×0.1. The CH module was designed to contain the energy that leaked out of the EM and FH modules.

Intercryostat detectors and massless gaps (ICR)

In order to improve energy measurement and particle detection in the uninstrumented region between the CC and EC cryostat walls, which extends from $\sim$0.8 to $\sim$1.4 in detector pseudorapidity, η_d, intercryostat detectors (ICD) and massless gap detectors (MG) were employed. The ICDs were mounted on the front surface of the ECs, and each ICD consists of 384 scintillator tiles of segmentation $\Delta\eta \times \Delta\phi = 0.1 \times 0.1$, exactly matching the size of the calorimeter cells. MGs are mounted both on the CC and the EC, and these are single cell structures.

Calorimeter Performance

The performance of the calorimeter has been studied in a test beam [33] with electrons and pions of energy ranging from 2 to 150 GeV and also with collider data. The response of the calorimeter to single electrons and pions have been studied extensively in the test beam. The response for both has been found to be linear within 0.5% [34]. The energy resolution of the calorimeter has been parametrized as:

$$\frac{\sigma^2}{E^2} = C^2 + \frac{S^2}{E} + \frac{N^2}{E^2}, \tag{3.2}$$

where, C, S and N represent the constant, sampling and noise terms, respectively. The energy resolution was found to be $15\%/\sqrt{E}$ for single electrons and $50\%/\sqrt{E}$ for single pions [30]. Most of the noise is due to uranium radioactivity. The position resolution was found to be $2\text{cm}/\sqrt{E}$ for electrons. The energy resolution and linearity is affected by the e/π response ratio of the calorimeter, which is found to decrease from 1.11 at 10 GeV to 1.04 at 150 GeV.

3.2.3 The Muon System

The muon system consists of five solid iron torroidal magnets surrounded by three layers of proportional drift tubes (PDT) and covers the pseudorapidity $\eta_d < 3.6$ [30]. The muon system is used to determine the trajectory and momentum of muons from $p\bar{p}$ collisions. The PDTs measure trajectory of the muons before and after they pass through the magnetized torroids, giving a measurement of the muon momentum.

The muon system is divided into two main sets of chambers. The wide angle muon chamber (WAMUS) covers the angular region $|\eta_d| < 2.5$. The total number of WAMUS PDT cells is 11,386. The small angle muon chambers (SAMUS) covers the forward regions $2.5 < |\eta_d| < 3.6$. The total number of SAMUS tubes is 5308. The central toroid covers the region of $|\eta_d| < 1.0$ and two end toroids cover $1.0 < |\eta_d| < 2.5$. The two SAMUS toroids cover $2.5 < |\eta_d| < 3.6$. There are 50,920 analog elements in the muon system. The muon momentum resolution is given by:

$$\frac{\delta p^2}{p^2} = (0.18)^2 + \frac{0.01^2}{p^2}, \tag{3.3}$$

where, p is the muon momentum in GeV/c.

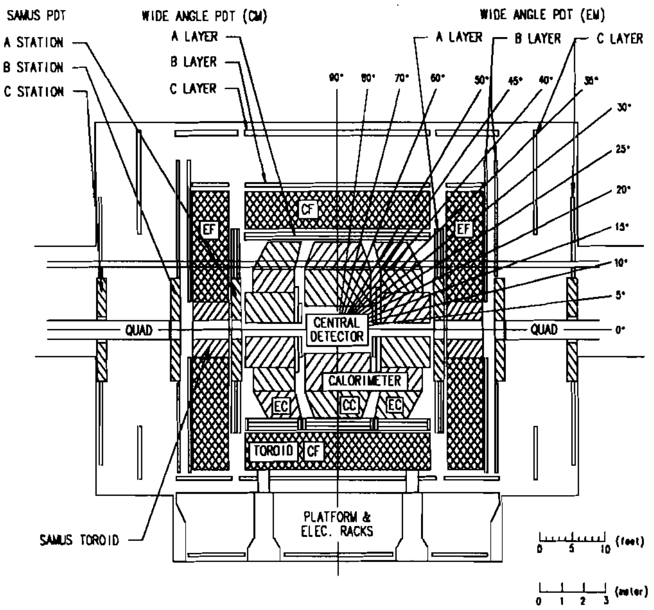

Figure 3.7: Side view of the D0 muon system.

3.2.4 Trigger System

The beam crossing rate at the Tevatron is about 290 kHz and the instantaneous luminosity for Run IA was $5 \times 10^{30} cm^{-2} s^{-1}$. With these machine conditions an inelastic collision occurred for 75% of the beam crossings. Most of the events are single interactions, only $\sim$ 17% of the events are multiple interactions. However, the processes of interest are rare and hence a trigger is required to select the small fraction of interesting events and write them to tape. The triggers are designed in such a way that they are able to handle the event rates as a function of E_T and η. In D0 , the trigger system works at three levels. Fig. 3.8 shows the D0 data acquisition system.

Level 0

The first or **Level 0 (L0)** trigger detects events with inelastic collisions. This trigger system utilizes the coincidence signal from two hodoscopes placed on the front surfaces of the end calorimeters to signal $p\bar{p}$ inelastic collision. The L0 trigger is more than 99% efficient for nondiffractive inelastic collisions. By comparing the arrival times of the signals from the two hodoscopes, the L0 detector also provides a fast measurement of the z-coordinate of the interaction vertex within 800 ns of the collision with a resolution of ±15 cm. The L0 system can also identify events containing multiple interactions [35].

For all jet triggers, except the highest E_T trigger, a cut on the vertex z-coordinate ($|z| < 10.5$ cm) was applied online at L0 . This reduced trigger rates by factors of 3-4. This selects events well measured by the calorimeter.

Level 1

The second trigger level, **Level 1 (L1)**, is a hardware trigger. Many L1 triggers operate within the 3.5 μs time between beam crossings and do not contribute any deadtime. The hardware calorimeter and a part of the muon trigger satisfy this condition. However, the remaining portion of the muon trigger requires several bunch crossings to complete computations and is referred to as **Level 1.5 (L1.5)** trigger. In Run 1A, L1 triggers reduced event rates from a beam crossing frequency of 290 kHz to 200 Hz. The L1.5 trigger reduced this rate to under 100 Hz. The control of the L1 triggers resides in the Level 1 Framework.

The L1 calorimeter trigger makes trigger decisions based on calorimeter information and selects events based on a deposition of energy in the calorimeter transverse to the beam line. The E_T of a trigger tower is calculated as:

$$E_T = \sum_i [E_T^{EM}(i) + E_T^{FH}(i)], \tag{3.4}$$

where the sum is over all the cells in the EM and FH modules of the calorimeter within the tower *i*. A jet event will fire L1, if the condition JT(n,e) where n is the least number of trigger towers and e is the E_T threshold, is satisfied. This trigger level does not introduce any dead time and a decision is taken within 3.5 μs of the beam crossings. In Run IA, this trigger covered $|\eta| < 3.2$.

The L1 muon trigger divides the muon system into five geographical regions. The trigger looks for a pattern of hits in all the three layers consistent with a muon emitted from a nominal interaction vertex. After counting the number of track candidates and comparing it with a previously set threshold, trigger decisions were made. The pure L1 muon trigger can not distinguish between muons of different momenta, as tracks were matched between layers very coarsely. The L1.5 muon trigger can distinguish between muons of different momenta.

Level 2

The final trigger or **Level 2 (L2)** trigger is software based and consists of 50 VAX nodes. Events satisfying the LØ , L1 and L1.5 triggers are digitized and sent to an available L2 node. L2 performs a fast reconstruction of the event and runs software filters on the complete data for an event. Since time constraints are not as stringent as in L1, sophisticated algorithms can be used at L2. Once an event is selected by L2, it is stored permanently on magnetic tape. Due to computational limitations the data is written to tape at 2 Hz. Fig. 3.8 shows the data path into and out of the L2 nodes.

For jets, L2 uses a fixed cone algorithm with a cone radius of $R = 0.7$ in $\eta - \phi$ space for reconstruction. The event is selected if the condition L2JT(n,e,r) is satisfied, where n is the number of jets with E_T greater than the threshold e and with a cone size of r. The computation time is about 200 ms.

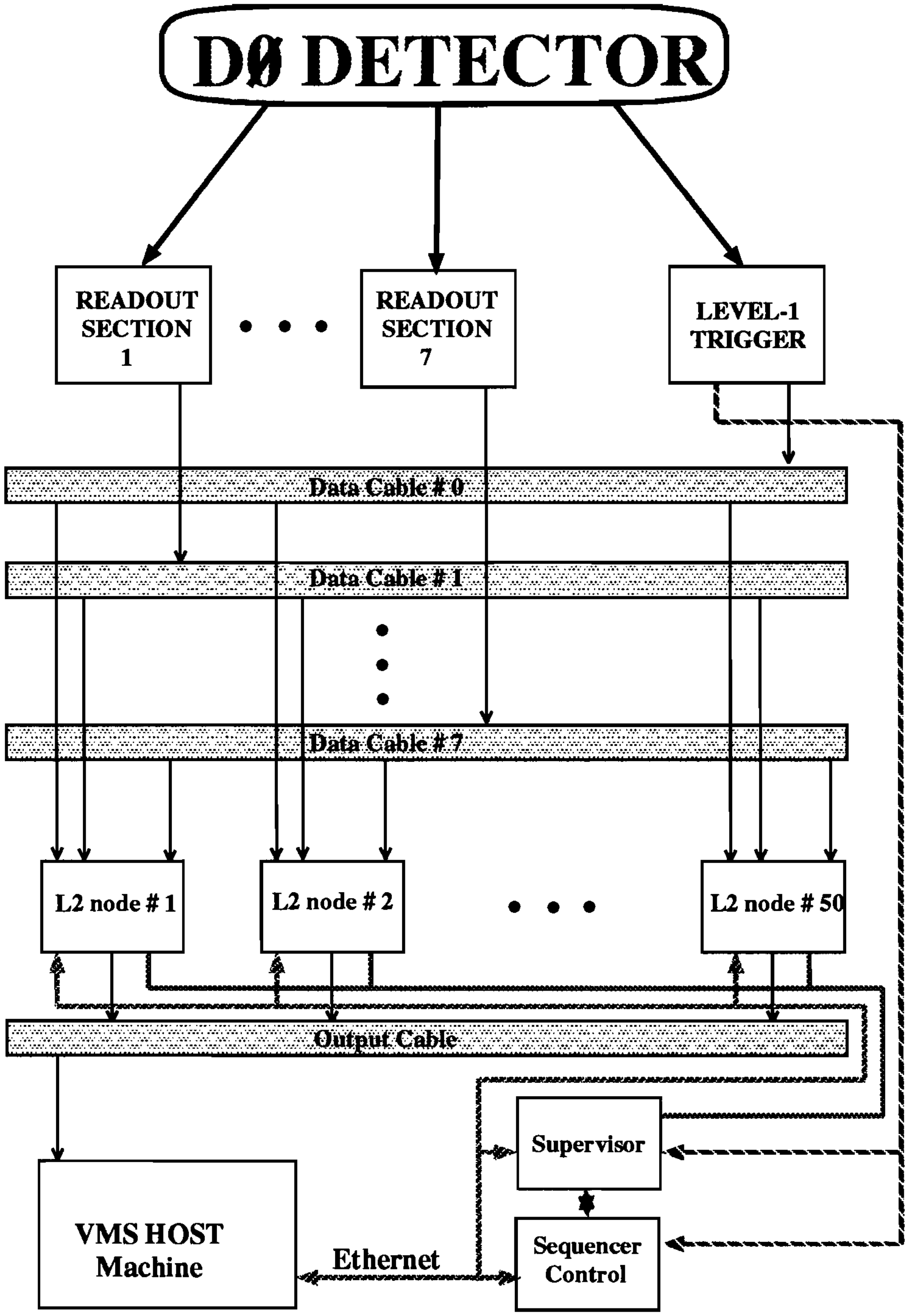

Figure 3.8: Flowchart of the DØ data acquisition system.

Chapter 4

Data Reconstruction

4.1 Introduction

A $p\bar{p}$ collision at a CM energy of 1.8 TeV often involves a hard scattering between two partons of the colliding proton and the antiproton. A scattered quark or gluon then produces a spray of high p_t hadrons, which is called a jet. A jet is identified as a localized peak of hadronic energy in a group of cells or towers in the DØ calorimeter. The DØ experiment uses a fixed cone jet algorithm to reconstruct jets from calorimeter cells [36]. In this chapter the interaction vertex reconstruction, jet reconstruction and the measurement of the event missing transverse energy, $\not{E}_T$, will be discussed.

At this point, it will be useful to discuss the DØ coordinate system. As only one parton from each of the colliding hadrons actually participates in the hard scattering, the nature of a $p\bar{p}$ inelastic scattering is very complex. Only a part of the final state energy is associated with the hard scattering event, the remaining energy resides with the spectator partons that did not take part in the hard scattering. The energy along the beam direction is not known, but one can apply energy conservation in the transverse plane. Hence, it is often convenient to work with the jet transverse energy E_T rather than E.

The position variables chosen are ϕ (azimuth angle), and η (pseudorapidity). The pseudorapidity η, defined as:

$$\eta = -log(tan\frac{\theta}{2}), \tag{4.1}$$

where θ is the polar angle approximates the rapidity,

$$y = \frac{1}{2}log\frac{E+p_z}{E-p_z}, \tag{4.2}$$

in the limit of $m << E$. It can be shown that a boost along the z direction will change η only by an additive constant. Hence, an advantage of E_T, ϕ, η is relativistic invariance.

4.2 Interaction Vertex Reconstruction

The precise measurement of the event interaction vertex is very important in determining the E_T and η of jets. The primary interaction vertex is reconstructed based on the tracks reconstructed with the CDC data. As there is no central magnetic field, the particle trajectories are straight lines. Background arising from particles which do not belong to the hard collision are removed by requiring the tracks used for vertex reconstruction to have an impact parameter less than 2.5 cm relative to the beam axis in $r-\phi$ plane. The $x-y$ position of the vertex is reconstructed from the tracks reconstructed in the VTX in the $r-\phi$ plane. As the beam position is relatively stable with time, the vertex $x-y$ position for each run is calculated as an average of all the events in that run.

The distribution of the interaction vertex z position is Gaussian with a width of about 30 cm centered at z = -10 cm. This position is determined by extrapolating the CDC and FDC tracks in the $r-z$ plane until they intersect the beam axis. The mean of the Gaussian distribution made by all the tracks in an event is taken as its interaction vertex. The z-vertex resolution is dependent on the number of tracks and their angular distribution in an event and varies from 0.65 to 0.95 cm. In case of multiple interactions, the two interaction vertices can be resolved if the clusters of tracks pointing to them are greater than 7 cm apart.

4.3 Fixed Cone Algorithm

DØ has developed a fixed cone jet algorithm to reconstruct jets from calorimeter cells [36] which is very similar to the Snowmass algorithm [21]. This assumes that particles are associated with a jet if they are contained within a cone of radius, $R=\sqrt{(\eta-\eta_0)^2+(\phi-\phi_0)^2}$, centered at the jet axis (η_0,ϕ_0). This type of fixed cone algorithm is highly suited for hadron collider experiments, as the underlying event energy is a small fraction of the total jet energy. Also, compatibility with other experiments can be maintained. The DØ jet algorithm can be divided into two basic parts: (1) accumulation of energy associated with a jet and (2) definition of E_T, ϕ and η. These steps are:

- **Preclustering:** The jet reconstruction process starts with the determination of the E_T in $\Delta\eta \times \Delta\phi = 0.1 \times 0.1$ calorimeter towers. The energy of a projective tower k is given by:

  $$E^k = \sum_i^{allcells} E_i^k, \tag{4.3}$$

  where i runs over all the cells within the tower. The E_T and position of the tower are given by:

  $$E_T^k = \sqrt{(E_x^k)^2+(E_y^k)^2}, \tag{4.4}$$

  $$\phi_k = tan^{-1}\frac{E_y^k}{E_x^k}, \tag{4.5}$$

  $$\theta_k = cos^{-1}\frac{E_z^k}{\sqrt{(E_x^k)^2+(E_y^k)^2+(E_z^k)^2}}, \tag{4.6}$$

$$\eta_k = -log(tan\frac{\theta^k}{2}). \tag{4.7}$$

All the towers with $E_T \geq 1$ GeV are selected and listed in descending order in E_T. These are known as *seed* towers. The highest E_T tower forms the first precluster *seed.* Next, all the neighboring towers with $E_T \geq 1$ GeV within a square of ±0.3 are added to the precluster *seed* to form the first precluster. All towers added to the precluster are removed from the list. The highest E_T tower among the remaining towers is then used to start the next precluster. This step is repeated until all the towers with $E_T \geq 1$ GeV are included in a precluster. This preclustering is done in order to reduce the number of starting points for the jet algorithm.

- **Clustering:** The clustering step starts with the preclusters of the previous step. Taking each precluster as the center of the jet (η_0, ϕ_0), a jet is formed from all the towers within a cone of radius $R=\sqrt{(\eta-\eta_0)^2+(\phi-\phi_0)^2}=0.7$. The jet centroid is then recalculated by using the Snowmass definition;

$$\eta_{jet} = \frac{\sum_i^{towers} \eta_i E_{Ti}}{\sum_i^{towers} E_{Ti}},$$

$$\phi_{jet} = \frac{\sum_i^{towers} \phi_i E_{Ti}}{\sum_i^{towers} E_{Ti}} \tag{4.8}$$

This step is repeated until the jet center is stable to within 0.0001 between two consecutive iterations. Once the jet center becomes stable, the relevant kinematic variables of the jet are recalculated using the DØ angle definition as follows:

$$E_{jet} = \sum_{i}^{towers} E_i,$$

$$E_{Tjet} = \sum_{i}^{towers} E_{Ti},$$

$$\phi_{jet} = tan^{-1}\frac{E_y}{E_x},$$

$$\theta_{jet} = cos^{-1}\frac{E_z}{\sqrt{(E_x)^2 + (E_y)^2 + (E_z)^2}},$$

$$\eta_{jet} = -log(tan\frac{\theta_{jet}}{2}), \tag{4.9}$$

where,

$$E_j = \sum_{i}^{towers} E_{ji}, \quad for \quad j = x, y, z.$$

Here E_x, E_y and E_z are the magnitudes of the components of the energy vector along the positive x-, y- and z-axis. If the E_T of the reconstructed jet is more than 8 GeV then the jet is retained. The reconstruction algorithm then looks for the next precluster and the process repeats until all the preclusters are examined.

- **Split/Merged Jets:** Sometimes the reconstructed jets overlap. In that case, if the the two jets share more than 50% of the E_T of the smaller E_T jet, they are merged into a single jet, otherwise they are split into two separate jets by assigning each shared cell to the jet with the nearest center. In either case, the E, E_T, η and ϕ of the new jets are recalculated using Equation 4.9.

- The process is repeated for jet cone sizes of 0.3, 0.5, 0.7, 1.0 and 1.3.

4.4 Event $\not\!\!E_T$

Missing transverse energy, $\not\!\!E_T$, in the calorimeter may indicate the presence of either a neutrino or a muon or both. A muon will pass through the D0 calorimeter leaving only a minimum ionizing track of energy 2-3 GeV in the electromagnetic calorimeter, while a neutrino does not interact within the D0 calorimeter. However, in a real calorimeter, $\not\!\!E_T$ includes the effects of noise, position and energy resolution too. The event $\not\!\!E_T$ is calculated in the following way:

$$\not\!\!E_T = \sqrt{(\sum_i E_x^i)^2 + (\sum_i E_y^i)^2}, \tag{4.10}$$

where the sum is over all the calorimeter cells including those of the ICD and massless gaps.

Chapter 5

Data Sample

5.1 Introduction

During Run 1A, the Tevatron provided $p\bar{p}$ inelastic collisions at a center-of-mass energy of 1.8 TeV. The process of jet selection starts at the trigger level. If an event passes the trigger requirements the entire detector is read out. Jets are then reconstructed with a fixed cone jet algorithm. Noise and background in the jet sample are removed by applying a series of offline cuts. Jet selection and the associated selection efficiencies are discussed in this chapter.

5.2 Trigger and Luminosity

Five trigger conditions were used to select jet events and write them to tape. The triggers are JET_MIN, JET_LOW, JET_MEDIUM, JET_HIGH and JET_MAX . The LØ , L1 and L2 conditions for these jet triggers are discussed in chapter 3. These conditions are summarized in Table 5.1. A cut on the interaction vertex z-coordinate is applied at LØ to select events well measured by the calorimeter. L1 requires n number of trigger towers with E_T greater then e, while L2 requires n number of jets of cone size r with

E_T greater than e. As only a fraction of the bandwidth was dedicated to jet triggers, so all high rate triggers were prescaled except for the highest E_T trigger.

Table 5.1: Jet Triggers. The L0 z - vertex cut is given in cm. MB denotes a minimum bias trigger.

Trigger Name	Level 0	Level 1	Level 2	Prescaled
JET_MIN	MB (10.5)	JT(1,3)	L2JT(1,20)	yes
JET_LOW	MB (10.5)	JT(1,7)	L2JT(1,30)	yes
JET_MEDIUM	MB (10.5)	JT(2,7)	L2JT(1,50)	yes
JET_HIGH	MB (10.5)	JT(3,7)	L2JT(1,85)	yes
JET_MAX	MB	JT(4,5)	L2JT(1,115)	no

During Run 1A, D0 collected a total integrated luminosity of 13.7 pb^{-1}. The integrated luminosity at D0 is obtained by measuring non-diffractive inelastic collisions and the method has been described in reference [37]. The interaction rate for colliding beams, R is expressed in terms of interaction probability per unit flux defined as the cross section σ (units of *barns*, 1 *barn* $= 10^{-24}$cm^2). Hence, the instantaneous luminosity is given by:

$$R = \sigma L. \tag{5.1}$$

If the experiment is run a for period of time, then the expected total number N of events of a specific type, which in our case are $p\bar{p}$ inelastic collisions, is obtained by integrating the instantaneous luminosity over that given period of time:

$$N = \sigma \int L dt. \tag{5.2}$$

The integrated luminosity for this period of running is given as:

$$L = \int L dt. \tag{5.3}$$

The luminosity was determined by measuring the rate of a subset of minimum bias events, which have a cross section (σ) of 48.2 mb as determined by averaging the measurements obtained from E710 and CDF [37, 38, 39].

The effective trigger luminosity for run i is defined as:

$$L_j^{eff}(i) = \frac{L(i) \times Z_j(i)}{P_j(i)}, \tag{5.4}$$

where Z_j is the fraction of events passed by the L0 z cut demanded by trigger j and P_j is the prescale factor. $L(i)$ is the integrated luminosity of all the runs i that contribute to trigger j. Table 5.2 gives the effective trigger luminosities for the various jet triggers used in this analysis. The luminosity measurement has an overall error of 5.4%.

Table 5.2: Effective trigger luminosities.

Trigger Name	Effective Luminosity (pb^{-1})
JET_MIN	0.0808
JET_LOW	0.0774
JET_MEDIUM	1.016
JET_HIGH	7.95
JET_MAX	13.7

5.3 Jet and Event Selection

Jet selection requires removal of spurious jets due to calorimeter noise and cosmic rays. In this section the removal criteria and associated efficiency, bad runs and fake jets are discussed. In some cases entire events were removed if the event missing $\not\!E_T$ was unusually large.

5.3.1 Bad Runs

This analysis uses about 1000 individual data runs. However, for a small portion of these runs there were known problems, such as systematic failures of the data aquisition system, level 2 node failure or problems with the base line subtractors. Also, some of the data were taken under bad beam conditions. These types of problems can affect the proper determination of the event interaction vertex or may affect the quality of calorimeter data. Hence, these runs were dropped from the data sample [40].

5.3.2 Noisy Calorimeter Regions

There are a number of different sources which can give rise to jet like signatures or modify existing ones. These sources are listed below [41]:

- **Electronic failures** which cause a response shift in one or a group of calorimeter channels and give rise to jet like signatures. This is characterised by an unphysically large energy deposit in one or more calorimeter cells.

- **Cosmic ray showers** which deposit a large amount of energy in the calorimeter that can mimic a jet.

- **Accelerator losses**, which deposit huge amounts of energy in the region, $1.5 < \phi < 2.2$ radians due to main ring activity.

It is easy to identify noise localized in (η_d, ϕ) space. Fig. 5.1 shows a scatter plot of jet position in (η_d, ϕ) space for jets with $100 \text{ GeV} \leq E_T \leq 150 \text{ GeV}$ and $200 \text{ GeV} \leq E_T \leq 250 \text{ GeV}$. Areas with unusually high occupancy, "hot spots", can be seen in these plots. In the Run 1A data sample, a total of 12 such noisy areas have been identified. These noisy areas represent individual cells or groups of cells with unusually high response. The $\eta_d - \phi$ positions of these noisy areas are given in Table 5.3. Apart from these, noise is also uniformly distributed in the calorimeter. There are jet variables which can be used to discriminate between spurious and real jets and they will be discussed next.

Table 5.3: $\eta_d - \phi$ positions of noisy calorimeter regions.

Region	ϕ	η_d
1	(0,0.2)	(0,0.6)
2	(0.45,0.55)	(0.6,1)
3	(1.1,1.5)	(1.8,2.3)
4	(1.1,1.5)	(-0.2,0.3)
5	(2.8,3)	(-1.5,-1)
6	(3.9,4.1)	(-1,-0.8)
7	(4.3,4.5)	(0.6,1)
8	(4.7,4.9)	(0.5,0.9)
9	(4.7,4.8)	(2.4,2.6)
10	(5,5.1)	(-0.4,-0.1)
11	(5,5.1)	(0.7,1)
12	(5.1,5.5)	(-0.6,-0.2)

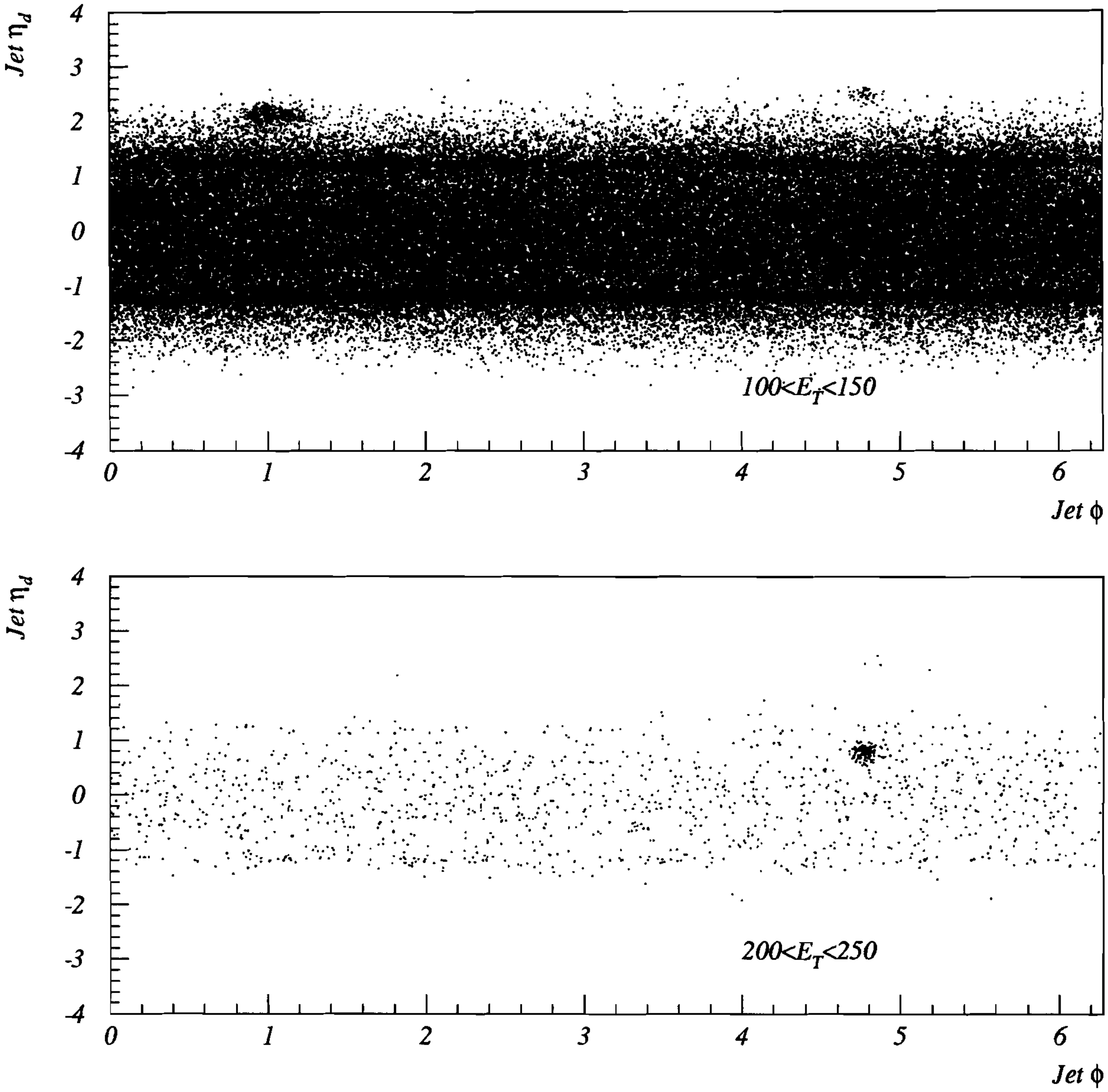

Figure 5.1: $\eta_d - \phi$ distribution of jets with 100 GeV $< E_T <$ 150 GeV and 200 GeV $< E_T <$250 GeV.

5.3.3 Jet Selection Criteria

The jet variables which can be used to identify spurious jets are listed below [41].

- The **electromagnetic fraction (EMF)** of a jet defined as the fraction of total jet energy deposited in the electromagnetic modules of the calorimeter.
- The ratio between the second most energetic cell to that of the most energetic cell in a jet, defined as the **hot cell fraction (HCF).**
- The fraction of jet energy deposited in the coarse hadronic modules of the calorimeter, defined as the **coarse hadronic fraction (CHF).**

To determine the appropriate cut thresholds for identifying spurious jets, a study was performed with noise runs, where data was taken with no colliding beams [41]. In this sample all jets are fake. It was found that all the noise is located below 0.05 and above 0.95 in the EMF distribution and mostly concentrated below 0.01 in the HCF distribution. The following cuts were used to identify good jets [41, 42].

- The EMF is required to be between 0.05 and 0.95.
- The HCF is required to be greater than 0.1.
- The CHF is required to be less than 0.4.

These cuts, known as the "standard cuts", are applied offline on a jet-by-jet basis. The EMF and the CHF cuts are very efficient in removing noisy cells. The CHF cut also removes spurious jets arising from main ring activity. The HCF distribution is very sensitive to the energy distribution over the calorimeter. These cuts have excellent noise rejection efficiency, however, a few events pass these cuts at high E_T.

A missing E_T ($\not{E}_T$) based cut is applied to remove cosmic ray showers which survive the standard cuts. This cut requires the ratio between the event $\not{E}_T$ and the E_T of the leading jet, R_{MTE}, to be less than 0.7. This cut is applied on an event-by-event basis.

Typical EMF, HCF, CHF and $1/R_{MTE}$ distributions are shown in Figs. 5.2, 5.3 and 5.4. In summary, after rejection of bad runs, fake jets are removed by quality and missing E_T cuts.

5.3.4 Efficiencies of Quality Cuts and Noise Rejection

The efficiency of noise rejection was examined in two different ways. If the quality cuts are applied on a data sample taken with no colliding beams, in which case the entire data set consists of noise, the fake jet rejection was found to be 99% [41]. However, this sample was taken over a short period of time and consists of a few thousand events.

In a Monte Carlo study, the effect of noisy cells on the inclusive jet cross section was investigated [43]. A sample of Monte Carlo events was corrupted by randomly introducing a noisy cell in $\eta-\phi$ space. The effect of these noisy cells was either formation of a spurious jet or modification of a good jet. In Run 1A collider data $\sim$ 15% of the good events have fake jets. Thus, $\sim$ 15% of the Monte Carlo events were corrupted with noisy cells of $E_T > 2$ GeV. The noisy cell E_T and η distribution were determined with "no-beam" data. The effect on the inclusive jet cross section in the central pseudorapidities was found to be $\sim$ 1% below 450 GeV after removal of spurious jets using the quality cuts.

Although the jet quality cuts are very effective in removing noise from the data they also remove a small fraction of the good jets. The global efficiency of these jet quality cuts, defined as the product of the efficiencies of the standard cuts and the R_{MTE} cut, is calculated as a function of jet E_T, η and cone size R [42]. The global efficiency is found out to be above 95% in central pseudorapidities for all the four jet cone sizes ($R = 1.0$, 0.7, 0.5 and 0.3).

The method used to calculate the efficiencies of the jet quality cuts are also described in reference [42]. The standard cuts and the $\not{E}_T$ based cut were assumed to be independent of each other. The standard cuts were applied in the following order: (1) EMF cut, (2) HCF cut and (3) CHF cut, but the order is a matter of choice. As shown in Figs. 5.2-5.3, fitting procedures were used to derive distributions for EMF and HCF and the fits are considered to represent the distributions of real jets. The fit distributions were used to estimate the efficiencies of the cuts. The fraction of good jets lost by the cuts was estimated by evaluating the area under the fit outside the cut thresholds. For the CHF cut no fitting procedure was used. If ε_{emf}, ε_{hcf} and ε_{chf} are the efficiencies of the EMF, HDF and the CHF cuts respectively, the global efficiency, ε^{std}_{glob}, of the standard cuts can calculated in the following way:

$$\varepsilon^{std}_{glob} = \varepsilon_{emf} \times \varepsilon_{hcf} \times \varepsilon_{chf}, \tag{5.5}$$

if the HCF cut is applied on the sample obtained after applying the EMF cut and the CHF cut is applied on the sample selected by the HCF cut.

To test if the fitting procedure provides a reasonable distribution, the $\not{E}_T$ based cut was used to clean the sample. The $\not{E}_T$ based cut cleans the EMF, HCF and CHF distributions. This is shown in Figs. 5.2 and 5.3 with dashed lines. The dashed lines are similar to the fits which show that the fits do reasonably well in describing the real jet distribution. The difference in efficiencies obtained with the fitting method before and after cleaning the sample by the R_{MTE} cut gives a measure of the systematic error in these measurements.

The same procedure has been applied to evaluate the efficiency of the $\not{E}_T$ based cut. The $E_T^{jet}/\not{E}_T$ distributions were examined both before and after the standard cuts were applied. The efficiency of this cut is also measured using a fitting procedure by calculating the fraction of good events outside the cut thresholds. The offline cut efficiency (standard + event selection) is given by:

$$\varepsilon_{tot} = \varepsilon^{std}_{glob} \times \varepsilon_{MTE}. \tag{5.6}$$

The inclusive jet cross sections are corrected for these efficiencies [7]. Figs. 5.5 and 5.6 show the event selection ($|\eta| \leq 4$) and jet selection ($|\eta| \leq 1$) efficiencies for the four different cone sizes. Also shown are the fits to the efficiency points. Tables 5.4 and 5.5 give the global efficiency of the standard cuts, ε^{std}_{glob}, for different cone sizes and Table 5.6 gives the event selection efficiency, ε_{MTE}, for different cone sizes [42]. As can be seen from the efficiency plots, the error contributed by these event and jet selection cuts are of the order of 1% for all cone sizes in $|\eta| \leq 0.5$ at all E_T's.

5.4 Conclusion

The jet and event selection process has been discussed in this chapter along with the offline cuts used to rid the sample of spurious jets. In the process of cleaning the sample with offline cuts a few real jets are also removed, which is corrected for by the measured efficiency of these cuts. From the efficiency plots, it can be seen that the error on the cross section from jet and event selection is of the order of 1%. The energy and E_T of these jets must also be corrected for a number of detector related effects, such as detector noise, underlying events, hadronic response of the detector, and algorithm related losses. These corrections are described in the next chapter.

Table 5.4: Global efficiency (ε_{glob}^{std}) of standard cuts for 1.0 and 0.7 jets in $|\eta| \leq 1$.

E_T in GeV of 1.0 jets	ε_{glob}^{std} for 1.0 jets	E_T in GeV of 0.7 jets	ε_{glob}^{std} for 0.7 jets
11.62	96.51±.17	11.5	96.92±.24
19.66	97.2±.17	22.5	97.12±.24
32.02	97.8±.17	33.5	97.41±.24
49.55	98.22±.17	49.1	97.53±.24
68.21	98.27±.17	67.3	97.2±.25
90.09	98.25±.17	89.6	96.9±.25
111.78	98.1±.17	111.7	96.34±.26
141.69	97.65±.42	142.7	96.00±.33
174.31	97.39±.42	166.	95.96±.69
225.91	96.02±.42	185.	96.1±.74
		205.	96.19±.96
		222.	95.59±2.1
		235.	97.03±1.9
		245.	96.64±2.1
		290.	98.87±2

Table 5.5: Global efficiency (ε^{std}_{glob}) of standard cuts for 0.5 and 0.3 jets in $|\eta| \leq 1$.

E_T in GeV of 0.5 jets	ε^{std}_{glob} for 0.5 jets	E_T in GeV of 0.3 jets	ε^{std}_{glob} for 0.3 jets
11.5	95.96±.29	11.5	92.1±.99
22.5	96.69±.29	22.5	93.78±.98
33.5	96.78±.29	33.5	94.72±.98
49.1	97.01±.29	49.1	95.38±.99
67.3	96.86±.3	67.3	95.72±.99
89.6	96.67±.3	89.6	95.23±.99
111.7	96.26±.31	111.7	95.32±.99
142.7	95.87±.36	142.7	95.03±1.02
166.	95.89±.62	166.	95.34±1.19
185.	95.65±.65	185.	94.95±1.2
209.	93.07±1.8	205.	93.44±1.8
230.	96.85±1.8	220.	92.74±2.9
260.	95.58±1.7	230.	96.96±2.6
		245.	96.86±2.5

Table 5.6: Efficiency of the $\not{E}_T$ based cut (ε_{MET}) for all cone sizes in $|\eta| \leq 4$.

E_T GeV	for R= 1.0	E_T GeV	for R= 0.7	for R= 0.5	for R= 0.3
33.1	99.62±.1	33.5	99.28±.1	99.07±.1	98.43±.2
49.6	99.72±.1	49.1	99.6±.1	99.57±.1	99.29±.2
68.1	99.85±.1	67.3	99.65±.1	99.64±.1	99.31±.2
90.01	99.89±.1	89.6	99.78±.1	99.81±.1	99.44±.2
111.59	99.88±.1	111.7	99.72±.1	99.67±.1	99.35±.2
141.5	99.57±.1	142.7	99.59±.1	99.6±.104	99.2±.22
183.51	99.09±.2	183.	99.42±.104	98.55±.14	

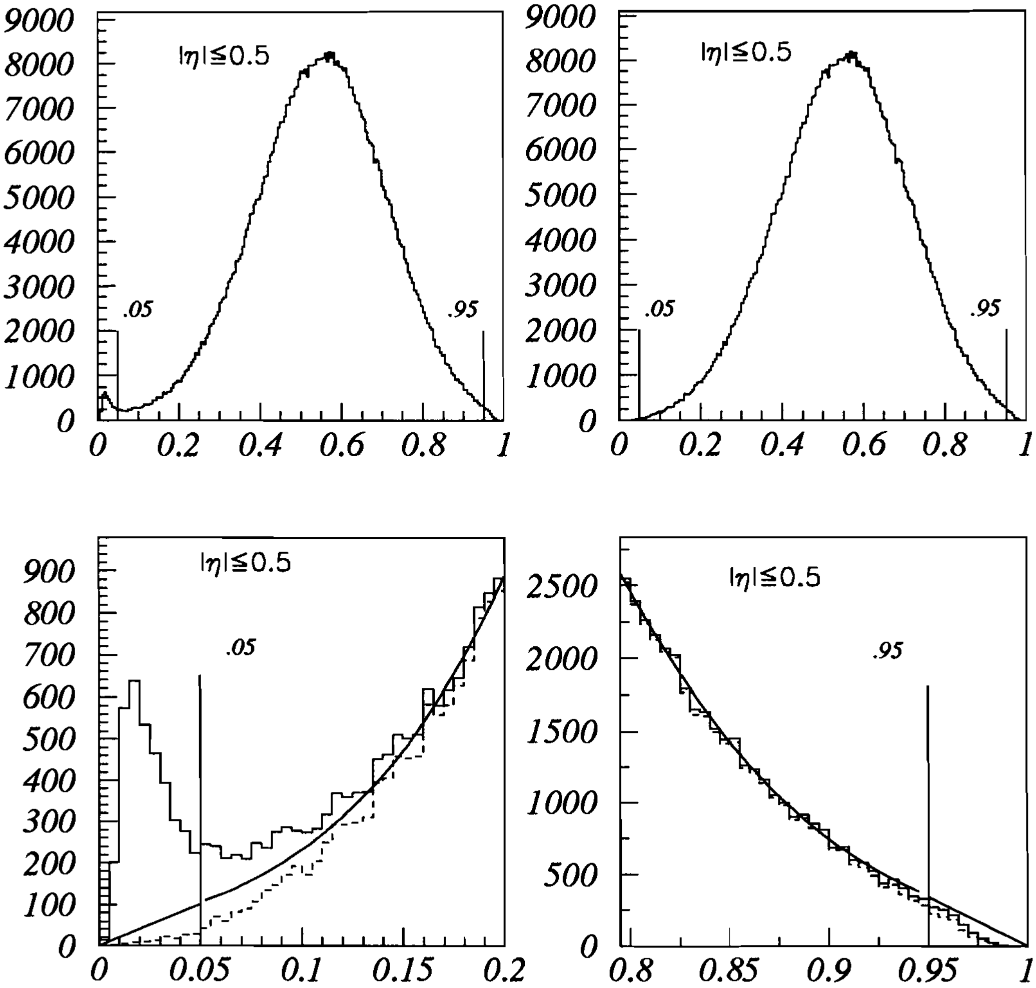

Figure 5.2: Typical Jet EMF distribution for 0.7 cone jets (40 GeV $\leq E_T \leq$ 100 GeV) in $|\eta| \leq 1$. The plot on the top left shows the distribution obtained from the raw data sample. The plot on the top right shows the distribution cleaned with the R_{MTE} cut. The fits used to obtain the cut efficiency are shown at the bottom. The vertical lines point to the cut thresholds and also the point where a gaussian fit is replaced by a linear extrapolation.

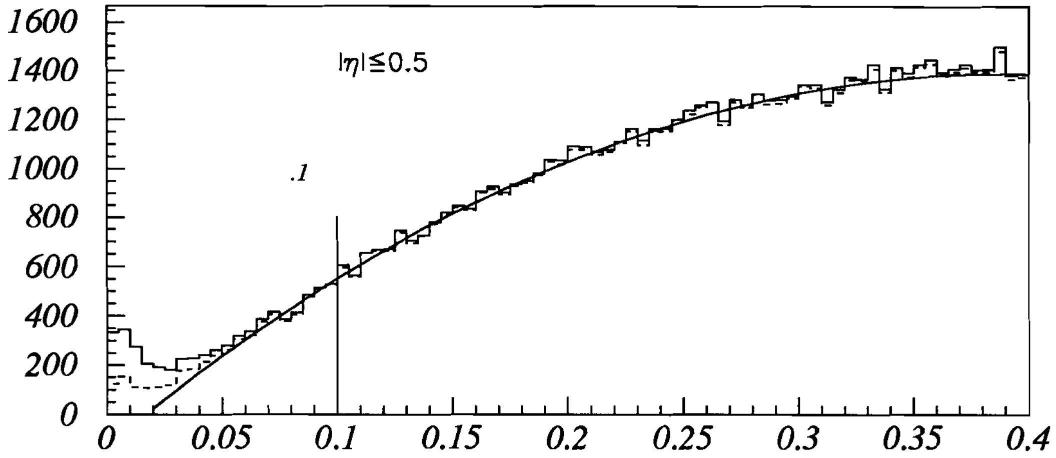

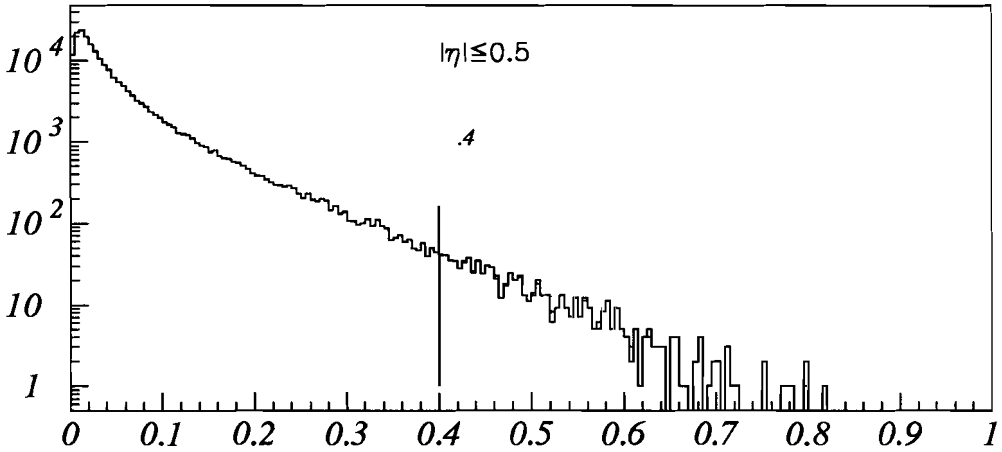

Figure 5.3: The top plot shows a typical Hot Cell Fraction distribution for 0.7 cone jets (60 GeV $\leq E_T \leq$ 100 GeV) in $|\eta| \leq 1$. The solid histogram is the raw data sample with only the EMF cut applied, the dashed histogram is the sample cleaned with EMF and the R_{MTE} cuts. Also shown is the cut threshold. The bottom plot shows CH Fraction distribution with the cut threshold.

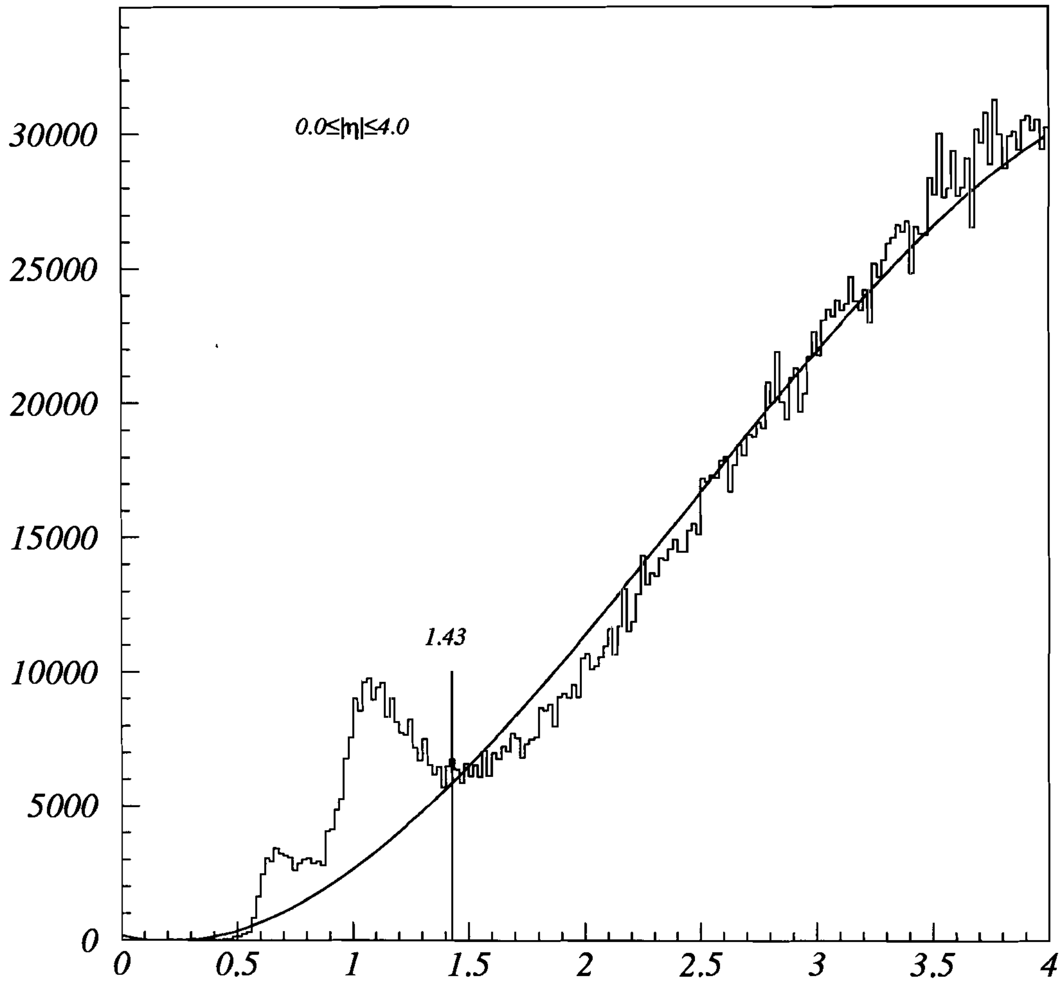

Figure 5.4: Typical $1/R_{MTE} = \frac{\not{E}_T}{E_T^{jet}}$ distribution for 0.7 cone jets (60 GeV $\leq E_T \leq$ 80 GeV) in $|\eta| \leq 4$ after the sample has been cleaned by the standard cuts. The fit gives the distribution for clean and real jets. The cut threshold is also shown by the vertical line.

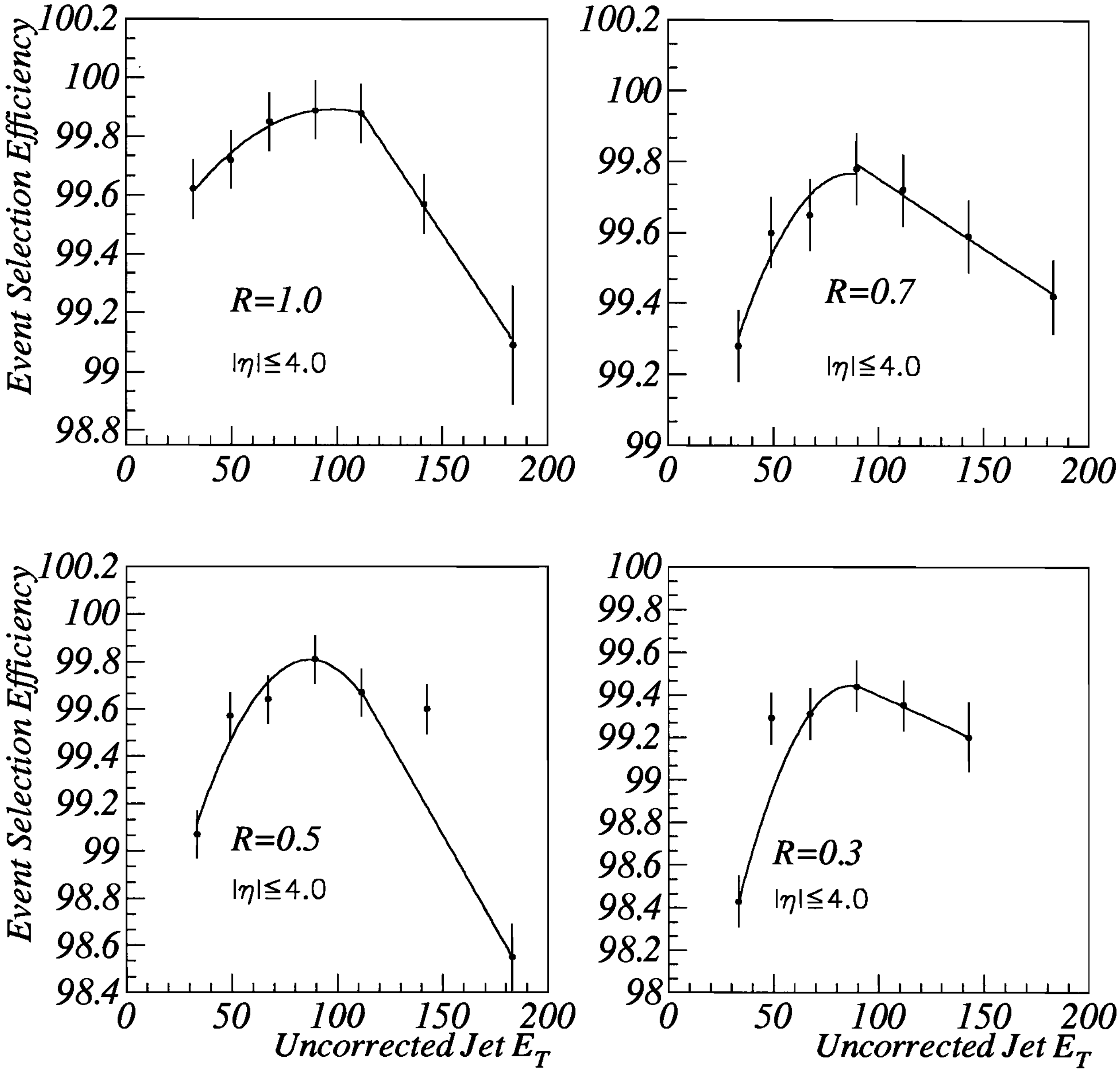

Figure 5.5: The event selection efficiency for 1.0, 0.7, 0.5 and 0.3 cone jets in $|\eta| \leq 4$. (Note the highly suppressed zero.)

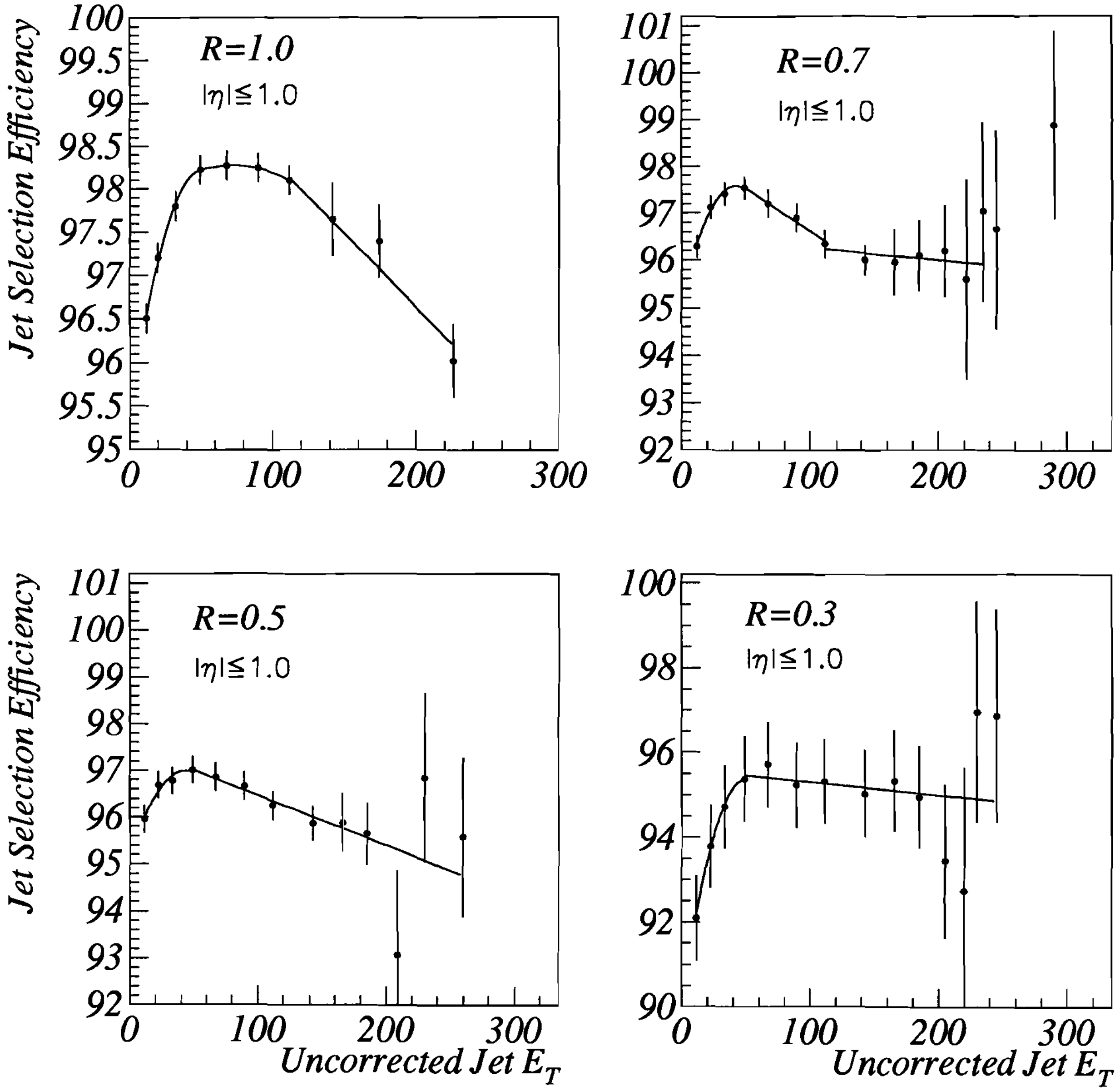

Figure 5.6: Figure shows the jet selection efficiency for 1.0, 0.7, 0.5 and 0.3 cone jets in the central region, $|\eta| \leq 1$. Note the highly suppressed zero.)

Chapter 6

Jet Energy Correction and the Observed Cross Section

6.1 Introduction

As discussed earlier, in a $p\bar{p}$ collision jets are produced as a result of fragmentation and hadronization of final state partons into a collimated spray of particles and are identified as localized energy deposits in adjacent calorimeter cells or towers. Although the final state jets are remnants of the partons participating in the hard scattering, it is not easy to associate the jet energy with a specific underlying parton energy. D0 defines and calibrates jet energies at the final state particle level, not at the parton level. This involves correction for the behaviour of the calorimetry and NOT for QCD radiation outside the jet defining cone. Proper measurement of jet energy is very important for the correct measurement of the jet E_T spectrum. In this chapter, the jet energy scale correction and the subsequent measurement of the inclusive jet cross section will be discussed.

6.2 Corrections to Jet Energy

Jets are composed of a large number of particles of different energies. For example, approximately 67% of the particles in a 50 GeV jet have less than 5 GeV energy [44]. The true jet energy is the sum of energies of all the particles inside the jet cone. However, there are several factors which contribute to the energy measurement of jets:

- The single particle response of the calorimeter, as studied with a test beam, is non-linear at the percent level below 10 GeV [33].
- Energy losses in the uninstrumented areas of the calorimeter, such as intermodule cracks or cryostat walls.
- Noise due to uranium radioactivity, zero-suppression, energy from the underlying event and pileup from multiple interactions.
- Showering losses of particles inside (outside) the particle jet cone before hitting the calorimeter, which then shower outside (inside) the cone in the calorimeter.

Because of these effects, the energy of the reconstructed jet differs from that of the parent particle jet. Hence energy scale corrections are required [45]. The correction scales the energy of the reconstructed jet to that of the parent particle jet. The jet energy is calibrated in such a way that the true jet energy, E_{jet} of the parent particle jet that struck the calorimeter is obtained from the measured jet energy, $E_{measured}$, with:

$$E_{jet} = \frac{E_{measured} - O}{(1 - S)R_{had}}, \tag{6.1}$$

where, R_{had} is the calorimeter hadronic response, O is the offset due to uranium noise, underlying events and pileup and S is the calorimeter showering loss of jet energy. These components of the jet calibration are discussed below.

Electromagnetic Energy Scale

The response of the EM calorimeter to electrons, positrons and photons has been calibrated with the decays of known resonances into these particles [46, 47]. To determine the absolute EM scale, the $Z \rightarrow ee$ decays are used and the resulting invariant mass distribution is fitted to a Breit-Wigner distribution. Then the energy scale is adjusted so that the central Z mass (M_Z) agrees with the value from the LEP experiments. Other resonances ($\pi^0 \rightarrow \gamma\gamma$, $J/\psi \rightarrow ee$) were used to check the EM scale at different energies. The correctness of the EM calibration is assumed for the jet scale calibration.

Offset

Not all of the jet energy can be attributed to the the hard scatter. There are other sources which contribute to the jet energy. Electronic noise and ionization caused by the radioactive decay of uranium nuclei modifies the energy of the jet. This contribution called "noise" is denoted N. Apart from this, additional energy comes from the spectator interactions and beam remnants, together called the "underlying event", and denoted by U. If there are multiple interactions then the underlying event contribution is multiplied by the number of extra interactions. This is a negative correction in the sense that the total contribution from these effects must be subtracted from the reconstructed jet energy. The noise and underlying event contribution together are called the offset correction, O [45].

This correction was determined from minimum bias events which were selected by requiring a coincidence between the forward and backward LØ hodoscopes. Both U and N are assumed to be uniformly distributed in ϕ. To determine the underlying event contribution, the transverse energy density in $\eta - \phi$ space for minimum bias events with single and double interactions were determined separately, and the contribution is assumed to double for double interactions. So, the difference between the single and double interaction curves give the underlying event contribution [45]:

$$U = (0.310 + 0.034|\eta_d|) GeV/rad/\eta. \tag{6.2}$$

The error on the underlying event E_T density is 0.2 GeV/rad/η. For multiple interactions, U is multiplied by the extra number of interactions.

The noise from electronics and uranium radioactivity will be the same for single and multiple interactions. Once U is evaluated, the noise N can be easily evaluated by subtracting U from the measured E_T density for single interactions [45]:

$$N = (0.196 + 1.44 sin\theta_d) GeV/rad/\eta. \tag{6.3}$$

The error in the noise E_T density is 0.1 GeV/rad/η.

Response

Direct photon or dijet events are used to calibrate the jet hadronic response [45]. At leading order, a direct photon event has a photon balanced in E_T by a jet. After application of the EM scale and offset corrections, any $\not{E}_T$ is assumed to be due to mismeasurement of the jet E_T. Both the photon and the jet are required to be in the central region $|\eta|$ <0.7 and the missing transverse energy projection fraction (MPF) is defined in the following way:

$$MPF = -\frac{\bar{\not{E}}_T \cdot \hat{n^\gamma}}{E_T^\gamma}, \tag{6.4}$$

where, $\bar{\not{E}}_T$ is the missing transverse energy vector in the direction opposite to that of the photon, E_T^γ is the photon transverse energy and $\hat{n^\gamma}$ is the unit vector in the direction of the photon. The $\not{E}_T$ reflects the mismeasurement of the jet E_T. It can be shown that the hadronic response of the calorimeter reduces to:

$$R_{had} = 1 + MPF. \tag{6.5}$$

It should be noted that the hadronic response is dependent only on the event $\not{E}_T$ and the E_T of the photon. However, this method of measuring the response is biased by the fact that there may be unreconstructed third or fourth jets in the event. In order to avoid these biases, events with back-to-back topology only in ϕ were selected.

In order to correct the jet energy for the detector hadronic response, the dependence of R_{had} on some jet variable X is required, which in our case is the jet energy. In γ - jet events, E_T^γ is very precisely measured and the direction of the photon and that of the jet are well known. So we define E':

$$E' = E_T^\gamma cosh\eta_{jet}, \tag{6.6}$$

and in 2→2 processes, $E' = E_{jet}$, the true jet energy. But in multijet event samples although this relation does not hold, E' is highly correlated with jet energy. So, to good accuracy the dependence of R_{had} on jet energy can determined by plotting R_{had} versus E'.

All reconstructed electromagnetic clusters within a jet are corrected by applying the EM scale. These corrections are propagated into the $\not\!\!E_T$. Threshold bias on low E_T jets are removed and corrections are also applied for scale variations between different cryostats. After these corrections are made, the absolute response as a function of jet energy can be measured to $\sim$ 2% at any E_t.

Using Equation 6.5, R_{had} is measured as a function of E', but it can not be applied to a jet in a multijet event as only $E_{measured}$ is known. Therefore, to relate between response and measured energy, average jet energy is measured as a function of E'. This and the previous results were combined to map the average response onto the average jet energy. This method has many systematic errors which include the effects of initial and final state radiation, resolution bias, and unbiasing of low E_T jets. The energy dependence is fairly described by [45]:

$$R_{had} = a + b \times ln(E_{jet}), \tag{6.7}$$

with a=0.71 and b=0.025.

Correction to the jet energy requires adjustment to the $\not\!\!E_T$. Since $\not\!\!E_T$ is determined by summing over all the cells in azimuth and as O is ϕ independent, this term is not needed for $\not\!\!E_T$. On the other hand as S only corrects for algorithm losses, not calorimeter losses, it is also not used for $\not\!\!E_T$. Thus the $\not\!\!E_T$ is only adjusted for response corrections to jets and electrons. The response errors for central jets are tabulated in Table 6.1 [45].

Showering

After the jet energy is corrected for the offset and response, the algorithm dependent corrections are applied. The hadrons deposit energy in the calorimeter by showering into a cascade of particles. The energy contained within a jet cone at particle level is taken as the true jet energy. A showering correction must correct for the loss of energy for those particles which were inside (outside) the jet cone at particle level before hitting

Table 6.1: Response errors in percent for CC jets

Source of error	10 GeV	15 GeV	20 GeV	30 GeV	80 GeV	150 GeV	400 GeV
statistical/method:							
event topology	0.0	0.0	2.02	1.78	1.22	0.88	0.88
k_T/ resolution bias	3.0	1.0	3.0	1.0	0.0	1.0	1.0
binning	1.0	1.0	0.0	0.0	0.0	0.0	0.0
unbiasing	5.0	0.5	0.0	0.0	0.0	0.0	0.0
background:							
instrumental	0.0	0.0	1.73	1.42	1.42	1.42	0.0
physics	0.5	0.5	0.5	0.5	0.5	0.5	0.5
multiple interaction	0.0	0.0	0.5	0.5	0.5	2.0	0.0
MC-data conversion	3.20	3.20	0.0	0.0	0.0	0.0	3.72

the calorimeter, which then showered outside (inside) the jet cone once the jet hits the calorimeter. We do not correct for QCD radiation outside the particle jet cone.

This correction was evaluated with the help of Monte Carlo and test beam single particle shower profiles. Particle jets were generated with HERWIG [48] at different energies and then the individual particles inside the particle jet were made to shower upon hitting the calorimeter using the test beam single particle shower profiles. After simulating the shower the jet finder was run to find the showered jet. The ratio of energies of the unshowered and the showered jet gave the showering correction. There is no correction for this effect for 1.0 cone jets and a very small correction at low E_T which vanishes at high E_T for 0.7 cone jets. However, for 0.5 (0.3) cone jets the correction is 3% (4%) at low E_T to 0% (2%) at higher E_T. The error on the showering correction is 1% for all jet cone sizes in $|\eta| \leq 0.5$ [45].

Remarks on Energy Scale Correction

The energy scale correction is applied in several steps and is obtained in terms of jet energy, jet detector pseudorapidity η_d, and jet cone size. Fig. 6.1 shows the correction factors for 1.0, 0.7, 0.5 and 0.3 cone jets as a function of uncorrected jet E_T in the central region $|\eta| \leq 0.5$. These plots show the actual data correction and represent the average correction as a function of uncorrected jet E_T. The outer curves indicate the correction error. The correction error is the largest source of error for the inclusive jet cross section. At a 100 GeV in E_T the average correction factors are 17%±6%, 21%±6.5%, 23%±6.5% and 28%±7%, respectively for 1.0, 0.7, 0.5 and 0.3 cone jets in $|\eta| \leq 0.5$.

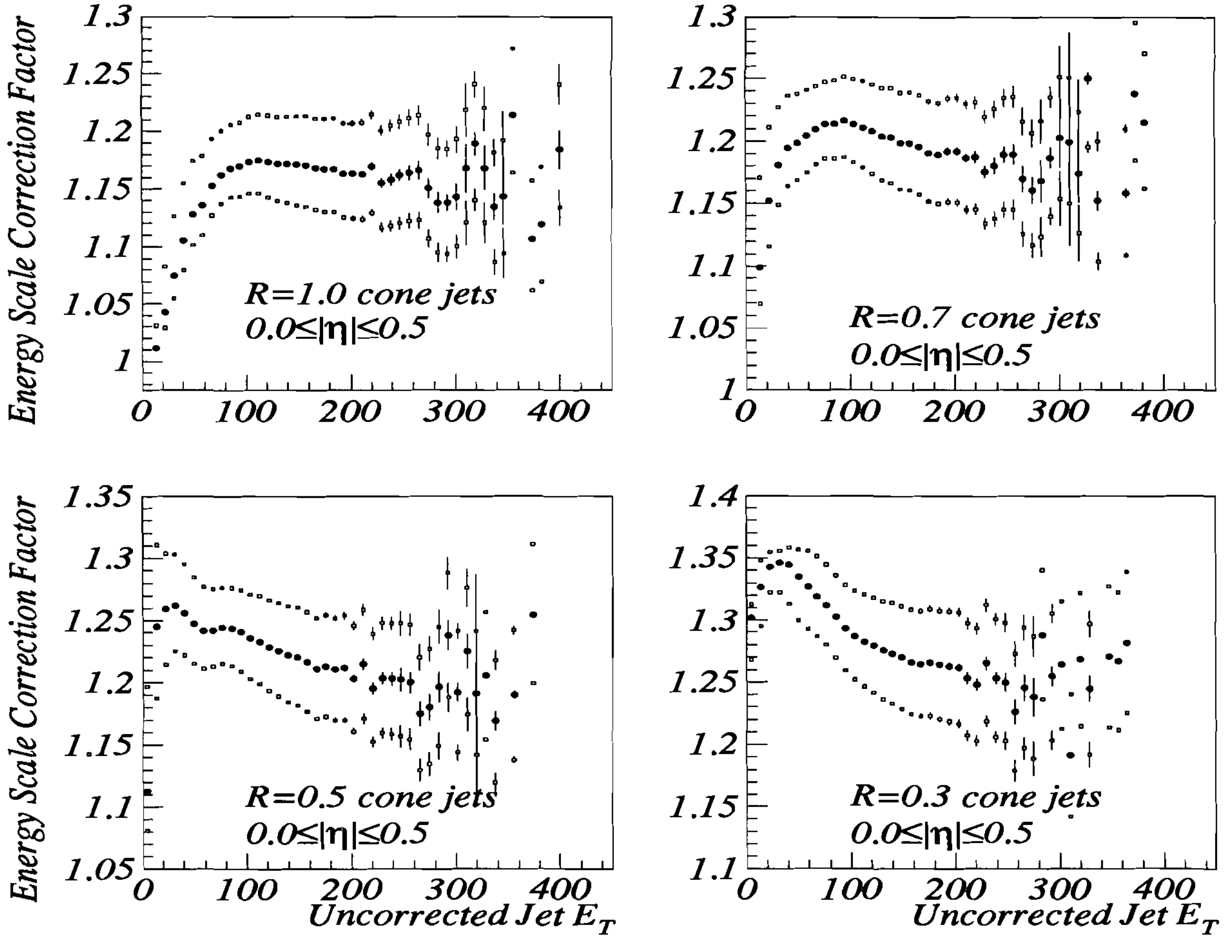

Figure 6.1: Energy Scale Correction Factors for different cone sizes for $|\eta| \leq 0.5$.

6.3 Observed Inclusive Jet Cross Section

The inclusive differential jet cross section is measured as a function of jet E_T in bins of η as [7]:

$$\langle\frac{d^2\sigma(p\bar{p}\rightarrow jet+X)}{dE_T d\eta}\rangle=\frac{N}{L_T^{eff}\times\triangle E_T\times\triangle\eta\times\varepsilon},\tag{6.8}$$

where, $\triangle E_T$ and $\triangle\eta$ define the E_T and η bins, $N=\sum_i N_i$ is total number of jets from all the runs in that E_T and η bin. The cross section is normalized by the trigger effective luminosity, L_T^{eff} and by the product of all the jet quality cut efficiencies. The statistical error on the cross section in each bin is given by:

$$\frac{\sqrt{N}}{L_T^{eff}\times\triangle E_T\times\triangle\eta\times\varepsilon},\tag{6.9}$$

since the number of jets in a bin follows Poissonian statistics and the total number of jets in the whole sample is much greater than N.

The inclusive jet cross section is obtained from the reconstructed variables in several steps [7].

(1) In the range of interest the reconstruction and trigger efficiencies must be 100%.

(2) Events that do not pass the R_{MTE} cut and the jets that do not pass the standard cuts are dropped from the sample.

(3) The energy and E_T of the remaining sample are corrected to that of the parent particle level jet.

(4) The E_T distributions were obtained for each of the triggers.

(5) Data points for each E_T bin are plotted at the average of the mean jet E_T and the bin center in each bin.

(6) Each jet is an entry and each jet is weighted by the corresponding jet quality cut efficiency.

(7) Each data point is weighted by the bin size and trigger effective luminosity.

(8) The final jet E_T spectrum is obtained from four different triggers. Each trigger is used in a different E_T range depending on whichever gives the highest statistics and efficiency (explained in next section).

The cross sections were not measured below 80 GeV in E_T due to uncertainties in reconstruction efficiency, trigger efficiency, energy scale and resolution.

6.4 Effective Trigger Luminosity and Luminosity Matching

Fig. 6.2 shows the ratios of the cross sections for various triggers for $R = 0.7$ cone jets. The ratios JET_MAX/JET_HIGH and JET_HIGH/JET_MEDIUM show that for these triggers, the cross sections are equal within 5%. However, the ratio JET_MEDIUM/JET_LOW does not equal unity. And JET_MIN matched to JET_LOW with the luminosity database numbers also shows a step in the cross section. Since the cross section ratios must equal unity once the triggers are efficient, the integrated luminosity for each trigger, JET_MIN, JET_LOW, JET_MEDIUM and JET_HIGH is adjusted. The E_T range at which each trigger is utilized can also be determined by these ratios. A 5-10% error is added for luminosity matching.

In DØ , at L2, a 0.7 radius cone algorithm was used to reconstruct jets and write them to tape. Different cone sizes are then applied offline to reconstruct jets and so the trigger efficiencies for different cone sizes are related to the trigger efficiency for 0.7 cone jets. As 0.3 and 0.5 cone jets are narrower than a 0.7 jet, they will have less E_T than the corresponding 0.7 cone jet and hence they should have a trigger "turn on" earlier in E_T relative to the corresponding 0.7 cone jet. By the same argument, for a 1.0 cone jet trigger "turn on" will occur at a higher E_T. This fact is illustrated in Figs. 6.3, 6.4 and 6.5 for 1.0, 0.5 and 0.3 cone jets, respectively. This effect is prominent for the lower E_T triggers, however, for higher E_T triggers the trigger "turn on" occurs more or less around the same E_T as the jets become narrower [49]. Based on these figures and separate trigger efficiency studies [50, 51], and with the objective of maximizing statistics, the E_T intervals over which trigger sets contribute to the cross section are tabulated in Table 6.2.

The observed inclusive jet cross sections for jet cone sizes of 1.0, 0.7, 0.5 and 0.3 are shown in Figs. 6.6, 6.7, 6.8 and 6.9, respectively. Table 6.3, summarizes the statistical and systematic errors (from jet and event selection, luminosity and luminosity matching) on the cross sections for different cone sizes. The error on the cross section from the error on the energy scale correction for a few different jet E_T's are shown in Table 6.4.

Table 6.2: E_T values above which different triggers are used, given as a function of jet cone size. These numbers are obtained by matching the cross sections from different triggers as shown in Figs. 6.2, 6.3, 6.4 and 6.5.

Cone Size R	JET_LOW	JET_MEDIUM	JET_HIGH	JET_MAX
1.0	$70 GeV$	$90 GeV$	$130 GeV$	$180 GeV$
0.7	$60 GeV$	$85 GeV$	$120 GeV$	$170 GeV$
0.5	$60 GeV$	$85 GeV$	$120 GeV$	$170 GeV$
0.3	$60 GeV$	$85 GeV$	$120 GeV$	$170 GeV$

6.5 Conclusion

The inclusive jet cross section requires an approximate 10-20% energy scale correction with a ±3-5% error. Due to the steeply falling nature of the jet cross section, the error on energy scale transforms into a 10-30% error on the cross section. Various errors on the cross section from different sources were discussed in this chapter. The cross section thus obtained is however smeared by resolution effects and resolution unsmearing is discussed in the next chapter.

Table 6.3: Percentage error on observed cross section for different cone sizes.

Source	R=1.0	R=0.7	R=0.5	R=0.3	Comment
Statistical(below 250 GeV)	~ 5%	~ 5%	~ 5%	~ 5%	
Selection	1%	1%	1%	1%	Statistical
Luminosity	5.4%	5.4%	5.4%	5.4%	Systematic
Luminosity Matching					
JET_LOW	10%	10%	10%	10%	Systematic
JET_MEDIUM	3%	3%	3%	4%	Systematic
JET_HIGH	3%	3%	3%	4%	Systematic
JET_MAX	0	0	0	0	Systematic

Table 6.4: Percentage error on observed cross section for different cone sizes, from error on the energy scale correction.

Jet E_T (GeV)	R=1.0	R=0.7	R=0.5	R=0.3
~100	~29%	~24%	~24%	~24%
~200	~40%	~40%	~38%	~40%
~300	~70%	~70%	~70%	~60%
~420	~190%	~150%	~90%	~100%

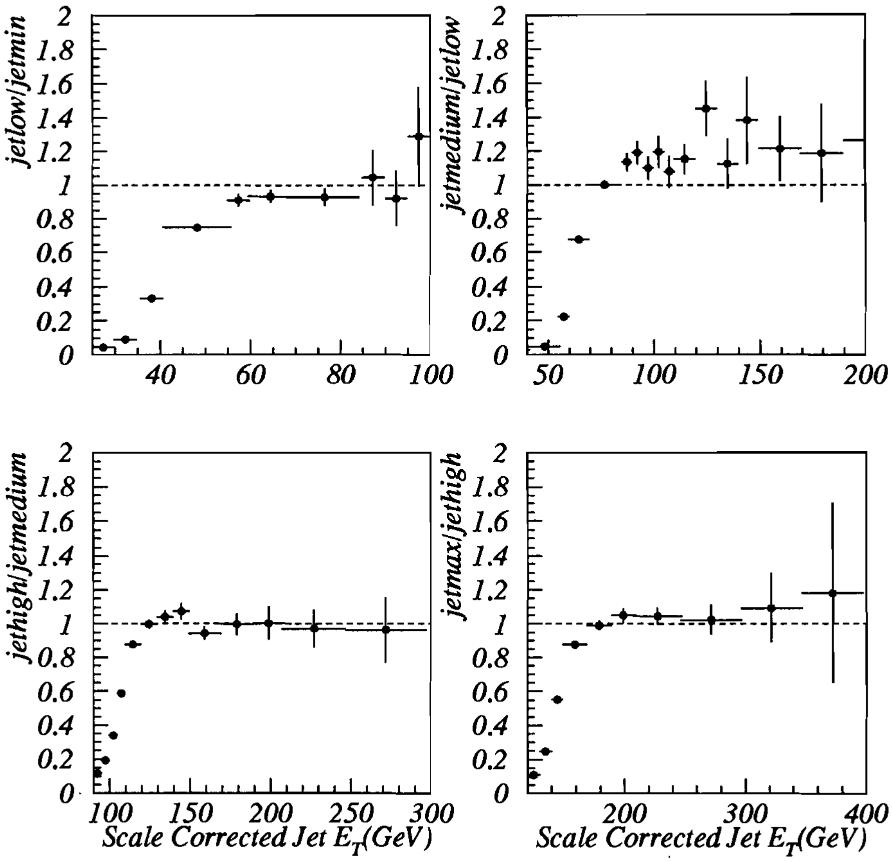

Figure 6.2: Ratio of cross sections with different triggers for 0.7 cone jets.

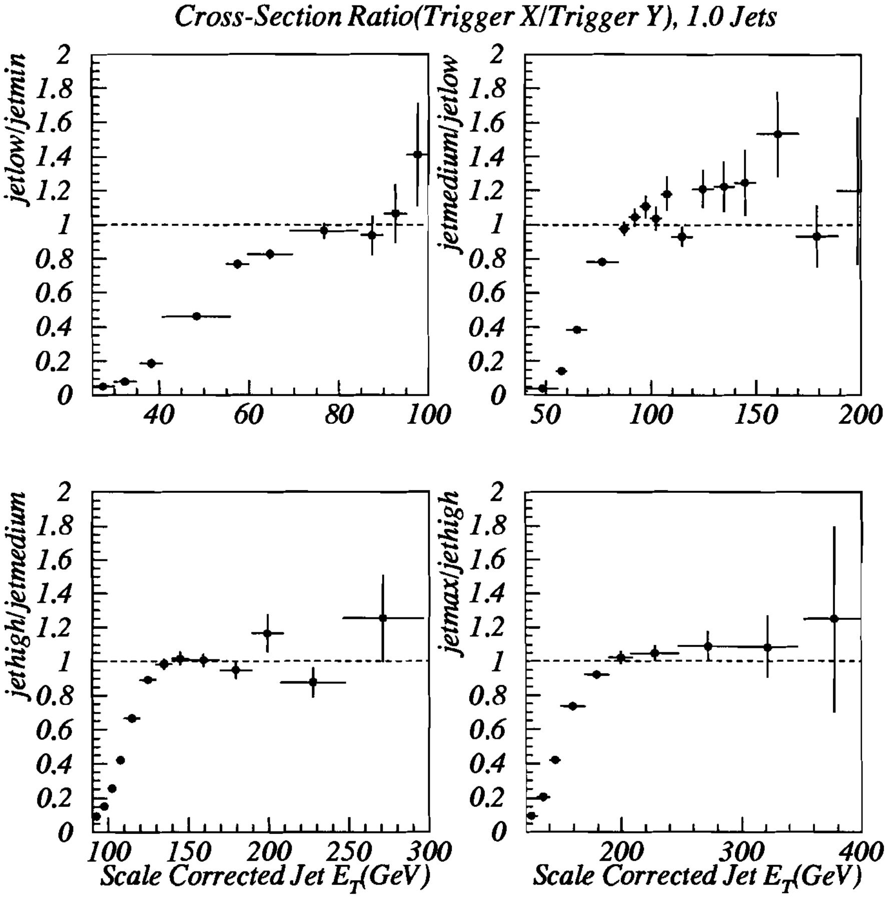

Figure 6.3: Ratio of cross sections with different triggers for 1.0 cone jets.

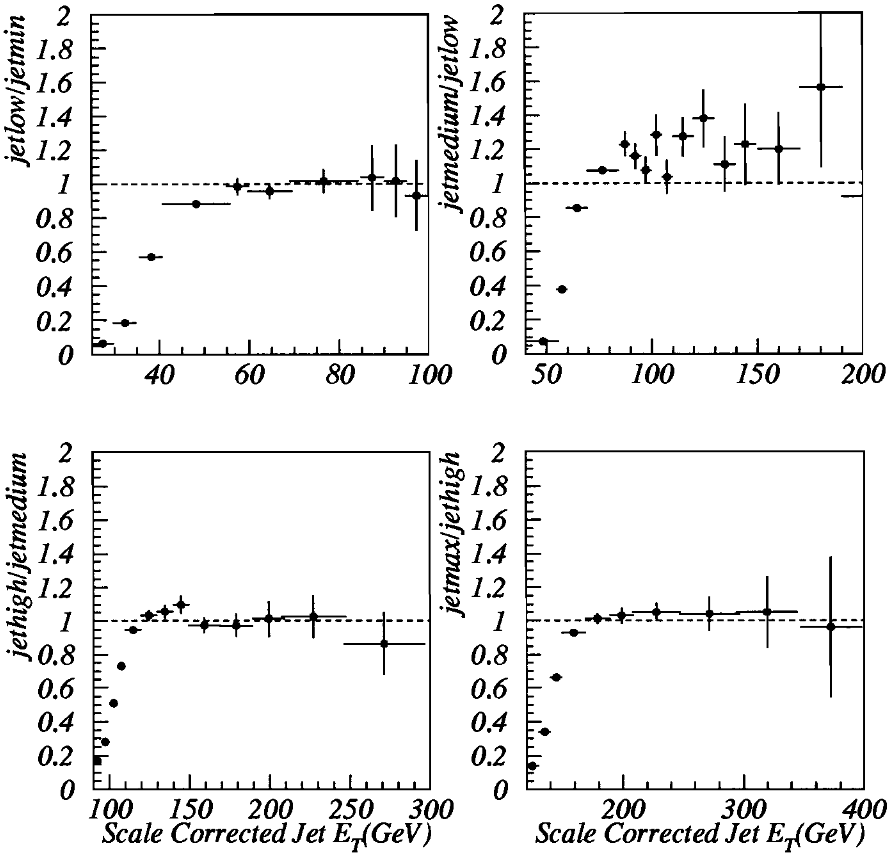

Figure 6.4: Ratio of cross sections with different triggers for 0.5 cone jets.

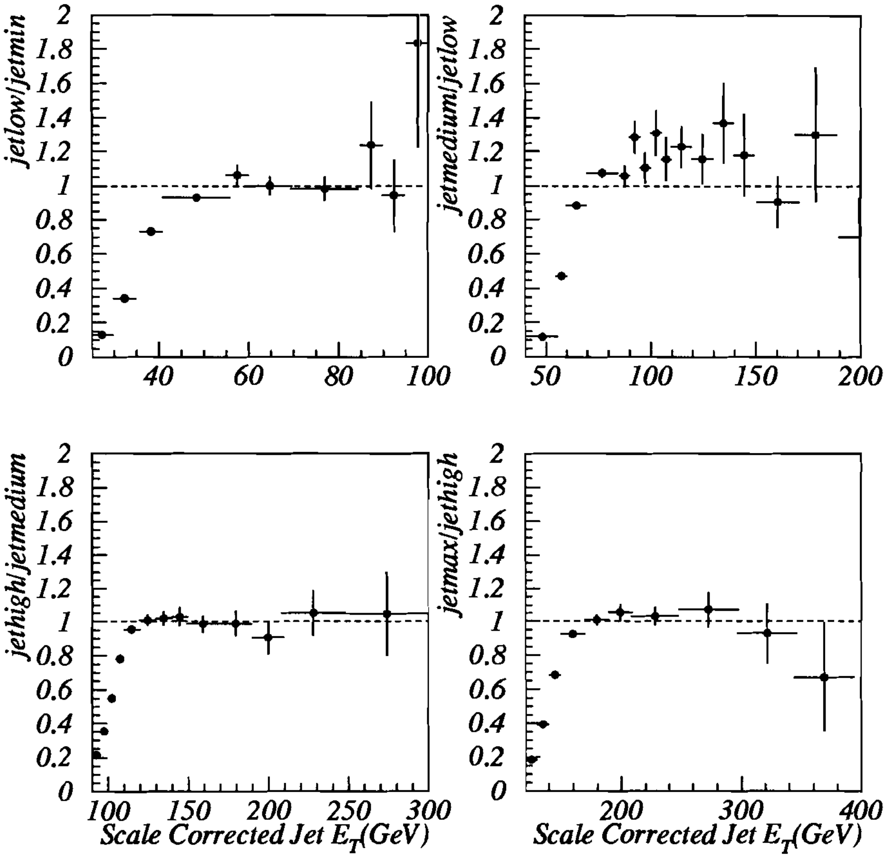

Figure 6.5: Ratio of cross sections with different triggers for 0.3 cone jets.

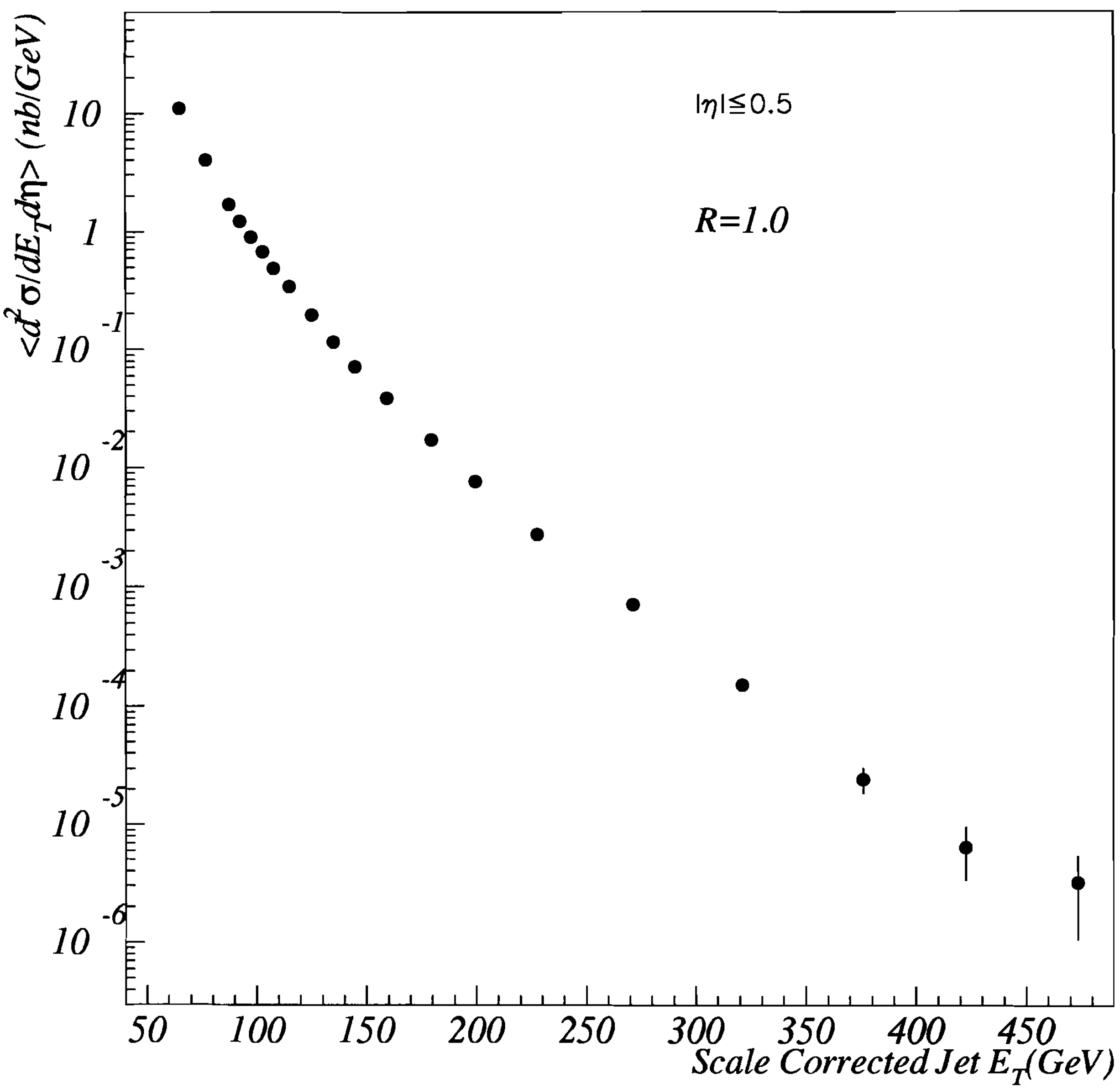

Figure 6.6: Observed Inclusive Jet cross sections in $|\eta| \leq 0.5$ for jet cone size of 1.0.

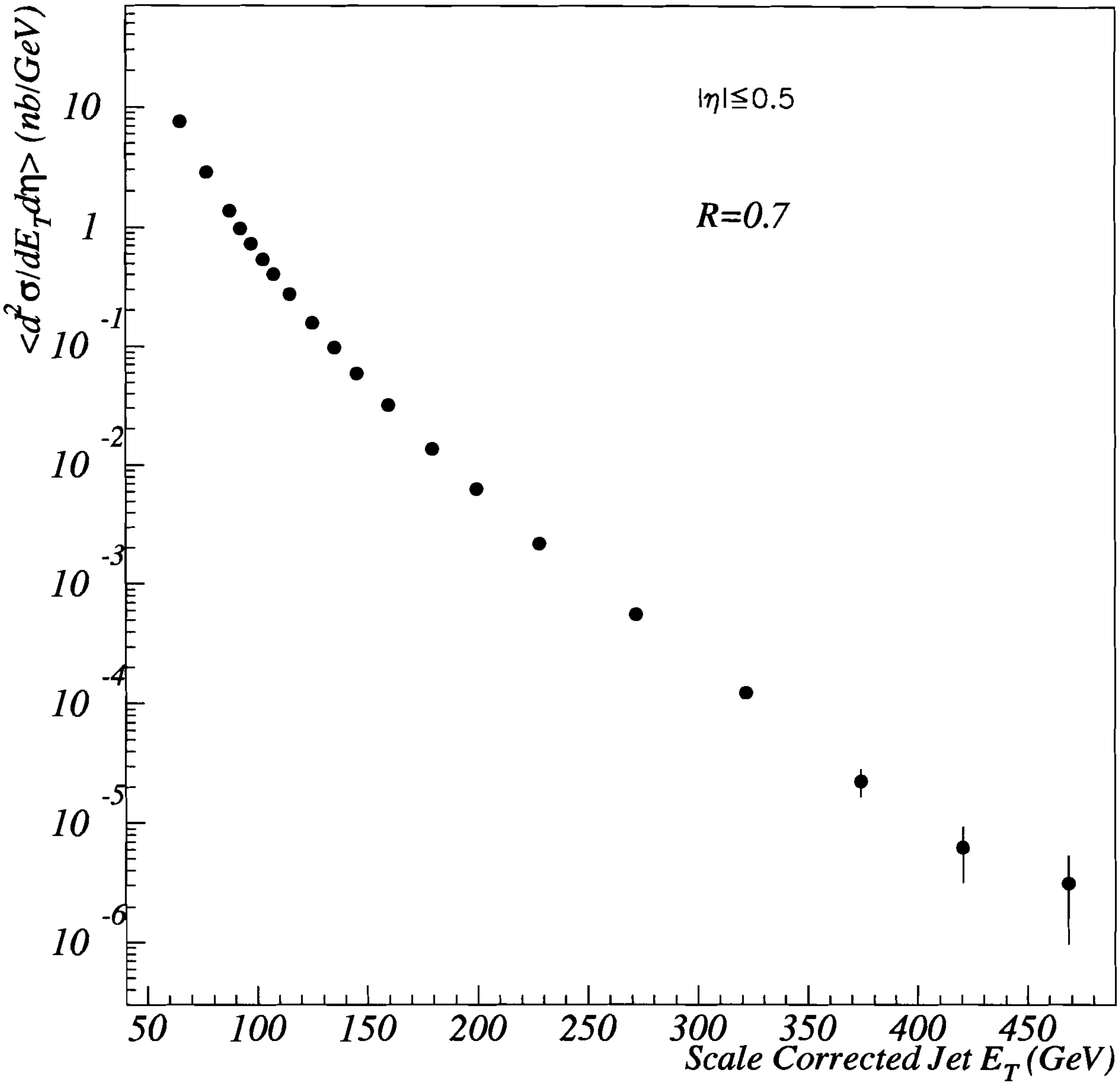

Figure 6.7: Observed Inclusive Jet cross sections in $|\eta| \leq 0.5$ for jet cone size of 0.7.

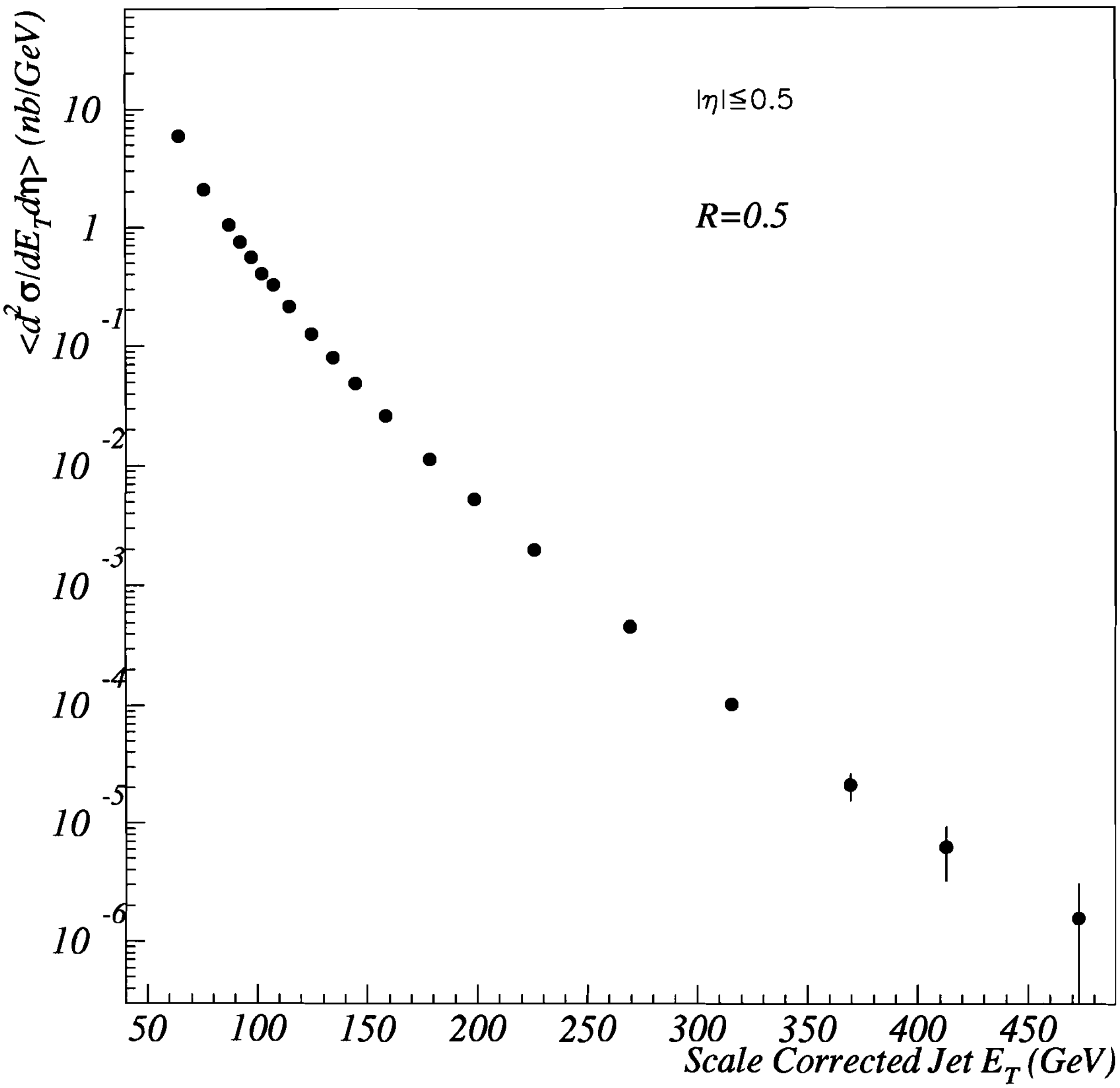

Figure 6.8: Observed Inclusive Jet cross sections in $|\eta| \leq 0.5$ for jet cone size of 0.5.

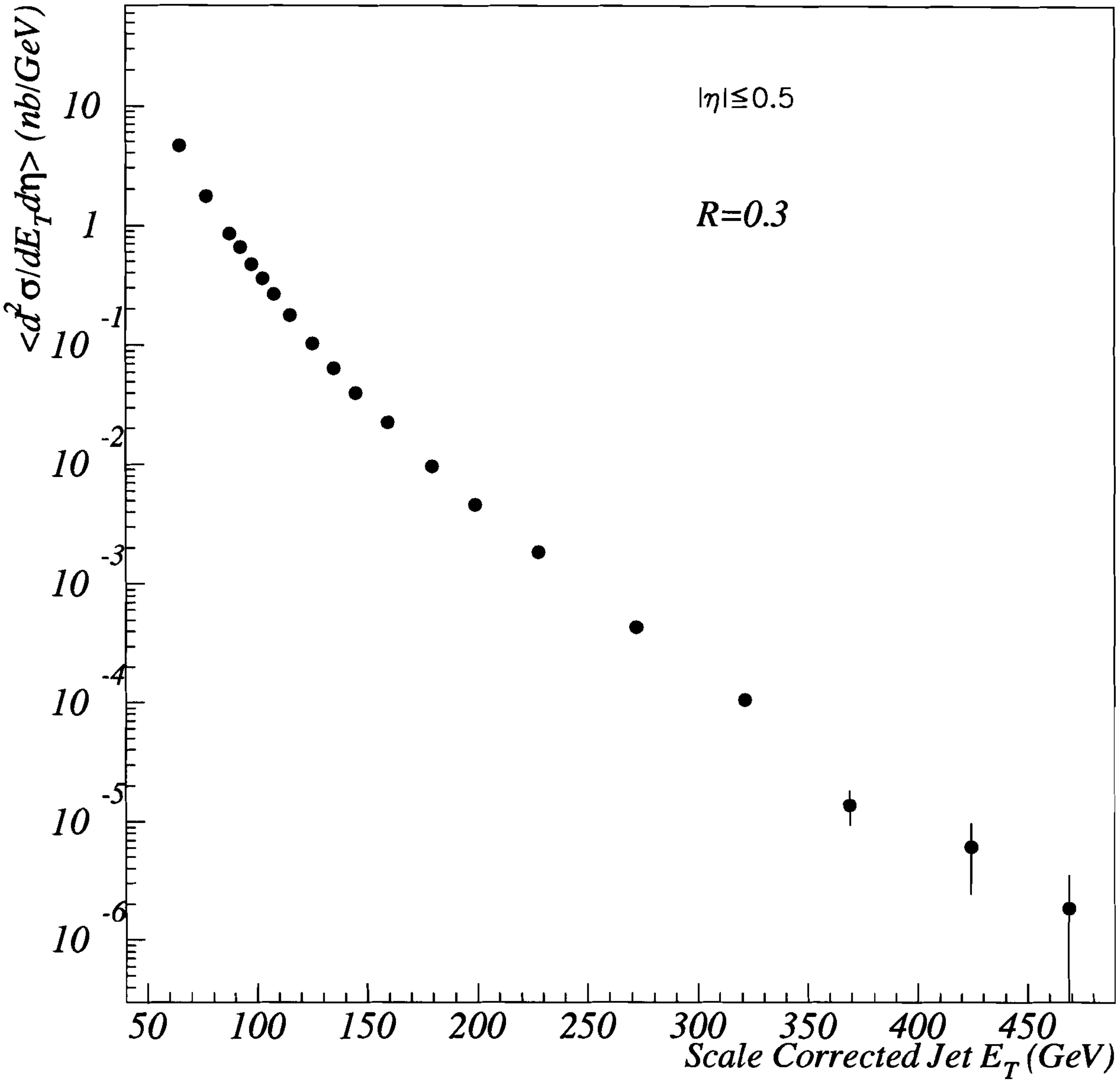

Figure 6.9: Observed Inclusive Jet cross sections in $|\eta| \leq 0.5$ for jet cone size of 0.3.

Chapter 7

Resolution Unsmearing of the Inclusive Jet Cross Section

7.1 Introduction

The finite calorimeter energy resolution smears the measured jet energy. As shown in Fig. 7.1, after passing through the detector, a monoenergetic beam of jets would be smeared with a width σ_E, centered at $E' < E$. The energy scale shifts the average response from E' back to E. However, jet distributions are still smeared due to the finite energy resolution. Also, η resolution smears the jet distribution. The inclusive jet cross section must be corrected for resolution effects before it can be compared to NLO QCD predictions.

The excellent energy resolution of the DØ electromagnetic calorimetry provides an opportunity to study jet resolution, σ_{E_T}, using photon - jet events. Fig. 7.2 shows the jet E_T distribution for γ - jet events with the photon in a very limited E_T range. Since the γ's were limited to 10 GeV intervals, most of the distribution variance is due to jet resolution. The distributions are well described by Gaussian curves.

Transverse energy smearing shifts jets from one bin in E_T to nearby bins. Due to the steeply falling nature of the inclusive jet cross section, more jets migrate from low

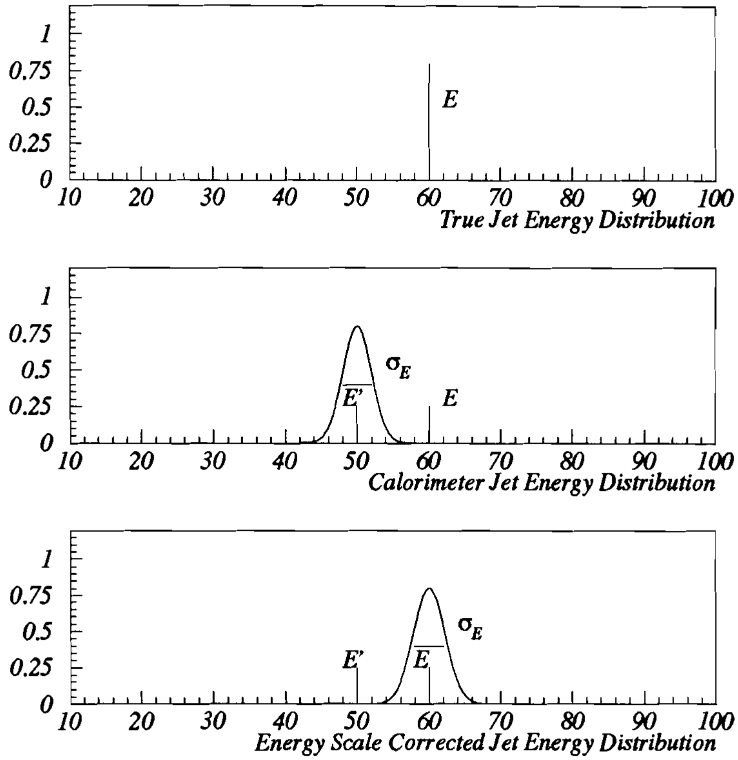

Figure 7.1: The calorimeter smears the energy distribution of a monoenergetic beam of jets of energy E with a width σ_E. The mean energy recorded is $E' < E$. The energy scale correction shifts the mean to E, but the distribution still remains smeared.

E_T bins to high E_T bins than from high E_T to low E_T. Thus, as shown in Fig. 7.3, the observed cross section, f, is higher than the true cross section, F. In this chapter, the unsmearing method developed to unsmear the inclusive jet cross section will be discussed. This requires the measurement of jet E_T resolution. Also discussed are the sources of error on the unsmearing procedure and the error on the final unsmeared cross section due to resolution unsmearing.

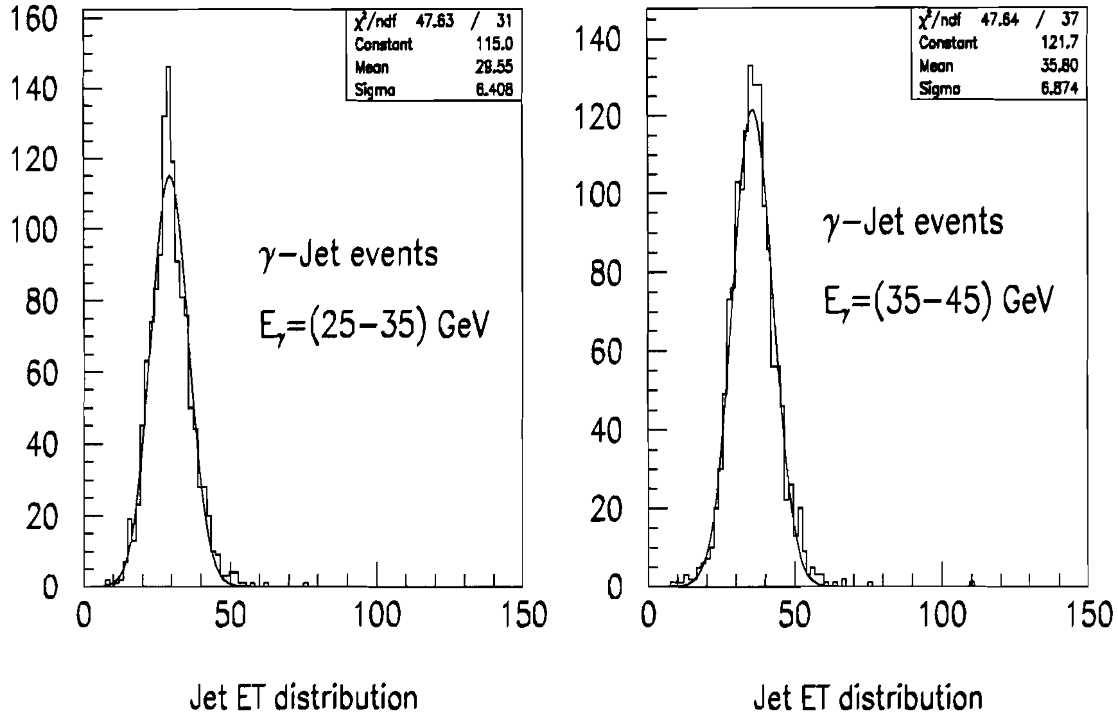

Figure 7.2: Jet resolution from γ - jet events.

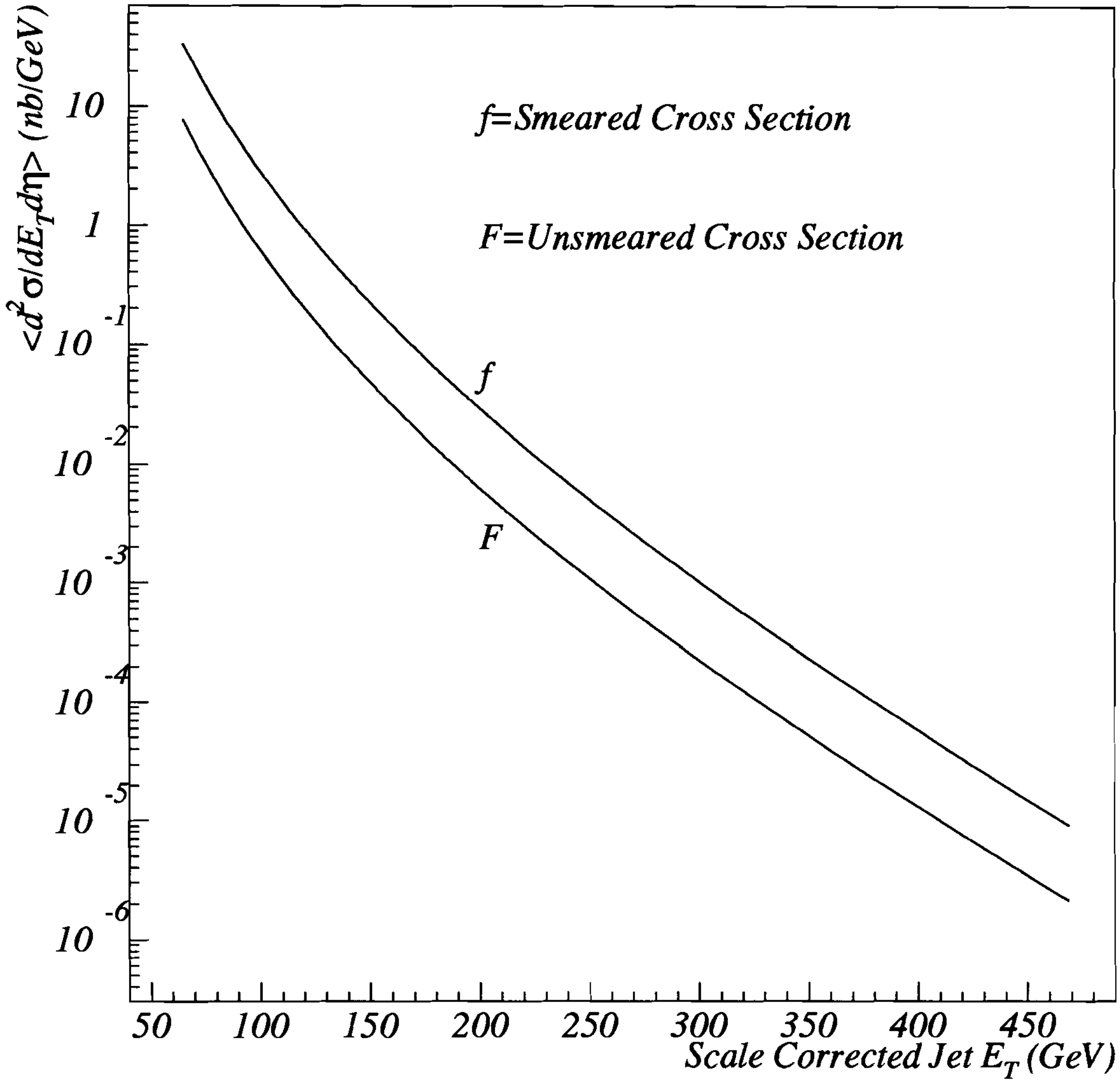

Figure 7.3: Effect of E_T smearing on Inclusive Jet cross section.

7.2 The Unsmearing Procedure

The smeared cross section f can be written as a convolution of the unsmeared cross section F and a smearing function G as [40, 52] :

$$f(E_T',\eta') = \int_{E_T}\int_{\eta} G(E_T' - E_T, \eta' - \eta)F(E_T', \eta')dE_T d\eta. \tag{7.1}$$

The top plot in Fig. 7.4 shows the jet η resolution as a function of particle jet E_T for different cone sizes as measured with a Monte Carlo jet sample (HERWIG). The bottom plot shows the ratio of a theoretical jet cross section smeared with the measured η resolution and the unsmeared jet cross section (JETRAD). The effect of η resolution on the inclusive jet cross section is negligible (1-2%) and can be neglected [7]. The double integral above can be approximated by a single integral, further the E_T smearing is Gaussian as shown in Fig. 7.2, thus the convolution becomes:

$$f(E_T') = \int_{E_T} \frac{1}{\sqrt{2\pi}\sigma_{E_T}} e^{-\frac{(E_T'-E_T)^2}{\sigma^2_{E_T}}} F(E_T)dE_T \tag{7.2}$$

The following procedure is used to unsmear the inclusive jet cross section: An Ansatz function which depends on jet E_T and four independent parameters is selected to describe the unsmeared or "true" jet cross section. The Ansatz must describe a variety of different shapes that can arise from different pdf's, μ scales and compositeness scales (λ_c) in theory. This function, $F(E_T, A, B, C, D)$, which we call the **hypothesis**, is given by:

$$F = (A/E_T^B)(1 + C(\frac{2}{\sqrt{s}})E_T)^D. \tag{7.3}$$

The hypothesis is smeared numerically with the smearing function $G(E_T', E_T)$, which is a Gaussian with a variance equal to the jet E_T resolution, according to the following formula:

$$f(E_T', A, B, C, D) = \int_{E_T} G(E_T', E_T)F(E_T, A, B, C, D)dE_T, \tag{7.4}$$

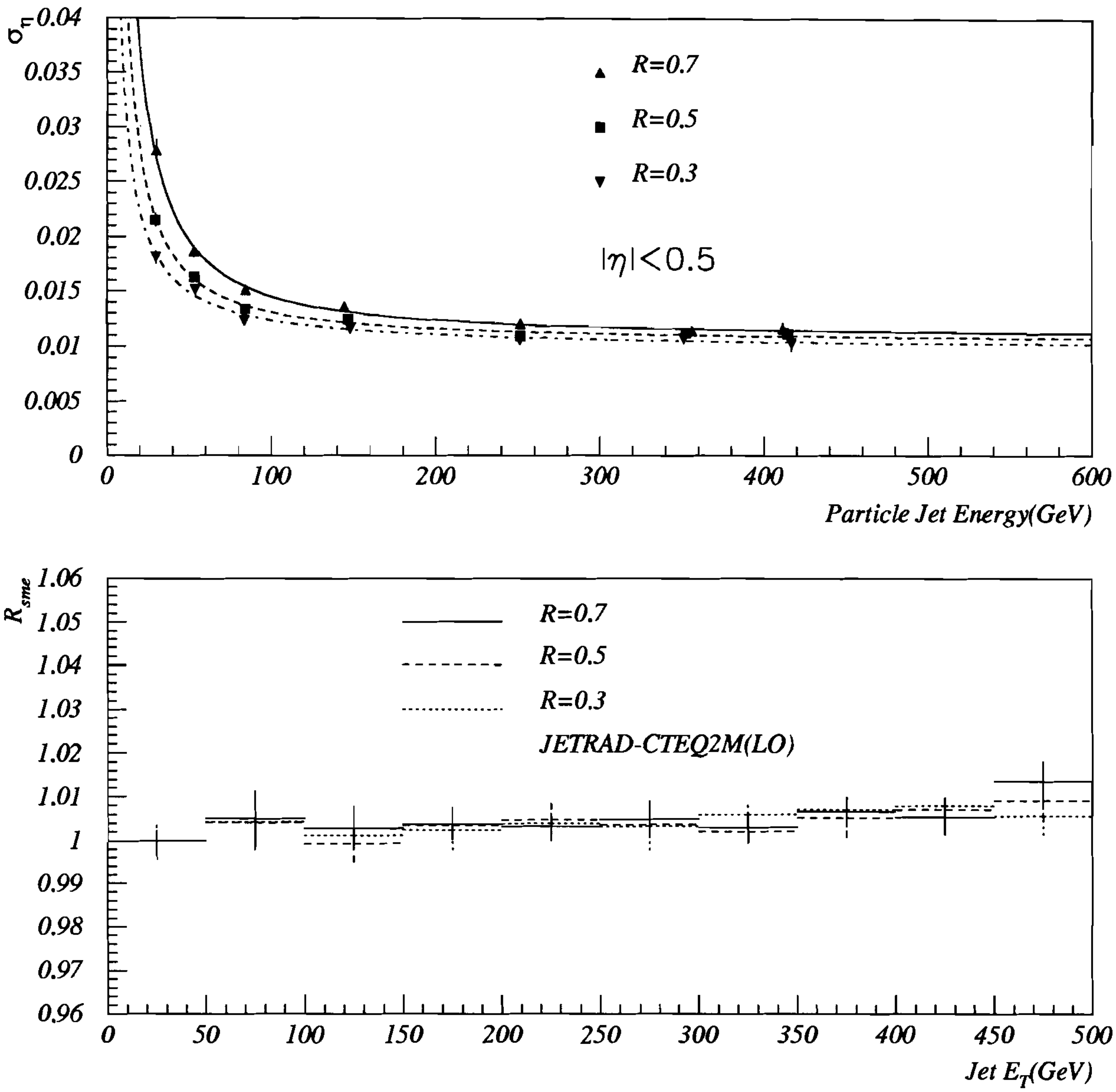

Figure 7.4: **Top** plot shows jet position resolution (η resolution) for 0.7, 0.5 & 0.3 cone jets obtained from HERWIG. **Bottom** plot shows the effect of η resolution on the inclusive jet cross section in central pseudorapidities, for 0.7, 0.5 & 0.3 cone jets. This is obtained from JETRAD.

The **smeared hypothesis** $f(E'_T, A, B, C, D)$ is then fitted to the observed inclusive jet cross section. The fit gives the four independent free parameters A, B, C, D. The parameters determine both the hypothesis and the smeared hypothesis. The inverse unsmearing correction applied to the observed cross section is given by the the following ratio:

$$R_{res} = \frac{f(E'_T, A, B, C, D)}{F(E_T, A, B, C, D)}. \tag{7.5}$$

7.3 Jet E_T Resolution

The fractional jet energy resolution σ_E/E can be parametrized as:

$$\frac{\sigma_E}{E} = \sqrt{\frac{N^2}{E^2} + \frac{S^2}{E} + C^2}, \tag{7.6}$$

where, the sampling term, $S/\sqrt{E}$, is dominated by the intrinsic energy resolution of the sampling calorimeter. The constant term, C^2, is due to detector imperfections and response nonlinearity. Uranium noise and underlying events contribute to the noise, N^2/E^2 term. The DØ detector has a fractional energy resolution of $15\%/\sqrt{E}$ for electrons and $50\%/\sqrt{E}$ for pions [30].

Since we measure the inclusive differential jet cross section as a function of jet E_T, we need to measure the fractional jet E_T resolution, σ_{E_T}/E_T as a function of jet E_T. The resolutions are a function of detector pseudorapidity, η_d, but we measure them in bins of physics η as the jet cross section is measured in bins of physics η. Also, apart from detector resolution, the effects of the fluctuation of the event z-vertex position must be folded into the resolutions used for data unsmearing. However, we should not include the contribution of the particles outside the particle jet cone to σ_{E_T}/E_T. This is because, the particle jet E_T is the true jet E_T in our QCD measurements. Data taken during the 1992-93 run is used to measure fractional jet E_T resolution.

The Dijet Balance Method

The determination of jet E_T resolution utilizes conservation of momentum in the transverse plane between the two leading jets in an event [53, 54]. In order to minimize the effects of additional low E_T jet contamination in the sample, the dijet events must be selected and handled very carefully. Problem runs were deleted from the sample. The following cuts are applied to select a clean dijet sample:

- The z-coordinate of the interaction vertex must be within 100 cm of the center of the detector.

- All the events are required to pass the R_{MTE} cut and all the jets are required to satisfy the standard jet cuts.

- The two leading jets must each have $E_T > 15$ GeV and must be back-to-back in ϕ within 5^0. If there are other jets in the event they must have $E_T < 8$ GeV (**dijet cut**).

- The two leading jets are required to be in the same η region so that resolutions are approximately equal.

The fractional jet E_T resolution is extracted from the asymmetry A, computed for each dijet event:

$$A = \frac{E_{T_1} - E_{T_2}}{E_{T_1} + E_{T_2}}, \tag{7.7}$$

where $E_{T_{1,2}}$ denotes the E_T of the leading two jets in the event. The asymmetry resolution may be written as:

$$(\sigma_A)^2 = \left(\left|\frac{\partial A}{\partial E_{T_1}}\right| \sigma_{E_{T_1}}\right)^2 + \left(\left|\frac{\partial A}{\partial E_{T_2}}\right| \sigma_{E_{T_2}}\right)^2 . \tag{7.8}$$

With both jets in the same η and $E_{T_1} \sim E_{T_2} \equiv E_T$:

$$\left(\frac{\sigma_{E_T}}{E_T}\right) = \sqrt{2}\sigma_A. \tag{7.9}$$

where, σ_A is the asymmetry resolution. Fig. 7.5 shows the asymmetry resolution at an average E_T of 110 GeV. The asymmetry distributions have been symmetrized by taking $E_{T_1} - E_{T_2}$ or $E_{T_2} - E_{T_1}$ in the numerator randomly for each event. Notice the data are well described by a Gaussian fit.

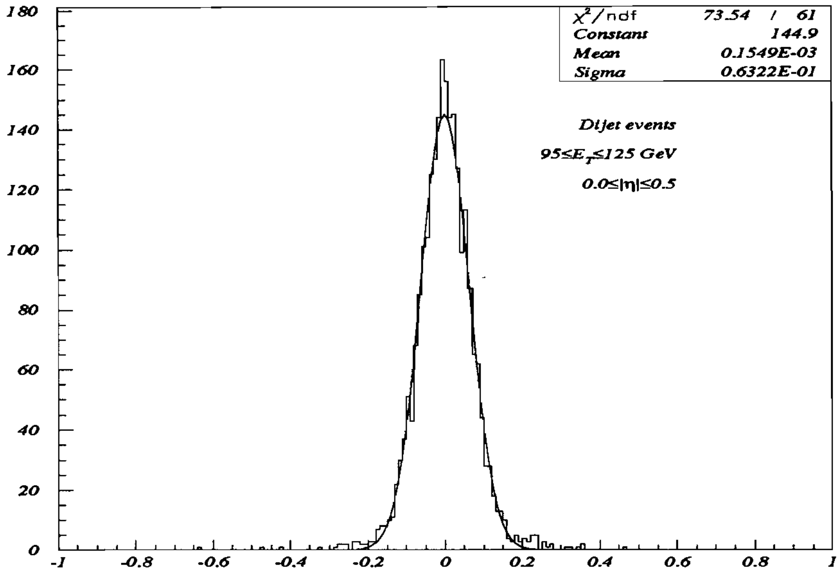

Figure 7.5: The asymmetry σ_A resolution for dijet events at an average E_T of 110 GeV in $|\eta| \leq 0.5$.

The resolutions as derived from asymmetry must be corrected for soft unreconstructed radiation and particle level fluctuations. These are discussed below.

Soft Radiation Correction

Although the back-to-back ϕ and dijet cuts were designed to select dijet events, the presence of unreconstructed extra jets and soft radiation can prevent the two leading jets from balancing in E_T in the transverse plane. Hence, the measured resolutions

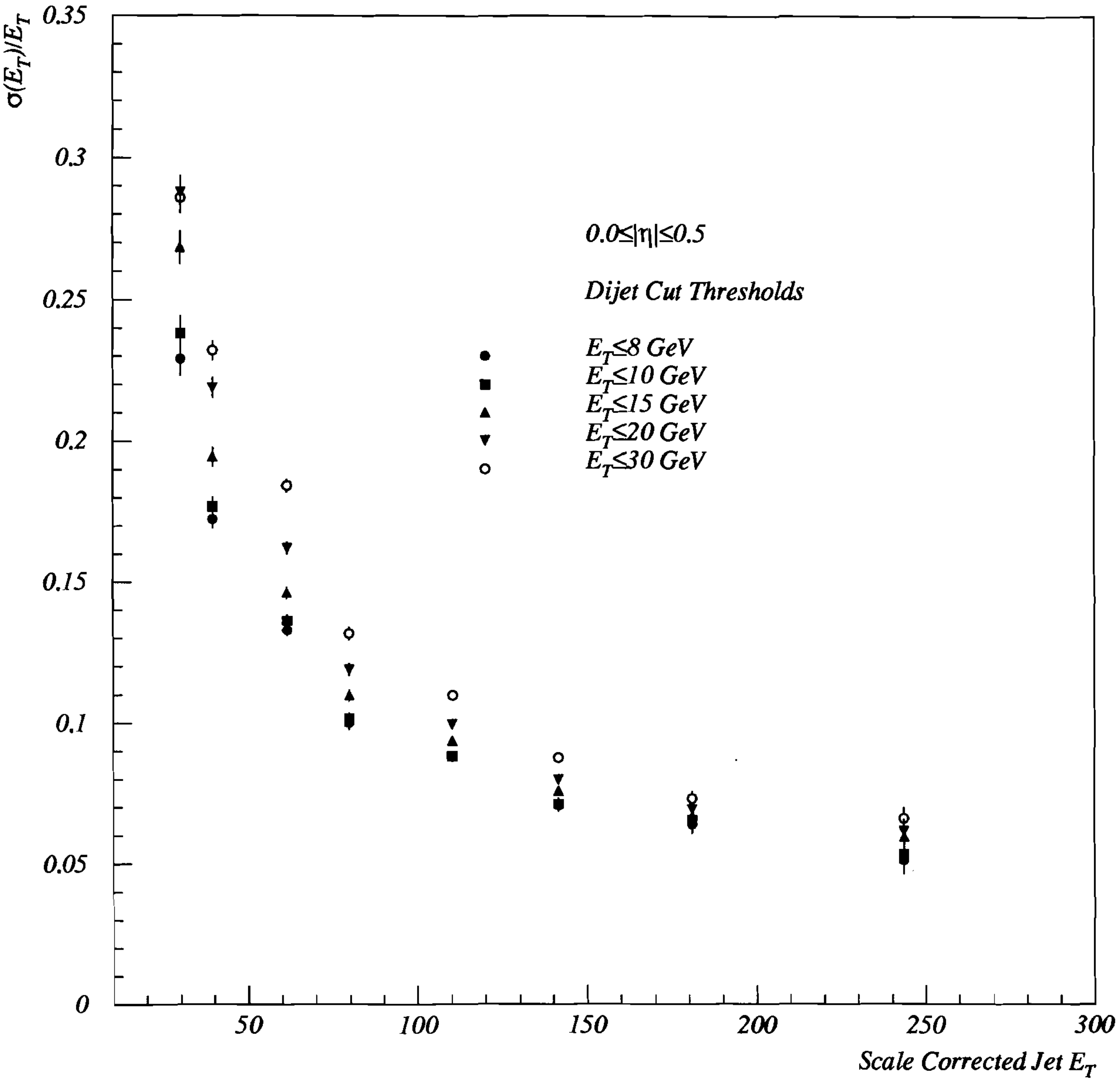

Figure 7.6: Fractional E_T resolution as a function of jet E_T for different dijet cut thresholds.

from dijet balance are overestimates of the true resolutions [54]. The bias introduced by the presence of extra jets and soft radiation is evaluated by applying following different dijet cuts to select a clean dijet sample: 8, 15, 15, 20 and 30 GeV. The resolutions for 0.7 cone jets in $|\eta| \leq 0.5$, measured from the samples selected by these dijet cuts are shown in Fig. 7.6. For each of the E_T bins, the ratio of resolutions defined as:

$$(\frac{\sigma_{E_T}}{E_T})^{Thr=\epsilon}/(\frac{\sigma_{E_T}}{E_T})^{Thr=8GeV} \tag{7.10}$$

is evaluated as a function of the cut threshold, ϵ. If we parametrize each ratio (for each bin in E_T) and extrapolate the fit to $\epsilon = 0$, we derive the resolution for a pure dijet sample. Hence, we fit a straight line and the extrapolation gives us:

$$K(E_T) = (\frac{\sigma_{E_T}}{E_T})^{Thr=0}/(\frac{\sigma_{E_T}}{E_T})^{Thr=8GeV} \tag{7.11}$$

from which we can calculate the unbiased fractional E_T resolution as:

$$(\frac{\sigma_{E_T}}{E_T}) = K \times (\frac{\sigma_{E_T}}{E_T})^{Thr=8GeV} \tag{7.12}$$

This procedure, repeated for each E_T bin provides the soft radiation correction as a function of jet E_T, which is larger at low E_T's. The following functional form is fitted to the soft radiation correction as a function of E_T:

$$K(E_T) = 1 - e^{(-a_0 - a_1 E_T)} \tag{7.13}$$

and the fit itself is used to calculate the unbiased resolutions. Fig. 7.7 shows the soft radiation correction for 1.0, 0.7, 0.5 and 0.3 cone jets as a function of jet E_T in $|\eta| \leq 0.5$. We do not use the fit error to calculate the error on $K(E_T)$. The point-to-point correlation on the ratio plots are large as each data point is derived from a data set which is subset of the previous data point. Also the assumption is made that the linear trend continues down to $\epsilon = 0$. The error on $(\frac{\sigma_{E_T}}{E_T})^{Thr=10GeV}/(\frac{\sigma_{E_T}}{E_T})^{Thr=8GeV}$ is taken as the error on $K(E_T)$. The values of a_0 and a_1 for different jet cone sizes are given in Table 7.1.

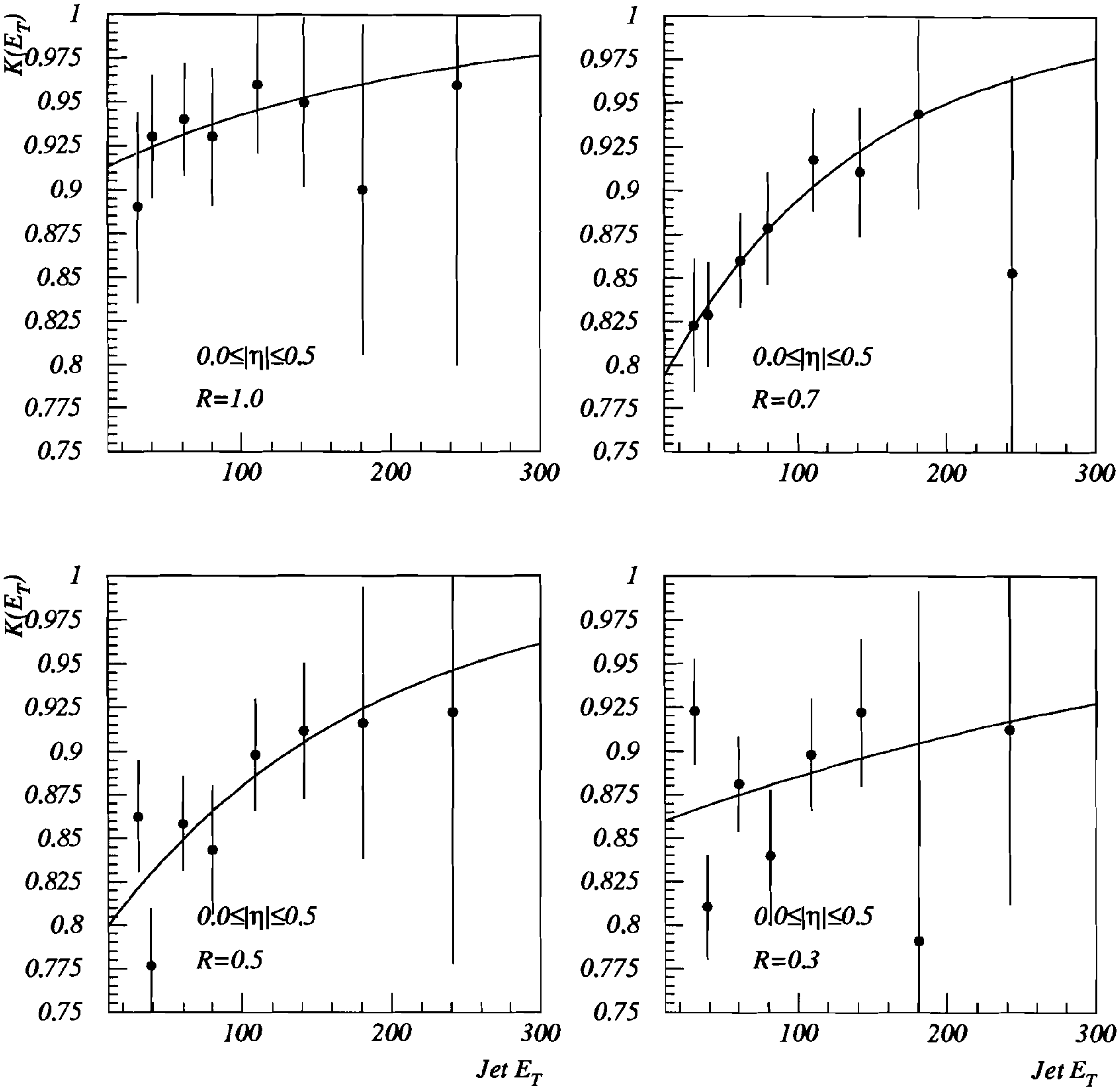

Figure 7.7: Soft radiation correction for different cone sizes in $|\eta| \leq 0.5$

Table 7.1: Soft radiation correction parameters for different cone sizes in $|\eta| \leq 0.5$.

Cone Size R	a_0	a_1
1.0	2.3968	0.45963E-02
0.7	1.5046	0.74758E-02
0.5	1.5499	0.56818E-02
0.3	1.9428	0.22501E-02

Particle Level Dijet Imbalance

The energy scale correction scales the jet energy to that of the parent particle jet incident upon the calorimeter. Once the energy scale correction is applied and the soft radiation bias has been removed, there still remains the effect of particles emitted outside the particle jet cone at particle level [54]. Because of these particles the jets in a dijet event at the particle level do not necessarily balance in E_T. This effect is convoluted with the detector resolution measured with the dijet balance method and must be removed.

The particle jet imbalance contribution, $(\frac{\sigma_{E_T}}{E_T}|^{pjet})_{asym}$, to the resolution can be estimated by applying the dijet balance method to particle jets in a Monte Carlo sample. The contribution obtained from a HERWIG sample in $|\eta| \leq 0.5$ for 0.7 cone jets, is shown in Fig. 7.8 along with the fractional E_T resolution from the data after soft radiation bias correction. The correct fractional E_T resolution is obtained from the following expression:

$$(\frac{\sigma_{E_T}}{E_T})^2 = (\frac{\sigma_{E_T}}{E_T})^2_{asym} - (\frac{\sigma_{E_T}}{E_T}|^{pjet})^2_{asym}, \tag{7.14}$$

the suffix *asym* stands for $K(E_T)$ corrected resolution.

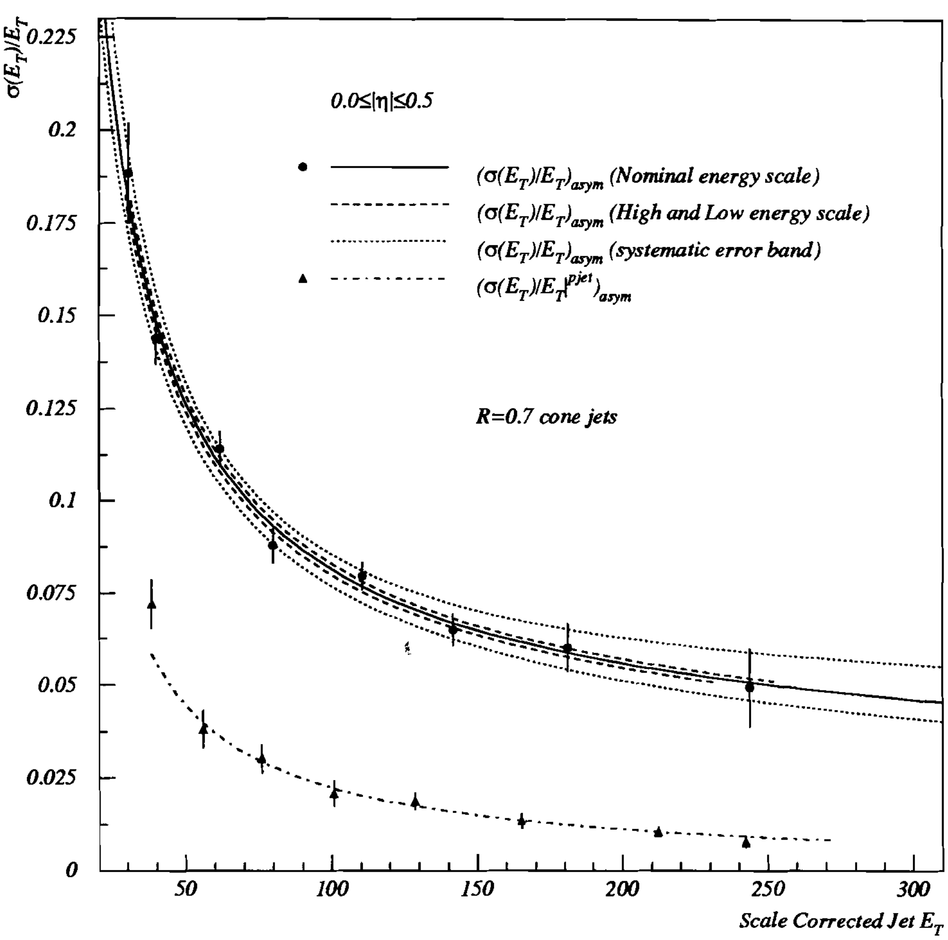

Figure 7.8: $(\frac{\sigma_{E_T}}{E_T}|^{pjet})_{asym}$ given by black triangles and $(\frac{\sigma_{E_T}}{E_T})_{asym}$ given by black dots, as a function jet E_T. The solid line is a fit to the nominal data points, while the dashed lines are fits to the data points from the high and low error on the energy scale correction. The dotted lines show the systematic error on the measured resolution. The dashed dotted line is a fit to the particle imbalance contribution.

Monte Carlo Consistency Checks

Using HERWIG Monte Carlo events a number of checks have been performed on the method and approximations that go into the resolution measurements [54]. The HERWIG sample provides jets both at the particle level and after full detector simulation (calorimeter level). Fractional jet E_T resolutions can be measured from calorimeter level jets in the same way as in data, by applying E_T balancing in dijet events followed by the soft radiation correction. This is equivalent to the dijet asymmetry resolution obtained from data and is denoted by $(\sigma(E_T)/E_T)_{Asym}$. One of the checks was to find out if the dijet balance method applied on calorimeter level jets give the same resolutions as that given by the direct comparison of calorimeter jet E_T to particle jet E_T, denoted by $\sigma(E_T^{cal}/E_T^{pjet}) \equiv (\sigma(E_T)/E_T)_{True}$. This is the true jet resolution as it contains only the effect of detector resolution. E_T balancing can also be applied in dijet events at particle level followed by the soft radiation correction. This gives the effect of particles outside the jet defining cone at particle level on the E_T balancing method, which is denoted by $(\sigma(E_T)/E_T|^{pjet})_{Asym}$. Fig. 7.9 shows all these three quantities and as can be seen, $(\sigma(E_T)/E_T)_{Asym}$ does not agree with $(\sigma(E_T)/E_T)_{True}$. However, as shown in Fig. 7.10, if the true jet resolution is added in quadrature with $(\sigma(E_T)/E_T|^{pjet})_{Asym}$ then it agrees within 1% with the dijet asymmetry resolution. This proves that the effect of particles outside the jet defining cone at particle level (particle imbalance effect) must be subtracted in quadrature from the measured jet resolution before it is used to unsmear the measured jet E_T distributions. The error on the resolution from the method is of the order of 1%.

The dijet balance method yields resolution as a function of the energy scale corrected jet E_T, but more fundamental is the resolution as a function of the particle jet E_T. Fig. 7.11 compares the dijet asymmetry resolution from HERWIG events binned in terms of energy scale corrected jet E_T with the dijet asymmetry resolution binned in terms of particle jet E_T. The error induced due to the use of scale corrected jet E_T rather than particle jet E_T is negligible. Although all the consistency checks are shown with 0.7 jets, they apply equally to all the jet cone sizes.

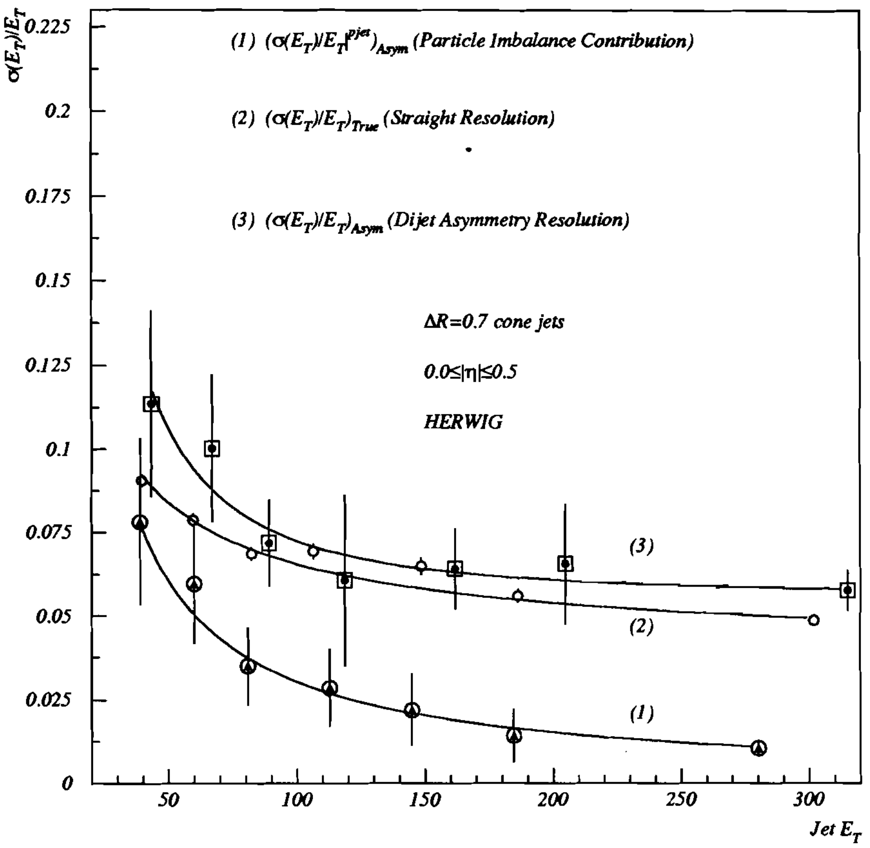

Figure 7.9: Monte Carlo consistency check with HERWIG events. $(\frac{\sigma_{E_T}}{E_T}|^{pjet})_{asym}$, $\sigma(\frac{E_T^{cal}}{E_T^{pjet}})$ and $(\frac{\sigma_{E_T}}{E_T})_{asym}$ as a function jet E_T.

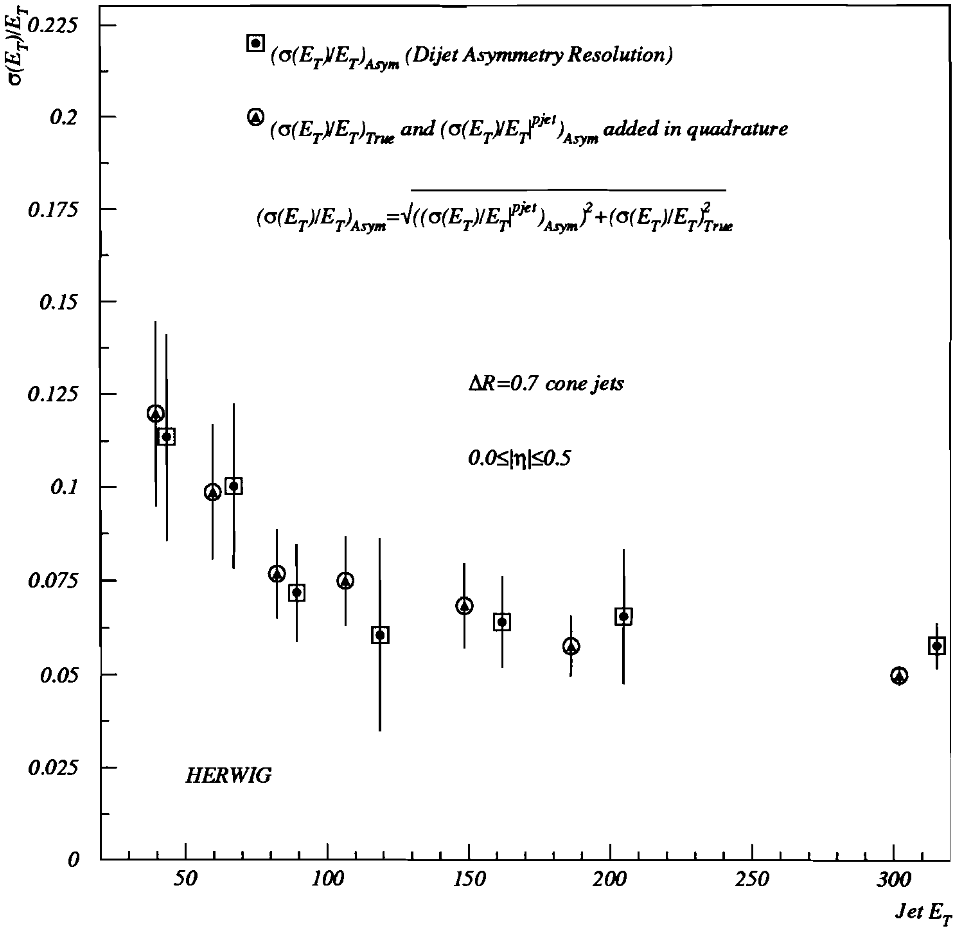

Figure 7.10: Monte Carlo consistency check with HERWIG events. $(\frac{\sigma_{E_T}}{E_T}|^{pjet})_{asym}$ and $\sigma(\frac{E_T^{cal}}{E_T^{pjet}})$ added in quadrature and compared to $(\frac{\sigma_{E_T}}{E_T})_{asym}$ as a function jet E_T.

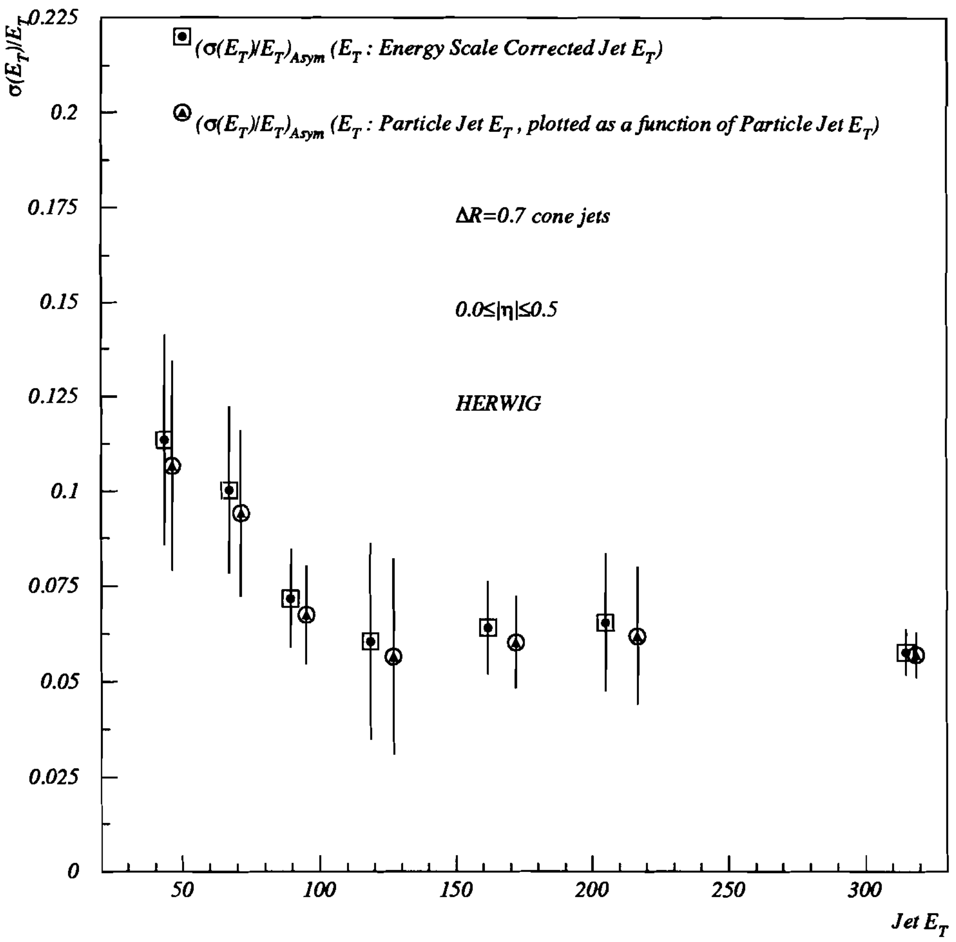

Figure 7.11: Monte Carlo consistency check with HERWIG events. Dijet asymmetry resolution binned in terms of scale corrected jet E_T compared to dijet asymmetry resolution binned in terms of particle jet E_T.

Results

The fractional jet E_T resolution is parametrized as:

$$\left(\frac{\sigma_{E_T}}{E_T}\right)^2 = \left(\frac{N}{E_T}\right)^2 + \left(\frac{S}{\sqrt{E_T}}\right)^2 + (C)^2. \tag{7.15}$$

The resolution parameters for the different cone sizes ($R = 1.0$, 0.7, 0.5, 0.3) are given in Table 7.2 [54].

Table 7.2: Jet E_T resolution fit parameters for different cone sizes in $|\eta| \leq 0.5$.

Jet Cone Size	Noise Term (N)	Sampling Term (S)	Constant Term (C)
1.0	3.89	0.66	0.04
0.7	3.96	0.55	0.036
0.5	5.13	0.38	0.045
0.3	6.47	0.66	0.035

Figs. 7.12 and 7.13, show the fractional jet E_T resolution obtained from collider data for $|\eta| \leq 0.5$ and 1.0, 0.7, 0.5 and 0.3 cones jets. These resolutions are corrected for soft radiation bias and the effect of particles outside the jet cone at the particle level. Also, plotted are resolutions obtained from HERWIG Monte Carlo. As can be seen from the plots, data and Monte Carlo are in agreement above 70 GeV. The data and Monte Carlo disagree below 70 GeV. This is due to the lack of multiple interaction and uranium noise in the sample. More complete Monte Carlo studies underway confirm this. Above 50 GeV these disagreements cause $< 5\%$ change in the inclusive jet cross section.

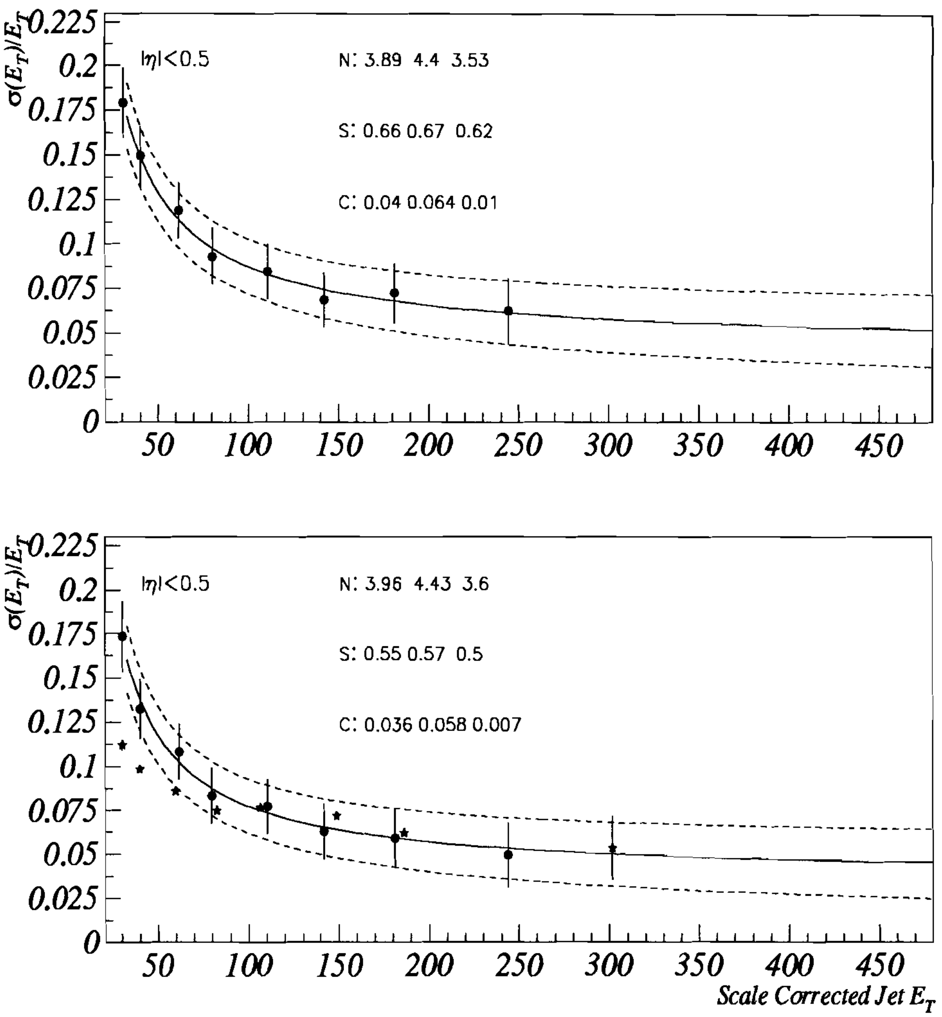

Figure 7.12: Fractional Jet E_T resolution for $|\eta| \leq 0.5$. **Cone Size R=1.0 (top) & Cone Size R=0.7 (bottom).** The dots (solid line) are the nominal data resolution, and the dashed lines give the error on the resolution measurement. The numbers from left to right are the fit parameters for nominal, upper & lower resolutions. The stars show the Monte Carlo resolution points. The last Monte Carlo point is included in the fit.

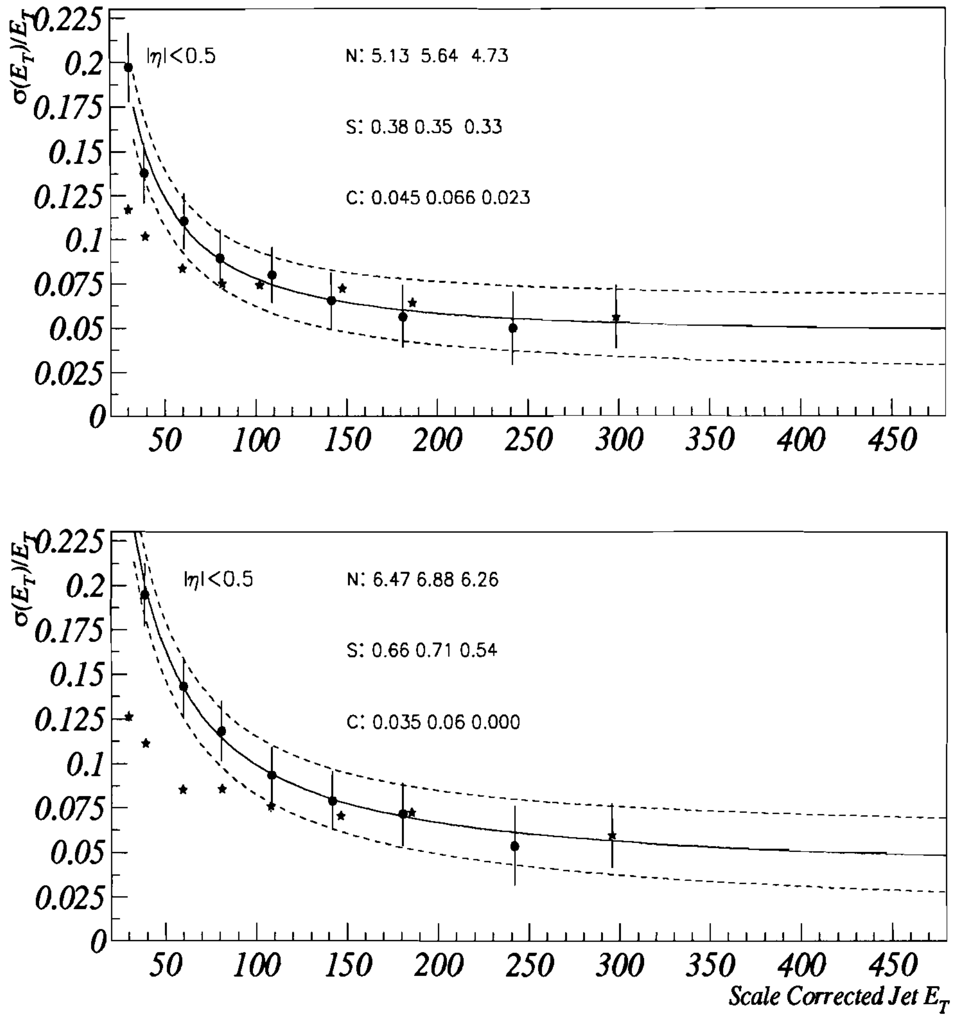

Figure 7.13: Fractional Jet E_T resolution for $|\eta| \leq 0.5$. **Cone Size R=0.5 (top) & Cone Size R=0.3 (bottom).** The dots (solid line) are the nominal data resolution, and the dashed lines give the error on the resolution measurement. The numbers from left to right are the fit parameters for nominal, upper & lower resolutions. The stars show the Monte Carlo resolution points. The last Monte Carlo point is included in the fit.

7.4 Unsmearing Results and Errors

The fit parameters A, B, C and D to the collider data for the four different cone sizes (R = 1.0, 0.7, 0.5, 0.3) are given in Table 7.3 [7]. Fig. 7.14 shows the unsmeared data cross section along with the hypothesis F.

Table 7.3: Parametrization of the central inclusive jet cross section, $F(E_T, A, B, C, D)$, as a function of energy scale corrected jet E_T.

R	η_d	lnA	B	C	D
1.0	0-0.5	24.25	5.1	-0.96	8.14
0.7	0-0.5	22.08	4.56	-0.36	32.27
0.5	0-0.5	20.31	4.17	-0.25	56.58
0.3	0-0.5	20.32	4.28	-0.46	24.78

The unsmearing process contributes to the systematic error of the inclusive jet cross section through [7]:

- the error on jet E_T resolution;
- the functional form chosen for the unsmearing procedure; and
- the dependence of the unsmearing process on statistical fluctuations of the data.

These errors have been estimated with a Monte Carlo simulation. Inclusive jet cross sections are generated with JETRAD at LO using the CTEQ2M parton distribution function. The cross sections are binned in E_T identically to the data. This study is also described in references [40, 52]. This simulation is done for all the cone sizes used in this analysis, R = 1.0, 0.7, 0.5, 0.3. The procedure used to obtain the error is as follows:

- The cross sections obtained from JETRAD are taken as the true inclusive jet cross section and are named **theory**.

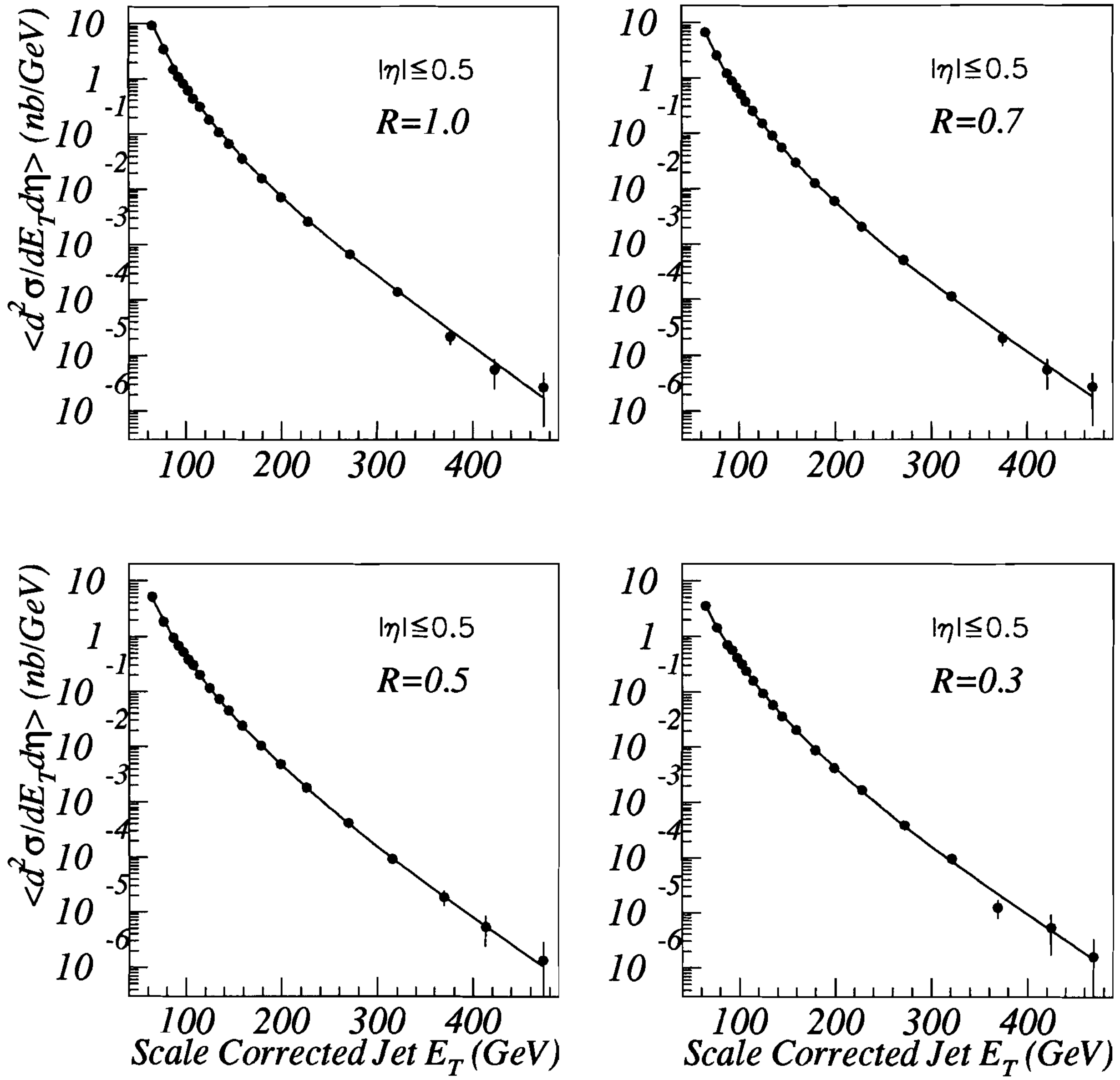

Figure 7.14: The hypothesis, $F(E_T', A, B, C, D)$, as fitted to the unsmeared data cross section for different cone sizes in central pseudorapidities.

- The true cross sections (theory) are smeared with the measured jet E_T resolution parameters given in Table 7.3. This is done by smearing each generated jet by the measured resolution parameters.

- Realistic statistical errors (E_{st}) are included into the smeared theory according to:

$$E_{st} = \frac{E_d}{C_d} C_{st}, \tag{7.16}$$

where E_d, C_d are, respectively, the statistical error and cross section of the real collider data and C_{st} is smeared theory cross section. Now the smeared theory points are called **simulated data** as they play the role of data. The statistical fluctuations are included in the simulated data by allowing the data points to fluctuate with a gaussian probability around the mean. The variance of the gaussian distribution are the realistic errors associated with the simulated data. Ten different sets of data are generated using this technique.

- The unsmearing procedure is applied to the simulated data in the same way as it was applied to real collider data and the smearing correction is obtained as:

$$R_{res}^{uns} = \frac{f(E_T^{'})}{F(E_T)}. \tag{7.17}$$

Once R_{res}^{uns} is obtained, it can be compared to:

$$R_{res}^{true} = \frac{data(simulated)}{theory}. \tag{7.18}$$

The difference between R^{true}_{res} and R^{uns}_{res} gives the systematic error associated with choice of the fit function and the fitting procedure, and the RMS of the ten sets of R^{uns}_{res} from the simulated data gives the error associated with the statistical fluctuation of the data.

Figs. 7.15, 7.16, 7.17 and 7.18 show the results of this simulation for $R = 1.0$, 0.7, 0.5 and 0.3 cone sizes, respectively in $|\eta| \leq 0.5$. The top plots show the difference between R^{true}_{res} and R^{uns}_{res} and the bottom plots show the change in the smearing correction due to statistical fluctuation in data. The change in the smearing correction due to choice of the fit function and fitting procedure is of the order of $0 - 2\%$ in the E_T range used in this analysis. The error due to statistical fluctuations is less than 0.5%.

The error on the jet E_T resolution also contributes to the cross section error. This error is measured by unsmearing the nominal data points with the upper and lower error bands in the jet E_T resolution. The top plots in Figs. 7.19, 7.20, 7.21 and 7.22 show the nominal unsmearing corrections for $R = 1.0$, 0.7, 0.5 and 0.3 inclusive cross sections, respectively, along with the (Nominal $+ 1\sigma$) and (Nominal - 1σ) bands on the correction (coming from upper and lower error bands of jet E_T resolution). For 1.0 cone jets the error is 8% at 35 GeV, 3.5% at 100 GeV and 9% at 400 GeV. For 0.7 cone jets the error is 7%, 2.5%, and 7% at 35, 100 and 400 GeVs. For 0.5 (0.3) cone the errors are 7% (7%), 2.5% (3%), and 10% (10%).

7.5 Conclusion

The unsmearing correction, $1/R_{res}$ given by Equation 7.5 is obtained by the method discussed above and the associated errors are also evaluated. As can be seen from the plots, the effect of this correction is to lower the observed jet cross section at a fixed E_T. Table 7.4 summarizes the size of this correction for all four jet cone sizes in $|\eta| \leq 0.5$. This correction can now be applied directly to the inclusive jet cross section obtained after event and jet selection and energy scale correction, to take out the effects of detector resolution in the following way:

$$\langle\frac{d^2\sigma}{dE_T d\eta}\rangle = \langle\frac{d^2\sigma}{dE_T d\eta}\rangle_{observed} \times \frac{1}{R_{res}(= f/F)}. \tag{7.19}$$

Once this correction is applied to the jet cross section, all the detector related effects are effectively removed, and the measured cross section can now be compared to NLO QCD predictions. In the next chapter, comparison of the measured cross section to theoretical predictions is discussed.

Table 7.4: Unsmearing correction for different cone sizes (R).

R=1.0		*R=0.7*		*R=0.5*		*R=0.3*	
E_T (GeV)	R_{res}	E_T (GeV)	R_{res}	E_T (GeV)	R_{res}	E_T (GeV)	R_{res}
87.42	13.4%	87.42	10.6%	87.37	10.2%	87.44	17.9%
92.43	12.7%	92.41	10.2%	92.38	9.6%	92.41	16.7%
97.44	12.2%	97.44	9.8%	97.43	9.2%	97.46	15.7%
102.43	11.7%	102.47	9.4%	102.42	8.8%	102.47	14.9%
107.43	11.2%	107.43	9.2%	107.48	8.4%	107.42	14.2%
114.73	10.7%	114.76	8.8%	114.62	8.1%	114.74	13.3%
124.83	10.1%	124.82	8.5%	124.65	7.6%	124.78	12.3%
134.82	9.7%	134.81	8.3%	134.60	7.4%	134.77	11.6%
144.81	9.4%	144.85	8.1%	144.66	7.2%	144.83	11.1%
159.27	9.1%	159.29	8.0%	158.69	7.0%	159.35	10.5%
179.33	8.8%	179.28	7.9%	178.48	7.0%	179.41	9.9%
199.41	8.7%	199.51	8.1%	198.72	7.1%	199.29	9.7%
227.59	8.8%	227.87	8.4%	225.76	7.4%	227.76	9.6%
271.55	9.4%	271.81	9.2%	269.65	8.2%	272.26	9.8%
321.28	10.7%	321.76	10.4%	315.83	9.4%	321.64	10.6%
376.02	12.8%	374.06	12.2%	369.69	11.2%	369.25	11.7%
422.85	15.5%	420.59	14.1%	413.10	13.0%	424.52	13.4%
473.69	19.5%	468.62	16.4%	473.08	15.8%	468.89	15.1%

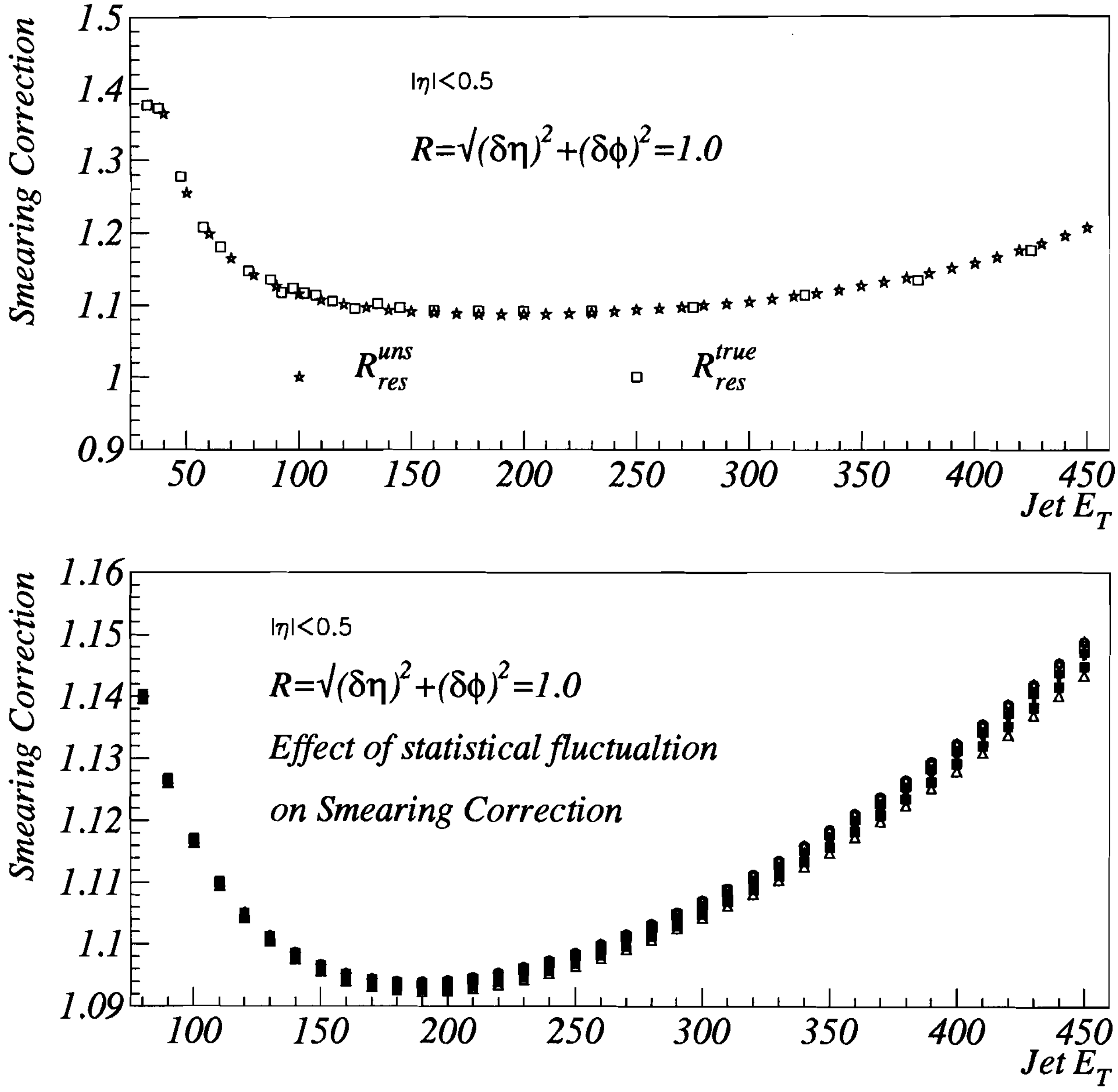

Figure 7.15: Error on unsmearing correction due to fit function (**top**) and statistical fluctuation of the data (**bottom**), 1.0 cone jets.

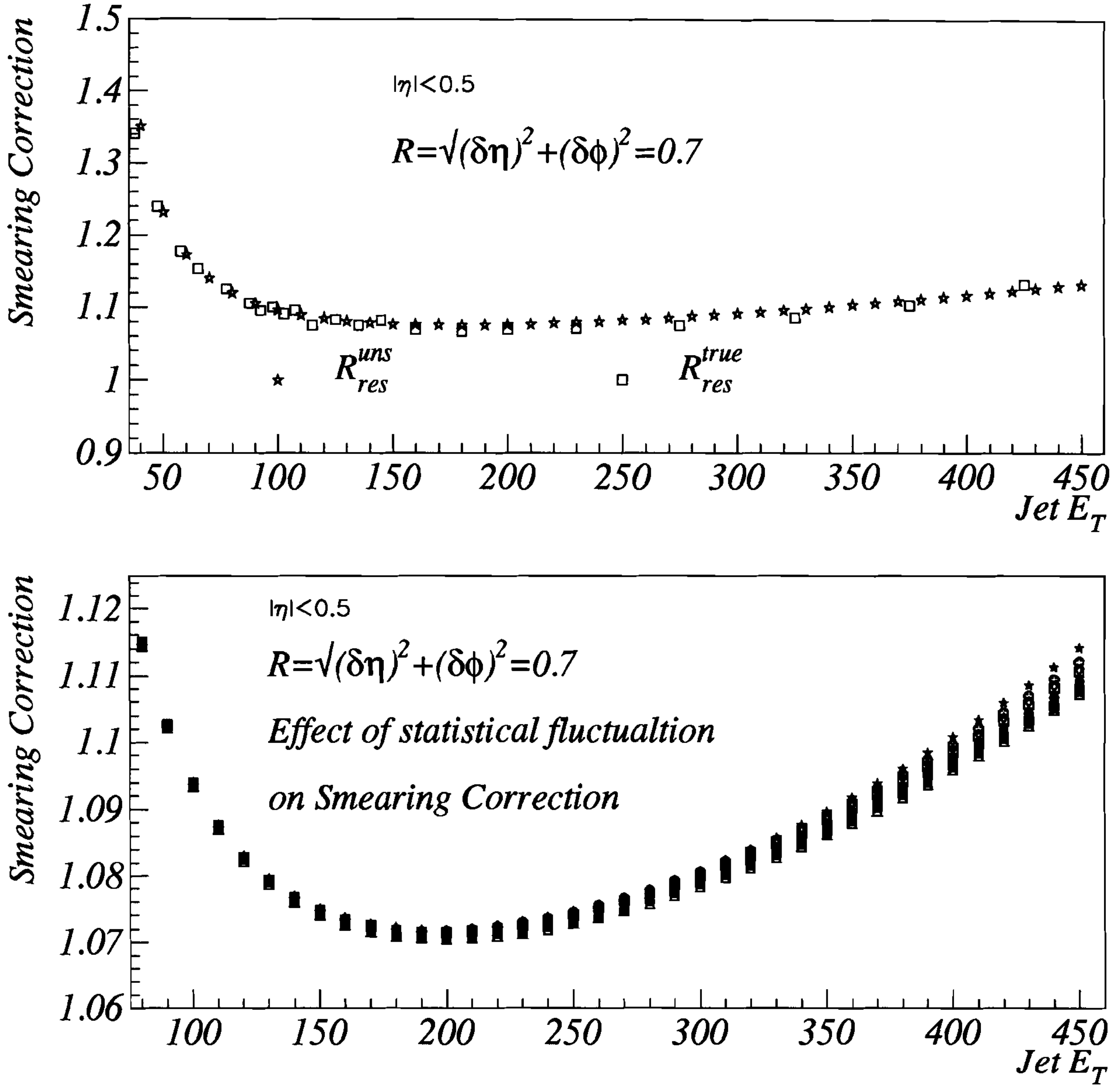

Figure 7.16: Error on unsmearing correction due to fit function (**top**) and statistical fluctuation of the data (**bottom**), 0.7 cone jets.

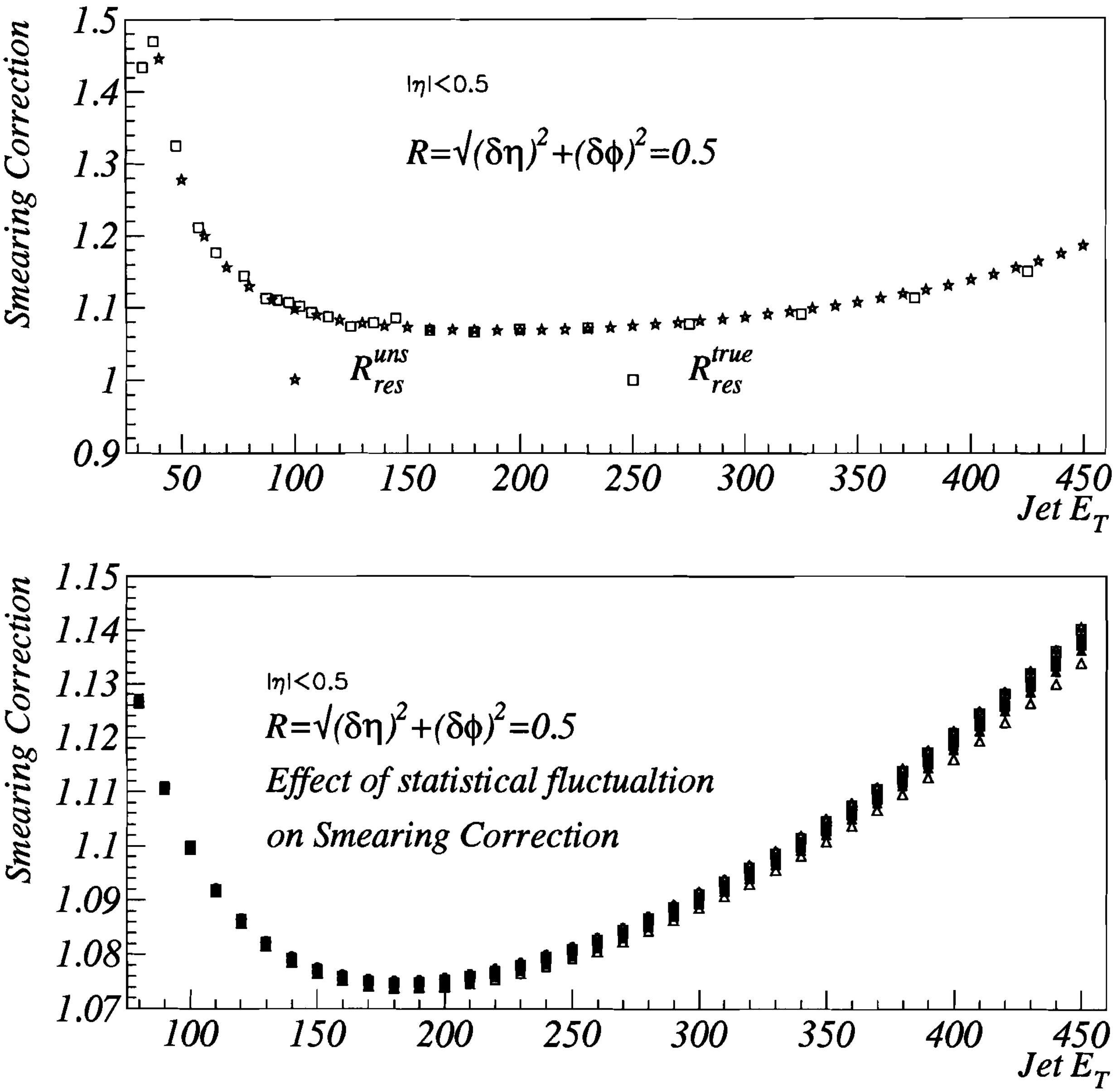

Figure 7.17: Error on unsmearing correction due to fit function (**top**) and statistical fluctuation of the data (**bottom**), 0.5 cone jets.

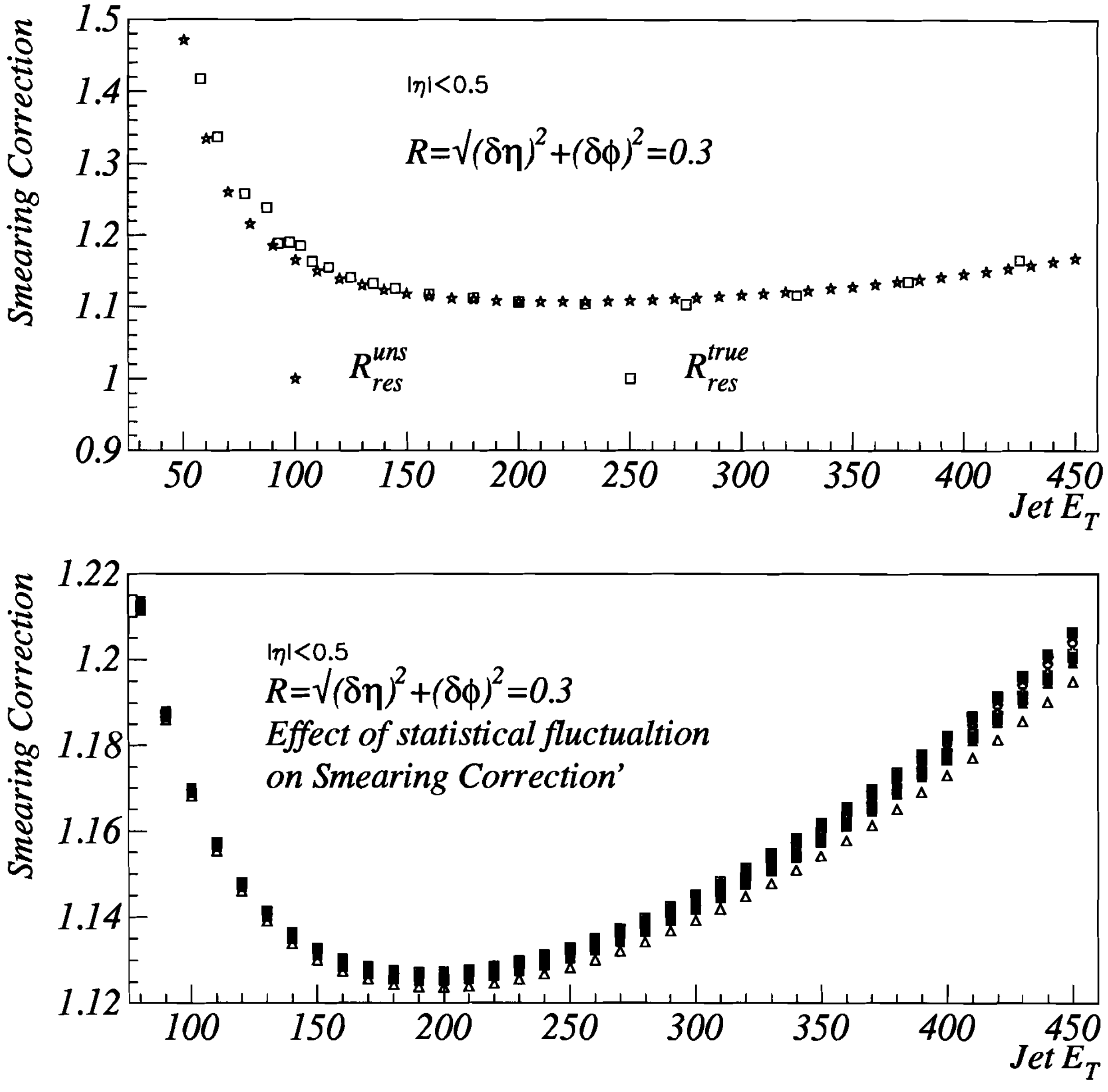

Figure 7.18: Error on unsmearing correction due to fit function (top) and statistical fluctuation of the data (bottom), 0.3 cone jets.

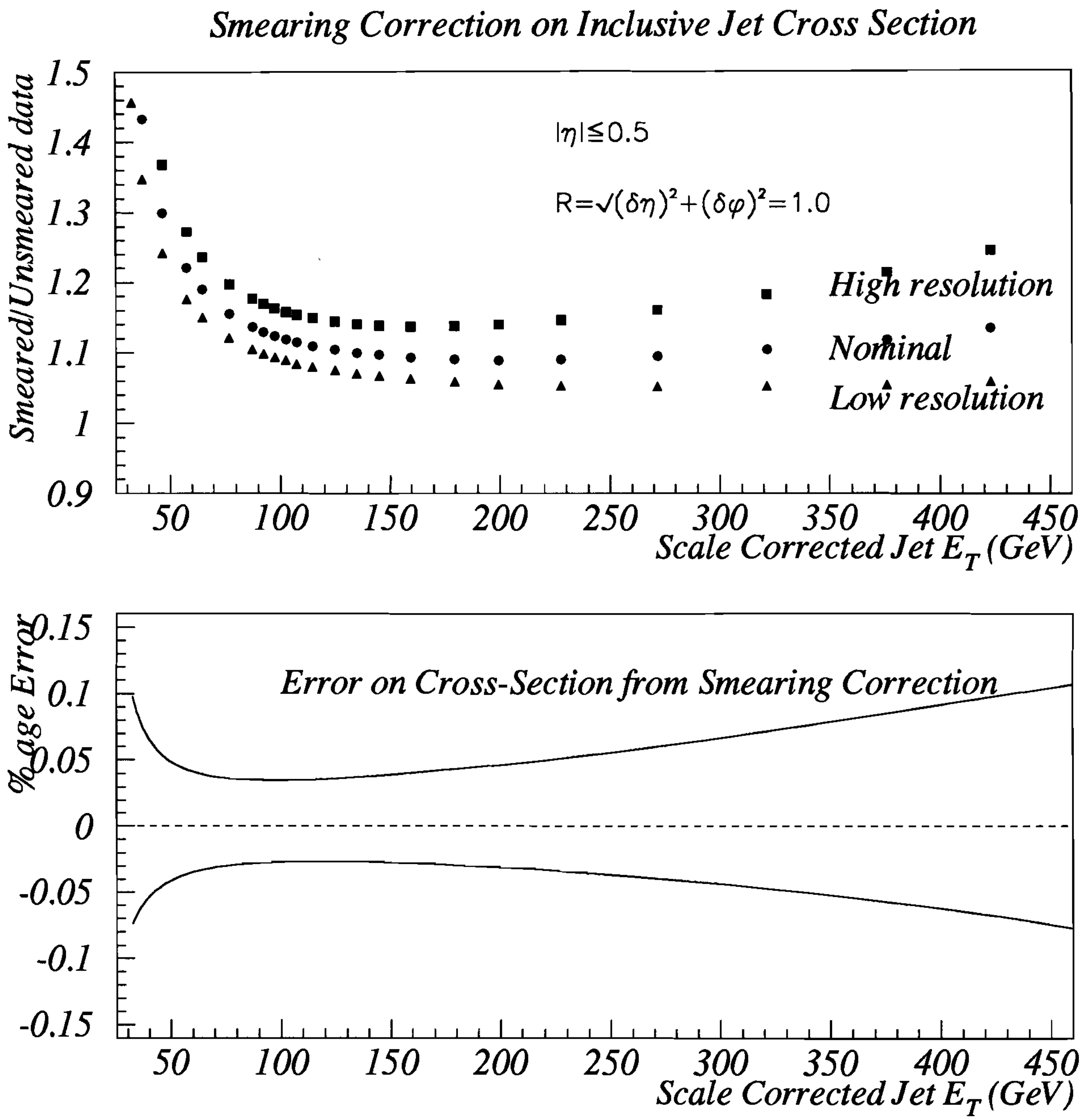

Figure 7.19: Unsmearing correction that is applied to the inclusive jet cross section for 1.0 cone jets (**top**). The unsmearing error due to error on E_T resolution is shown in the **bottom** plot.

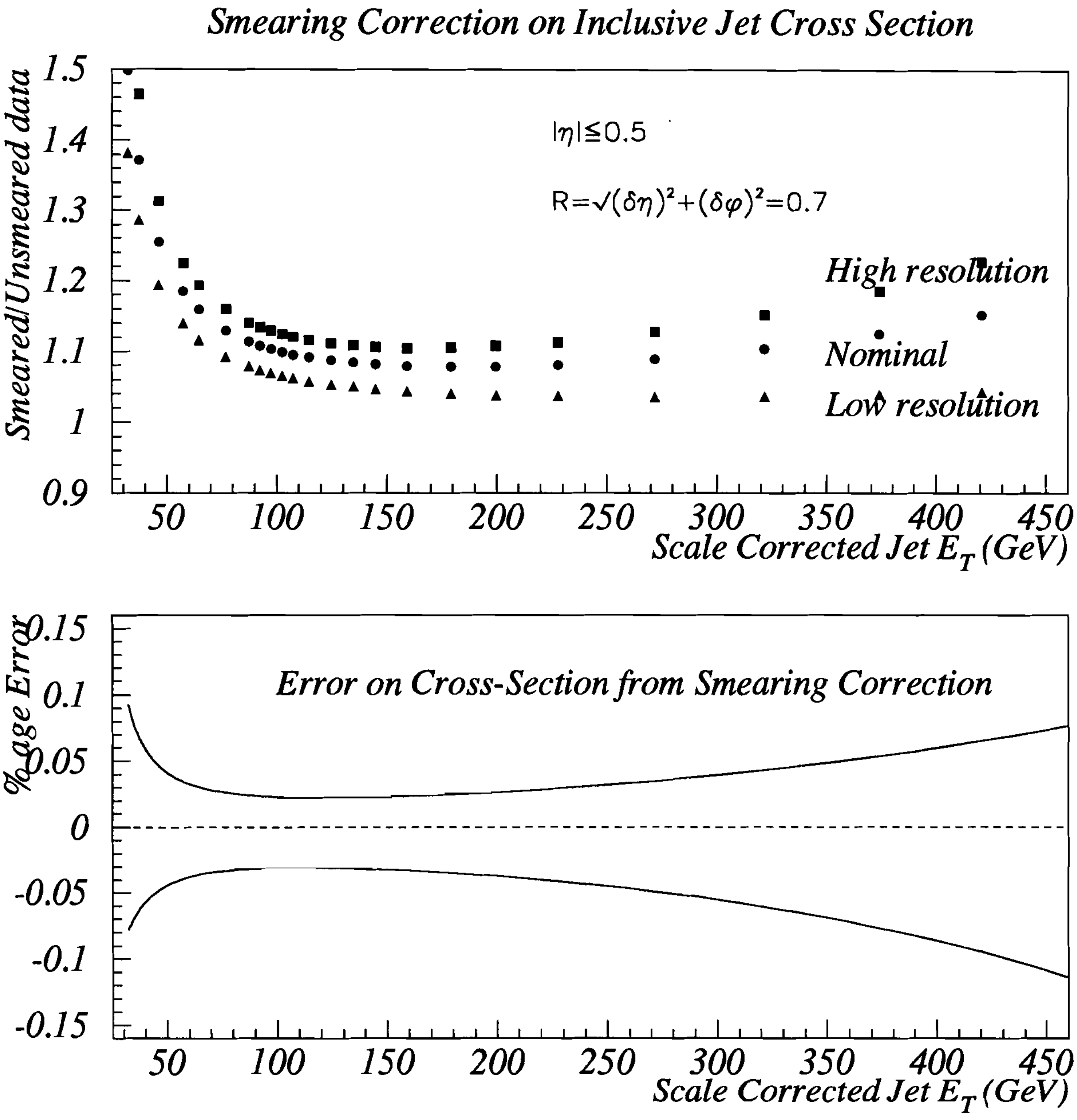

Figure 7.20: Unsmearing correction that is applied to the inclusive jet cross section for 0.7 cone jets (**top**). The unsmearing error due to error on E_T resolution is shown in the **bottom** plot.

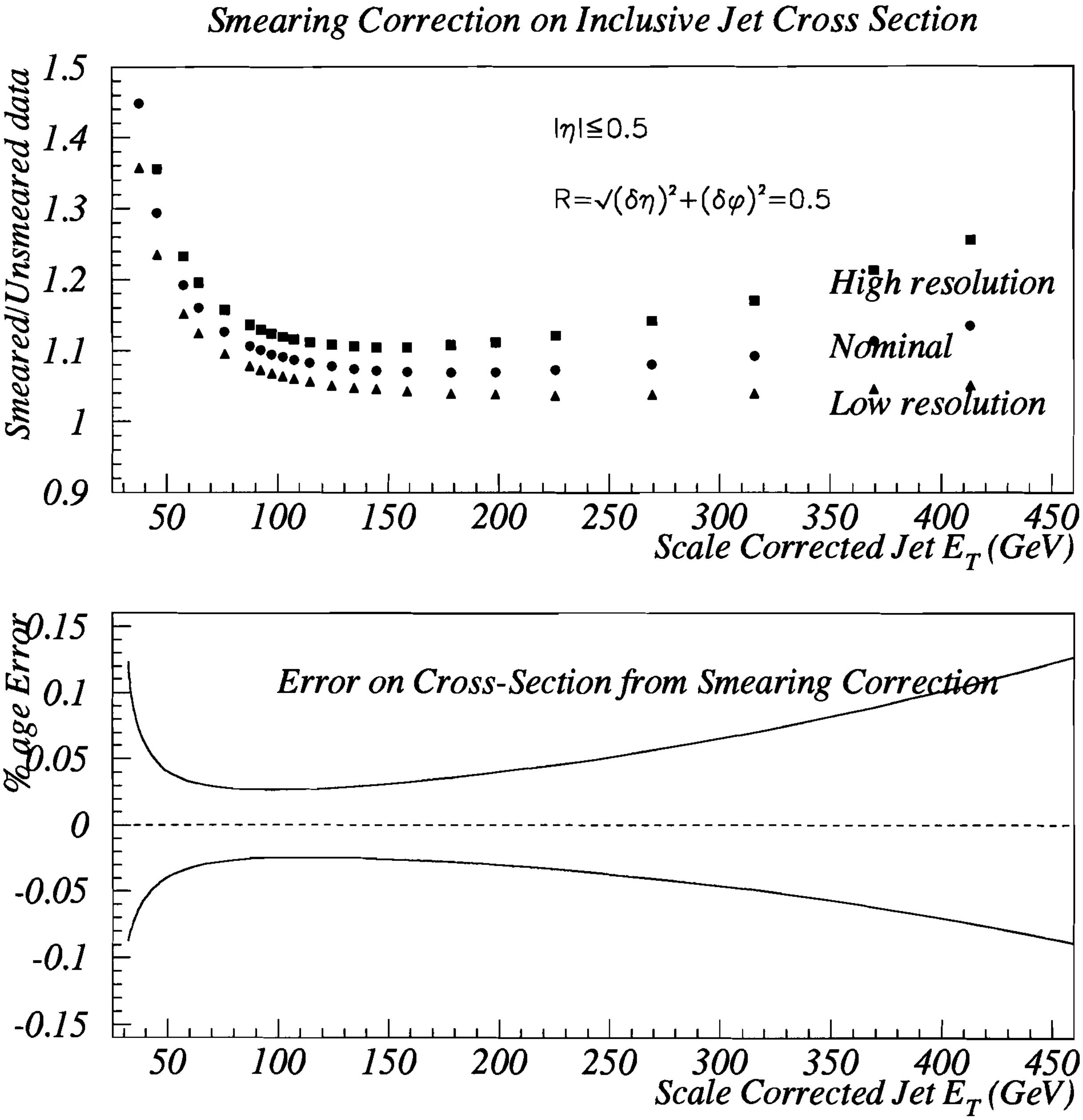

Figure 7.21: Unsmearing correction that is applied to the inclusive jet cross section for 0.5 cone jets (**top**). The unsmearing error due to error on E_T resolution is shown in the **bottom** plot.

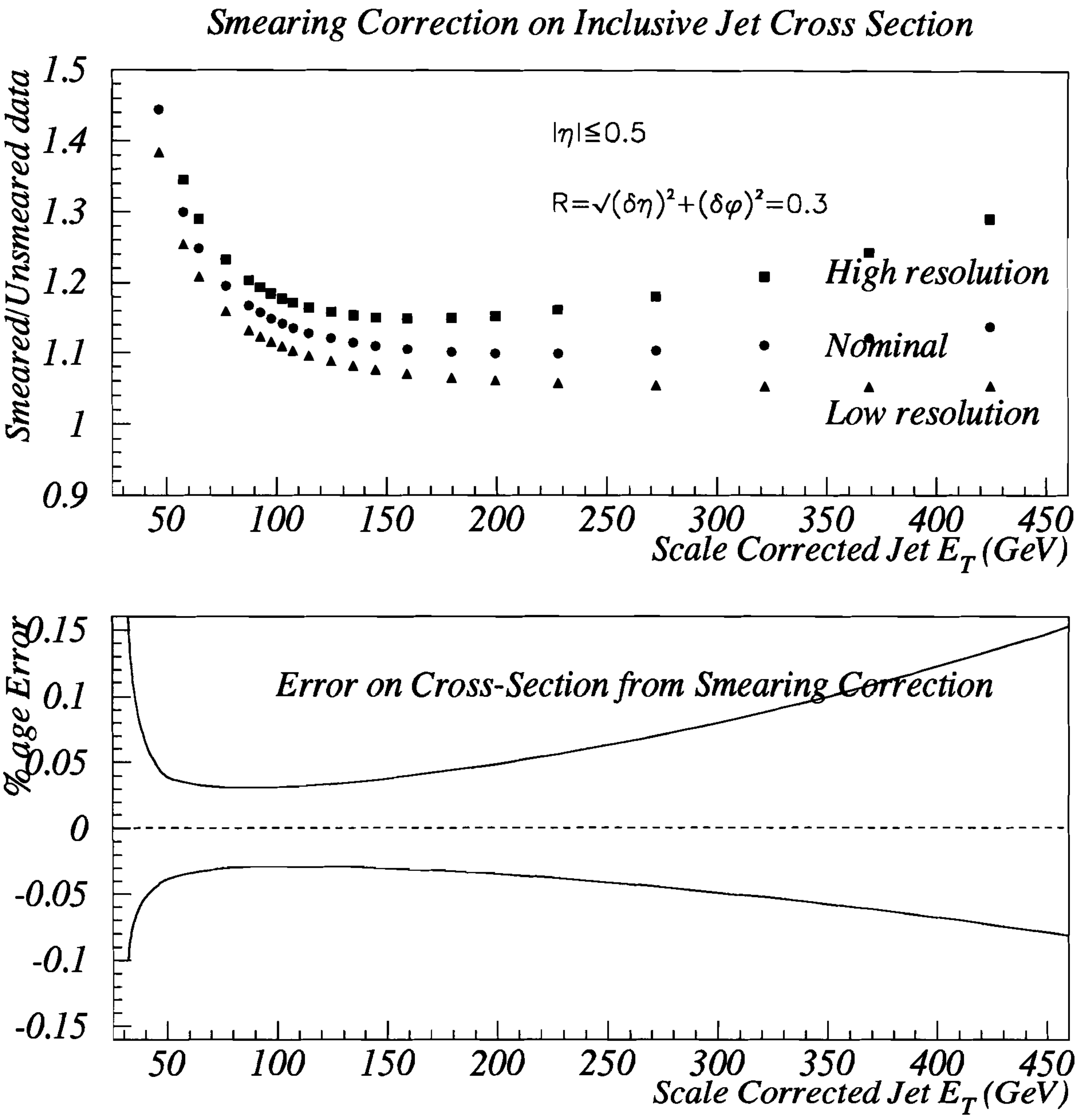

Smearing Correction on Inclusive Jet Cross Section

Figure 7.22: Unsmearing correction that is applied to the inclusive jet cross section for 0.3 cone jets (**top**). The unsmearing error due to error on E_T resolution is shown in the **bottom** plot.

Chapter 8

Results and Conclusions

This chapter presents the inclusive differential jet cross section as a function jet E_T and jet cone size in central pseudorapidities ($|\eta| \leq 0.5$). The results are compared to NLO QCD predictions. The study can be divided into two parts, namely, (1) measurement and comparison of absolute inclusive jet cross section to NLO QCD and (2) measurement and comparison of ratio of cross sections to NLO QCD. The inclusive differential jet cross section as a function of jet E_T in $|\eta| \leq 0.5$, along with the statistical and systematic errors are tabulated for all four jet cone sizes in Tables 8.1, 8.2, 8.3 and 8.4.

8.1 Inclusive Jet Cross Section

The comparison of theoretical expectations with the inclusive jet cross section constitutes a strong test of NLO QCD. Figs. 8.1 and 8.2 show the difference between the data (D) and theory (T) normalized to the theory, $(D-T)/T$, for 1.0, 0.7, 0.5 and 0.3 cone jets, respectively. The NLO QCD predictions are from JETRAD. The theory is calculated with the CTEQ2ML parton distribution function and evaluated at a μ scale of $E_T/2$ of the leading jet in the event. The clustering algorithm uses an R_{sep} of 1.3. The error band is obtained by adding in quadrature all the systematic errors (10-30% for energy scale, $\sim$ 10% for unsmearing, 1% for selection etc.). The 5.4% luminosity uncertainty is not added. The dots are the nominal data points and the vertical bars are statistical errors.

These plots show the percentage deviation of the data from NLO QCD expectations.

A change in the input pdf in the theoretical calculation introduces a normalization uncertainty as well as a shape change. Figs. 8.3, 8.4, 8.5 and 8.6 show $(D-T)/T$ plots for 1.0, 0.7, 0.5 and 0.3 jets, respectively, with the theory evaluated at $\mu = E_T/2$ of the leading jet in the event, but with three different pdf's, namely CTEQ2ML, MRSD0' and CTEQ3M. The CTEQ2ML pdf describes normalization and shape for the larger cone sizes. There is a ~20% deviation between QCD and the cross section for 0.3 cone jets, but this is well within systematic errors. Note that as the cone size decreases the differences between pdf increases. Although all three pdf's describe the data at a cone size of 1.0, only CTEQ2ML does at a cone size of 0.3.

The effect of a change in the μ scale can be seen from Figs. 8.7, 8.8, 8.9 and 8.10, where the theory is evaluated with CTEQ2ML parton distribution function, but for two different values of the μ scale, namely E_T and $E_T/2$ of the leading jet in the event. Apart from a 10-20% normalization uncertainty, the shape of the cross section is described well by NLO QCD evaluated at different μ scales.

The data for all cone sizes and NLO QCD predictions are in agreement for all E_Ts from 80 to 480 GeV, apart from a normalization difference (10-20%) depending on the choice of pdf's and μ scale. NLO QCD with CTEQ2ML pdf and $\mu = E_T/2$ of the leading jet in the event gives the best representation of the data. No significant deviation from NLO QCD predictions has been observed.

8.2 Ratio of Cross Sections

Cross section ratios are evaluated by dividing the cross sections obtained for jets of different cone sizes by the cross section for 0.7 cone jets. The advantage of the ratio is that most of the systematic errors cancel. Selection errors, luminosity errors, unsmearing errors and a part of the energy scale error can be neglected. Also, most of the theoretical uncertainties due to pdf, μ scale and clustering algorithm choices cancel. From Table 2.4 and Figs. 2.10, 2.11 and 2.12 of chapter 2, it can be seen that uncertainties due to pdf's and clustering algorithm choices almost vanish, the theoretical predictions for ratio of cross sections have some dependence on the choice of μ scale.

The data points between various cone sizes are very correlated from bin to bin in E_T and hence, the statistical errors on the ratio of cross sections are highly correlated. In Fig. 8.11, the top plot shows the ratio of cross sections with statistical errors evaluated assuming no correlation between the data points at various cone sizes, and the bottom plot shows the same, but with statistical errors assuming 100% correlation between the data points. We expect the correct statistical errors to lie somewhere in between these extremes. The true error can be estimated by dividing the data sample into two equal halves, and the difference in the ratios between these two halves used as a measure of the statistical error. The difference in the ratios from the different samples divided by $\sqrt{2}$ is used as the statistical error.

Fig. 8.12 shows the ratio of cross sections of jets with different cone sizes to that of the 0.7 cone jets as function of jet E_T in $|\eta| \leq 0.5$. As can be seen, the jet cross section is a function of jet cone size and does decrease with jet cone size. Figs. 8.13, 8.14 and 8.15 show a comparison of ratio of cross sections of 1.0, 0.5 and 0.3 cone jets to that of 0.7 jets with NLO QCD predictions using CTEQ2ML. The clustering algorithm uses a R_{sep} of 1.3. The theory is evaluated at two different μ scales, namely, E_T and $E_T/2$ of the leading jet in the event. As can be seen from the plots, the data favours $\mu = E_T/2$ and is in qualitative agreement with NLO QCD prediction at all E_Ts from 80 to 480 GeV in $|\eta| \leq 0.5$. In fact, only the 0.3/0.7 ratio differs by more than 20% in the region 200 GeV $< E_T <$ 300 GeV.

Fig. 8.16 shows the ratio of cross sections for all the cone sizes plotted on the same graph and compared to NLO QCD prediction evaluated with three different pdf's, namely CTEQ2ML, CTEQ3M and MRSD0'. The perturbative expansion is evaluated at $\mu = E_T/2$. As can be seen all input pdf's describe the data equally well. The ratios do not depend on parton distribution functions.

The variation of the cross section with jet cone size at a fixed E_T is also of interest. Figs. 8.17 and 8.18 show this dependence at four fixed E_Ts, namely 102, 159, 227 and 321 GeV as a function of jet cone size. The cone size dependence is compared to NLO QCD predictions evaluated with two different pdf's, namely CTEQ2ML and MRSD0', at a μ scale of $E_T/2$ of the leading jet in the event. As can be seen from the plots, the data are in good agreement with NLO QCD prediction.

8.3 Conclusions

The inclusive jet cross section for all cone sizes is in good agreement with NLO QCD predictions at all E_T from 80 to 480 GeV in $|\eta| \leq 0.5$. The cross section is well described by many NLO QCD predictions. In particular, data at all cone sizes agree very well with NLO QCD calculations using CTEQ2ML and $\mu = E_T/2$ of the leading jet in the event. No evidence of any deviation from the Standard Model has been observed.

From the ratios, it can be seen that the jet cross section decreases with jet cone size. The ratio of cross sections are in good agreement with NLO QCD. The ratios are independent of the pdf and clustering choice. However, the ratios depend on the μ scale; and prefer a μ scale of $E_T/2$ of the leading jet in the event. Only statistical errors are presented for the ratios, however the systematic errors are expected to be very small.

Table 8.1: Cross Section and associated statistical and systematic errors for 1.0 cone jets in $|\eta| \leq 0.5$.

Jet E_T in GeV	Cross Section in nb/GeV	Statistical Error	Positive Systematic Error	Negative Systematic Error
87.42	0.149E+01	0.182E-01	0.394E+00	-0.910E-01
92.43	0.108E+01	0.155E-01	0.271E+00	-0.781E-01
97.44	0.804E+00	0.133E-01	0.178E+00	-0.782E-01
102.44	0.602E+00	0.115E-01	0.125E+00	-0.712E-01
107.43	0.434E+00	0.975E-02	0.110E+00	-0.487E-01
114.73	0.307E+00	0.578E-02	0.637E-01	-0.551E-01
124.83	0.179E+00	0.440E-02	0.530E-01	-0.438E-01
134.81	0.105E+00	0.121E-02	0.494E-01	-0.387E-01
144.81	0.657E-01	0.951E-03	0.474E-01	-0.378E-01
159.27	0.357E-01	0.495E-03	0.473E-01	-0.379E-01
179.33	0.158E-01	0.329E-03	0.495E-01	-0.386E-01
199.41	0.705E-02	0.167E-03	0.526E-01	-0.399E-01
227.59	0.252E-02	0.708E-04	0.581E-01	-0.426E-01
271.55	0.647E-03	0.322E-04	0.695E-01	-0.485E-01
321.28	0.138E-03	0.149E-04	0.878E-01	-0.580E-01
376.02	0.215E-04	0.595E-05	0.117E+00	-0.733E-01
422.85	0.555E-05	0.306E-05	0.154E+00	-0.923E-01
473.69	0.271E-05	0.218E-05	0.210E+00	-0.122E+00

Table 8.2: Cross Section and associated statistical and systematic errors for 0.7 cone jets in $|\eta| \leq 0.5$.

Jet E_T in GeV	Cross Section in nb/GeV	Statistical Error	Positive Systematic Error	Negative Systematic Error
87.42	0.123E+01	0.164E-01	0.192E+00	-0.135E+00
92.41	0.891E+00	0.139E-01	0.141E+00	-0.100E+00
97.44	0.664E+00	0.120E-01	0.951E-01	-0.876E-01
102.47	0.488E+00	0.103E-01	0.785E-01	-0.668E-01
107.43	0.369E+00	0.889E-02	0.612E-01	-0.588E-01
114.76	0.251E+00	0.518E-02	0.450E-01	-0.523E-01
124.82	0.147E+00	0.396E-02	0.400E-01	-0.445E-01
134.81	0.904E-01	0.111E-02	0.374E-01	-0.425E-01
144.85	0.545E-01	0.861E-03	0.376E-01	-0.418E-01
159.29	0.294E-01	0.447E-03	0.380E-01	-0.427E-01
179.28	0.126E-01	0.292E-03	0.402E-01	-0.447E-01
199.51	0.584E-02	0.152E-03	0.431E-01	-0.472E-01
227.87	0.201E-02	0.631E-04	0.482E-01	-0.516E-01
271.81	0.505E-03	0.284E-04	0.583E-01	-0.600E-01
321.76	0.111E-03	0.134E-04	0.737E-01	-0.719E-01
374.06	0.198E-04	0.570E-05	0.949E-01	-0.874E-01
420.59	0.542E-05	0.301E-05	0.119E+00	-0.104E+00
468.62	0.266E-05	0.213E-05	0.150E+00	-0.124E+00

Table 8.3: Cross Section and associated statistical and systematic errors for 0.5 cone jets in $|\eta| \leq 0.5$.

Jet E_T in GeV	Cross Section in nb/GeV	Statistical Error	Positive Systematic Error	Negative Systematic Error
87.38	0.952E+00	0.144E-01	0.138E+00	-0.102E+00
92.38	0.694E+00	0.122E-01	0.106E+00	-0.754E-01
97.43	0.517E+00	0.105E-01	0.798E-01	-0.647E-01
102.42	0.378E+00	0.899E-02	0.723E-01	-0.482E-01
107.48	0.306E+00	0.808E-02	0.447E-01	-0.567E-01
114.62	0.201E+00	0.462E-02	0.452E-01	-0.422E-01
124.65	0.117E+00	0.352E-02	0.421E-01	-0.368E-01
134.60	0.739E-01	0.999E-03	0.395E-01	-0.363E-01
144.66	0.456E-01	0.785E-03	0.400E-01	-0.358E-01
158.69	0.243E-01	0.405E-03	0.413E-01	-0.363E-01
178.48	0.106E-01	0.267E-03	0.442E-01	-0.377E-01
198.72	0.488E-02	0.138E-03	0.478E-01	-0.397E-01
225.76	0.182E-02	0.598E-04	0.537E-01	-0.430E-01
269.65	0.416E-03	0.257E-04	0.656E-01	-0.497E-01
315.83	0.930E-04	0.122E-04	0.814E-01	-0.586E-01
369.70	0.189E-04	0.554E-05	0.104E+00	-0.715E-01
413.10	0.540E-05	0.303E-05	0.127E+00	-0.840E-01
473.10	0.136E-05	0.152E-05	0.165E+00	-0.104E+00

Table 8.4: Cross Section and associated statistical and systematic errors for 0.3 cone jets in $|\eta| \leq 0.5$.

Jet E_T in GeV	Cross Section in nb/GeV	Statistical Error	Positive Systematic Error	Negative Systematic Error
87.44	0.723E+00	0.130E-01	0.119E+00	-0.834E-01
92.41	0.568E+00	0.114E-01	0.651E-01	-0.985E-01
97.46	0.412E+00	0.968E-02	0.642E-01	-0.698E-01
102.47	0.314E+00	0.843E-02	0.551E-01	-0.625E-01
107.42	0.235E+00	0.726E-02	0.536E-01	-0.523E-01
114.74	0.158E+00	0.420E-02	0.503E-01	-0.460E-01
124.78	0.928E-01	0.320E-02	0.490E-01	-0.421E-01
134.77	0.580E-01	0.903E-03	0.479E-01	-0.413E-01
144.83	0.358E-01	0.708E-03	0.482E-01	-0.410E-01
159.35	0.204E-01	0.377E-03	0.491E-01	-0.412E-01
179.41	0.883E-02	0.247E-03	0.517E-01	-0.421E-01
199.29	0.420E-02	0.130E-03	0.550E-01	-0.434E-01
227.76	0.167E-02	0.579E-04	0.608E-01	-0.460E-01
272.26	0.396E-03	0.252E-04	0.726E-01	-0.514E-01
321.64	0.958E-04	0.125E-04	0.896E-01	-0.595E-01
369.25	0.124E-04	0.449E-05	0.110E+00	-0.694E-01
424.52	0.535E-05	0.364E-05	0.141E+00	-0.839E-01
468.90	0.160E-05	0.164E-05	0.171E+00	-0.983E+00

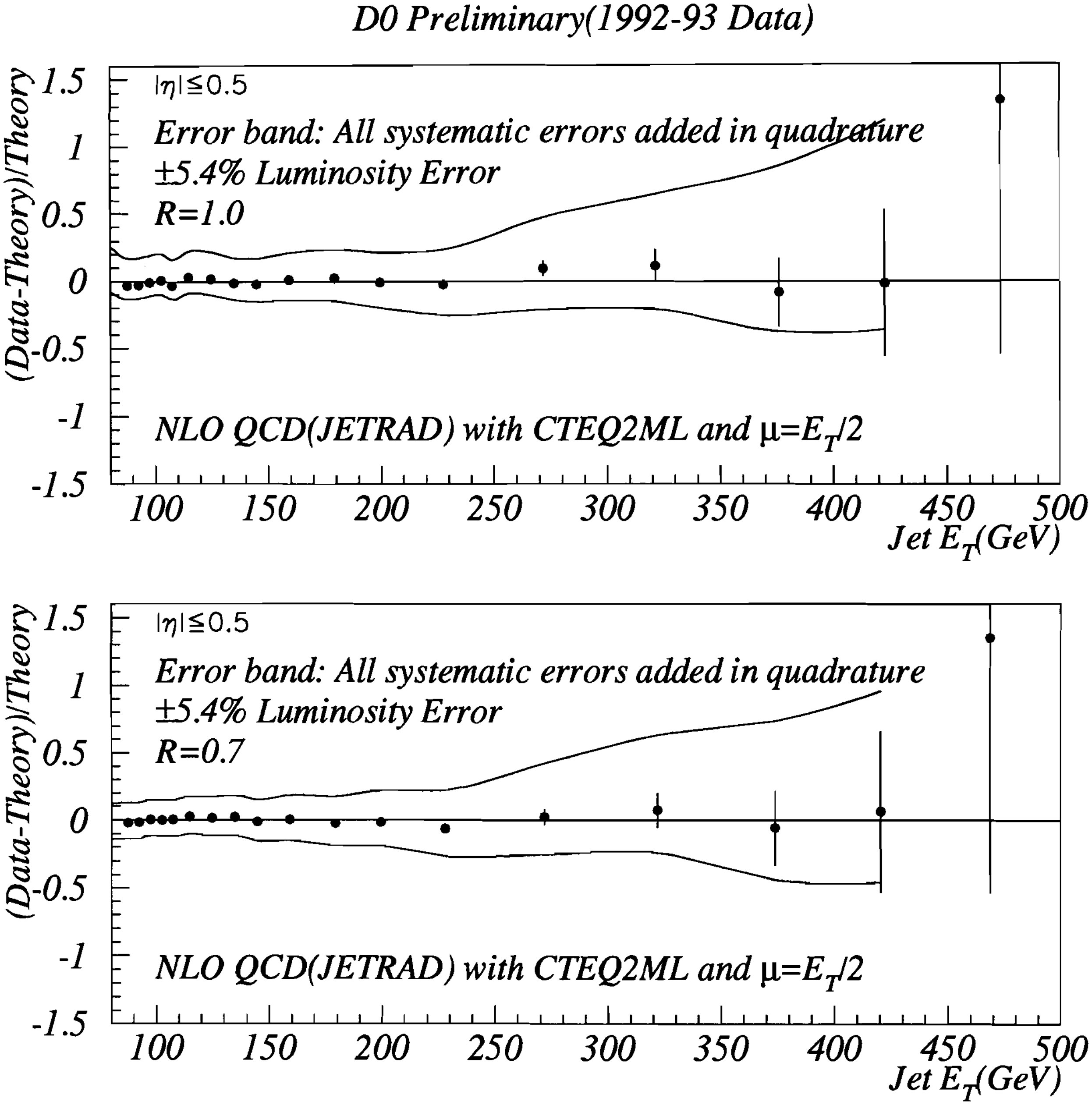

Figure 8.1: (Data-Theory)/Theory vs. Jet E_T for 1.0 (top) and 0.7 (bottom) cone jets in $|\eta| \leq 0.5$. The theory is NLO QCD (JETRAD) evaluated at $\mu = E_T/2$ of the leading jet in the event with the CTEQ2ML parton distribution function. The circles are nominal data points and the error band gives the total systematic uncertainty. The ±5.4% luminosity error is not included in the band. The error bars are statistical.

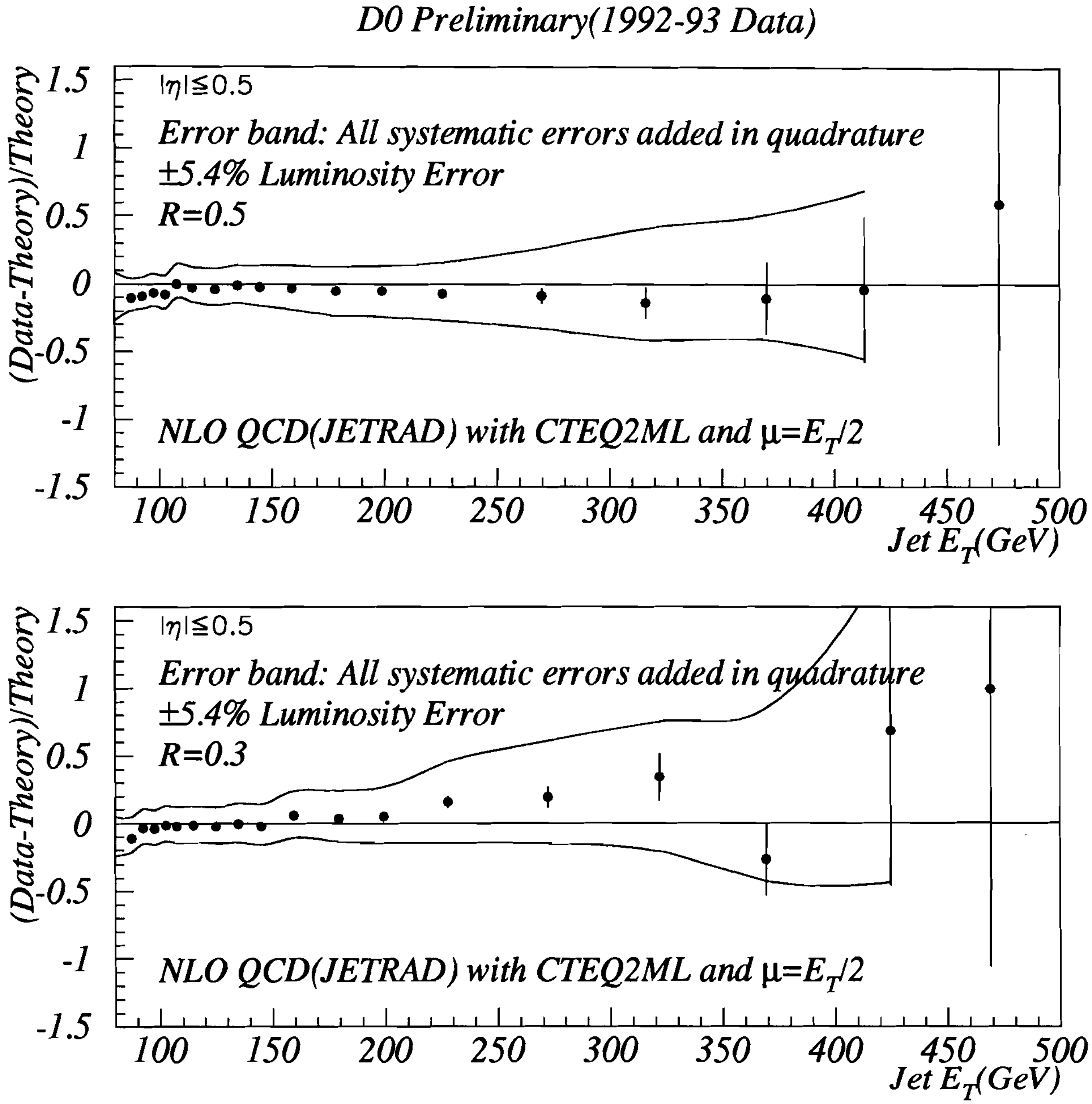

Figure 8.2: (Data-Theory)/Theory vs. Jet E_T for 0.5 (top) and 0.3 (bottom) cone jets in $|\eta| \leq 0.5$. The theory is NLO QCD (JETRAD) evaluated at $\mu = E_T/2$ of the leading jet in the event with the CTEQ2ML parton distribution function. The circles are nominal data points and the error band gives the total systematic uncertainty. The ±5.4% luminosity error is not included in the band. The error bars are statistical.

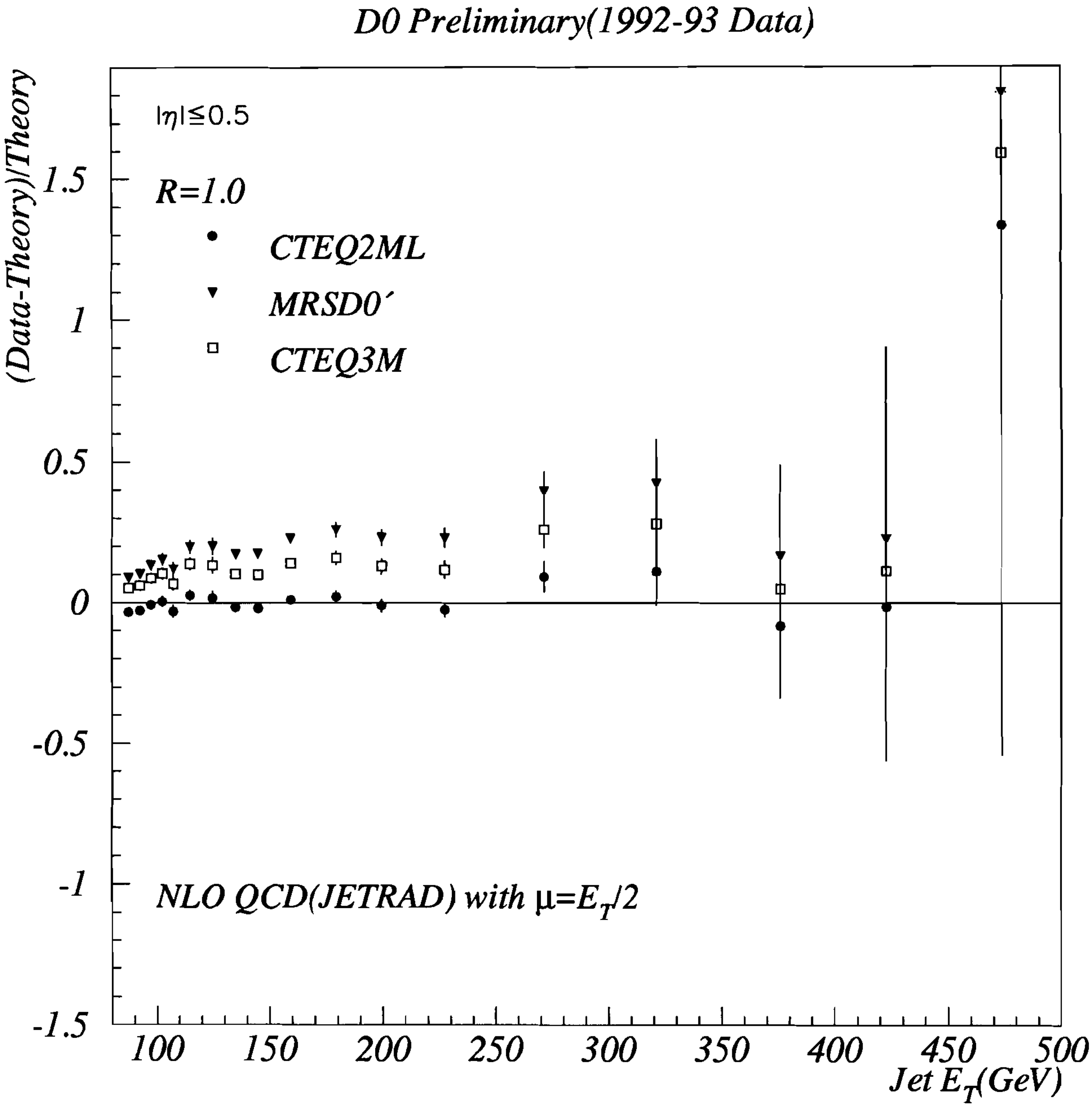

Figure 8.3: (Data-Theory)/Theory vs. Jet E_T for 1.0 cone jets in $|\eta| \leq 0.5$. The theory is NLO QCD (JETRAD) evaluated at $\mu = E_T/2$, but with three different pdf's, CTEQ2ML, MRSD0' and CTEQ3M.

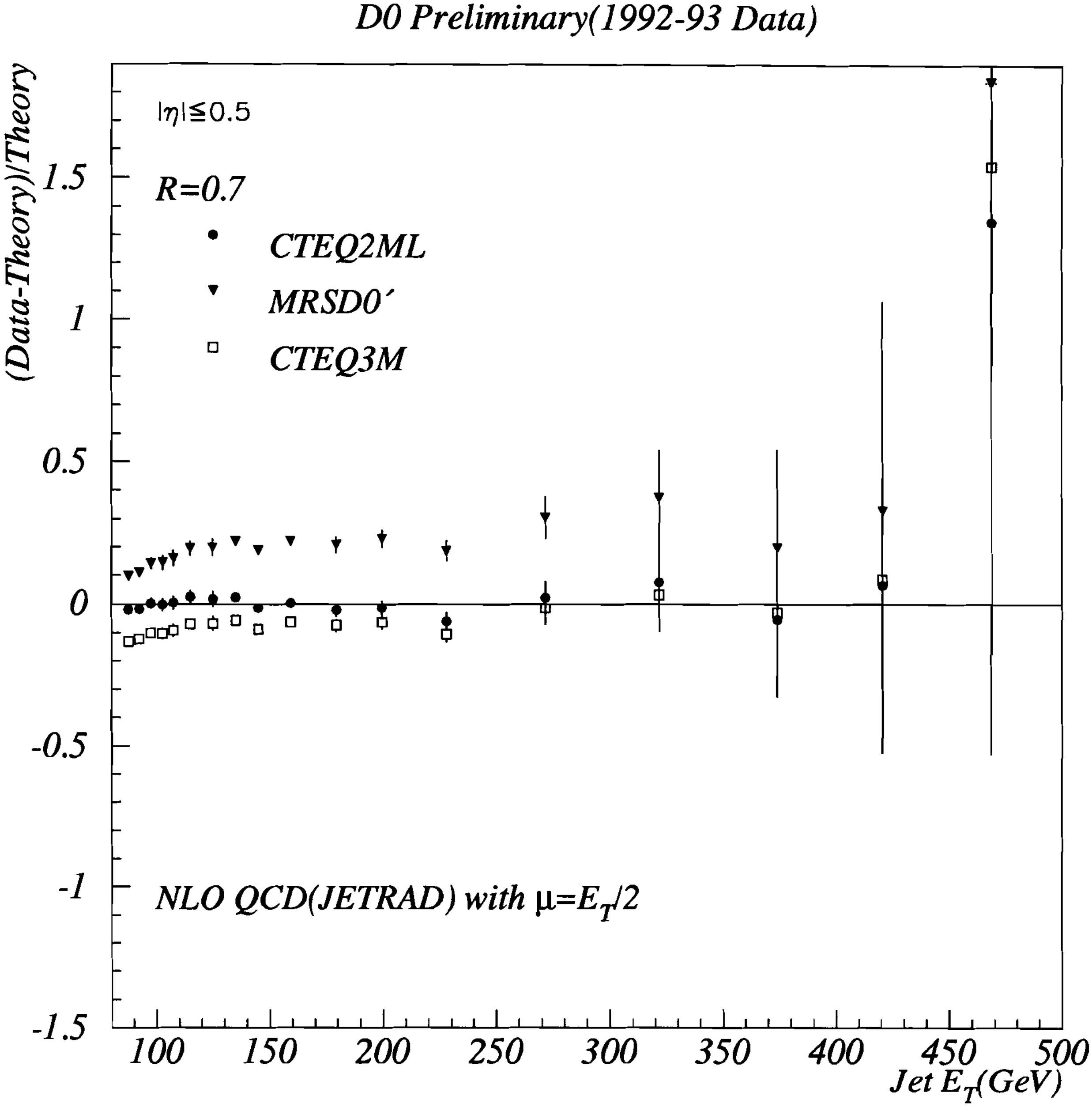

Figure 8.4: (Data-Theory)/Theory vs. Jet E_T for 0.7 cone jets in $|\eta| \leq 0.5$. The theory is NLO QCD (JETRAD) evaluated at $\mu{=}E_T/2$, but with three different pdf's, CTEQ2ML, MRSD0' and CTEQ3M.

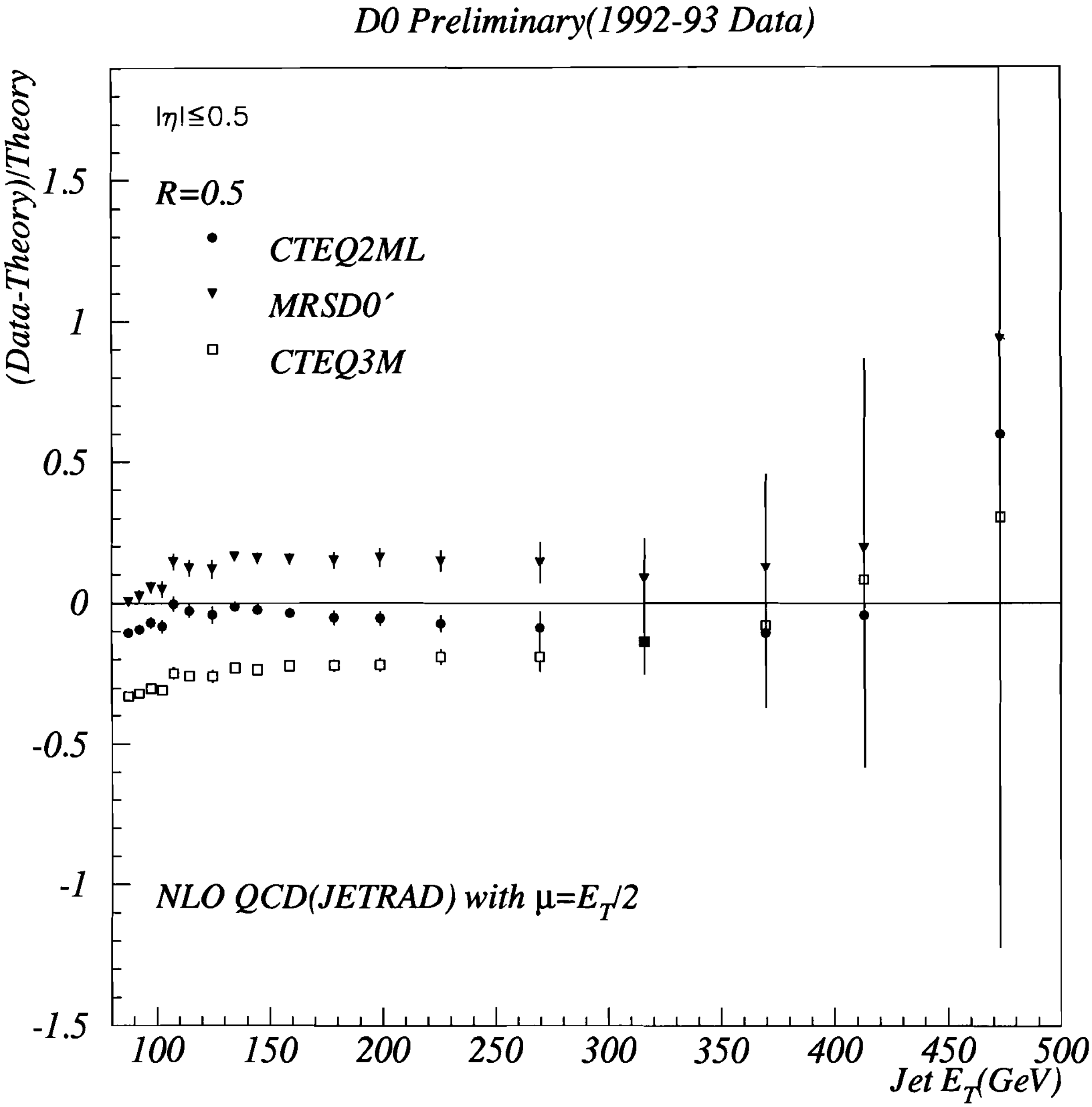

Figure 8.5: (Data-Theory)/Theory vs. Jet E_T for 0.5 cone jets in $|\eta| \leq 0.5$. The theory is NLO QCD (JETRAD) evaluated at μ=$E_T/2$, but with three different pdf's, CTEQ2ML, MRSD0' and CTEQ3M.

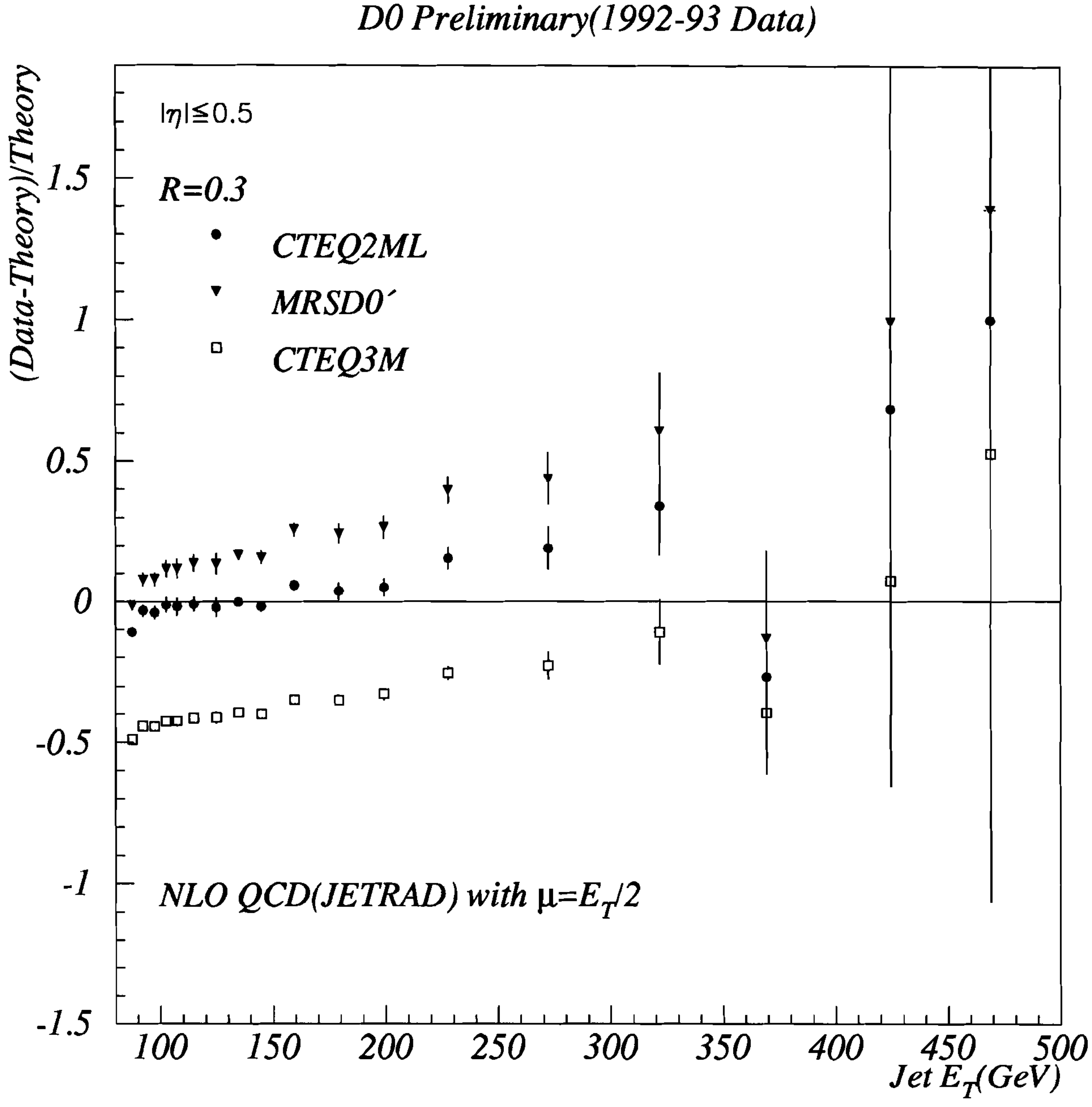

Figure 8.6: (Data-Theory)/Theory vs. Jet E_T for 0.3 cone jets in $|\eta| \leq 0.5$. The theory is NLO QCD (JETRAD) evaluated at $\mu = E_T/2$, but with three different pdf's, CTEQ2ML, MRSD0' and CTEQ3M.

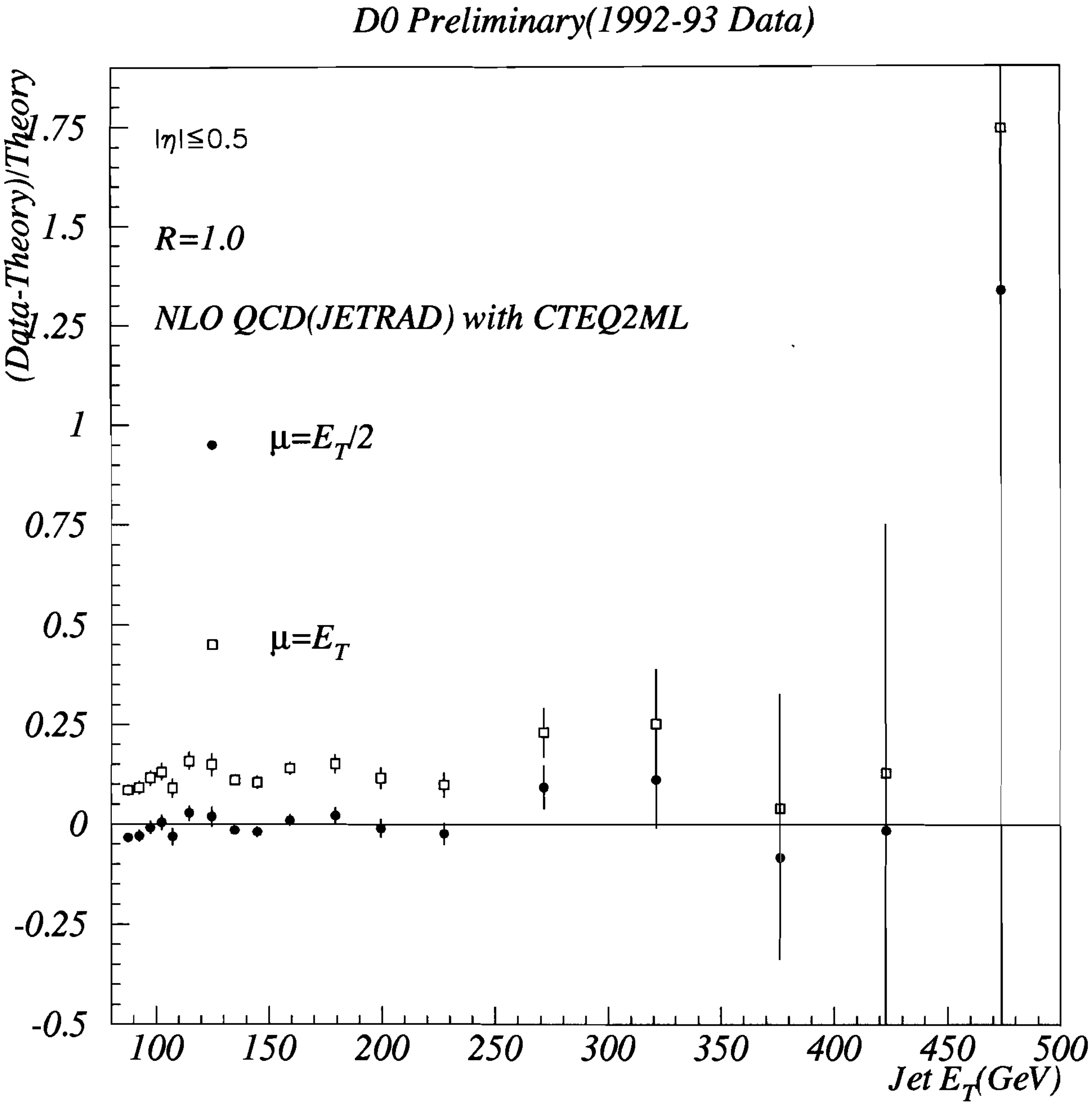

Figure 8.7: (Data-Theory)/Theory vs. Jet E_T for 1.0 cone jets in $|\eta| \leq 0.5$. The theory is NLO QCD (JETRAD) evaluated with CTEQ2ML, but for two different values of the μ scale.

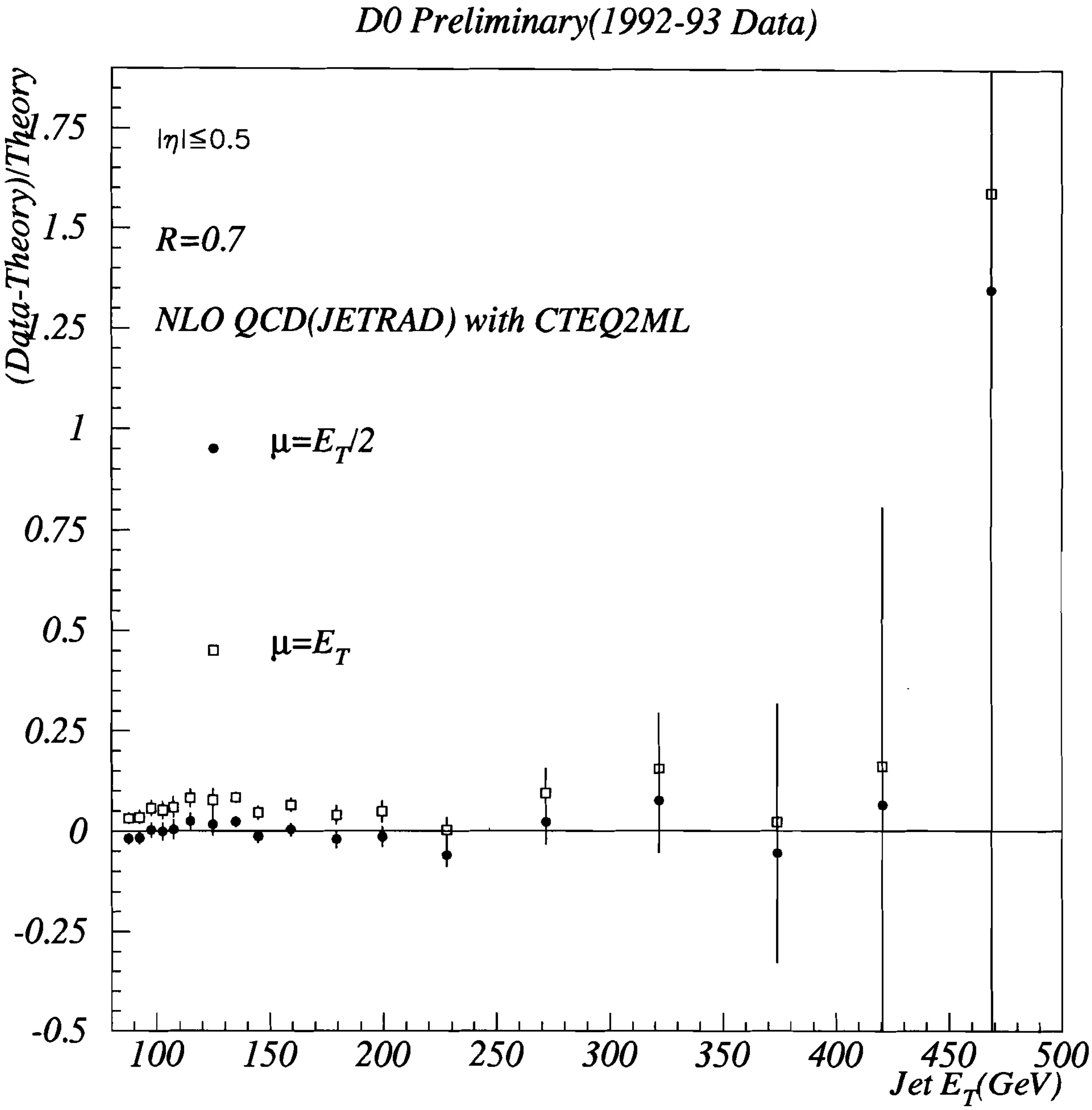

Figure 8.8: (Data-Theory)/Theory vs. Jet E_T for 0.7 cone jets in $|\eta| \leq 0.5$. The theory is NLO QCD (JETRAD) evaluated with CTEQ2ML, but for two different values of the μ scale.

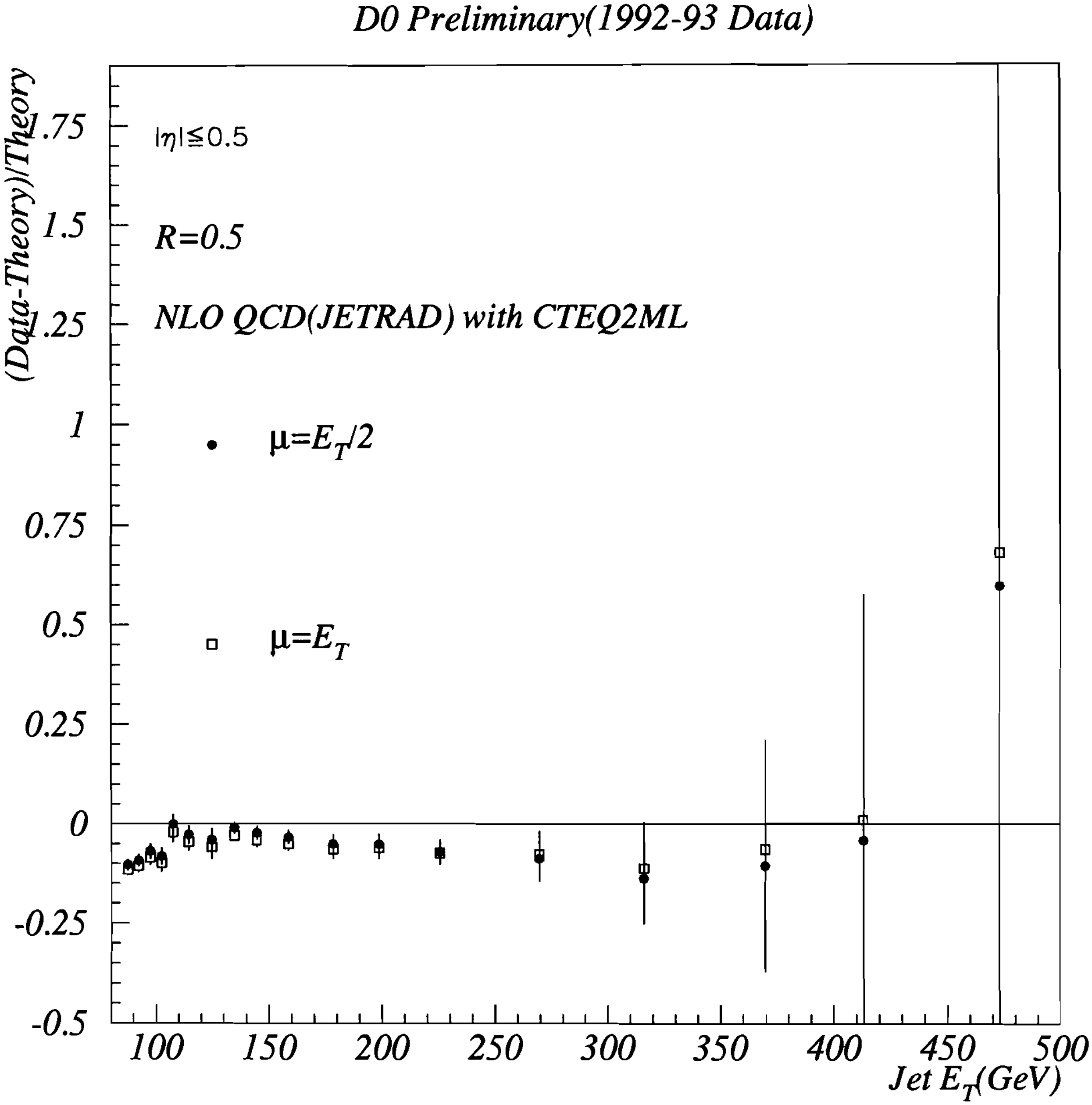

Figure 8.9: (Data-Theory)/Theory vs. Jet E_T for 0.5 cone jets in $|\eta| \leq 0.5$. The theory is NLO QCD (JETRAD) evaluated with CTEQ2ML, but for two different values of the μ scale.

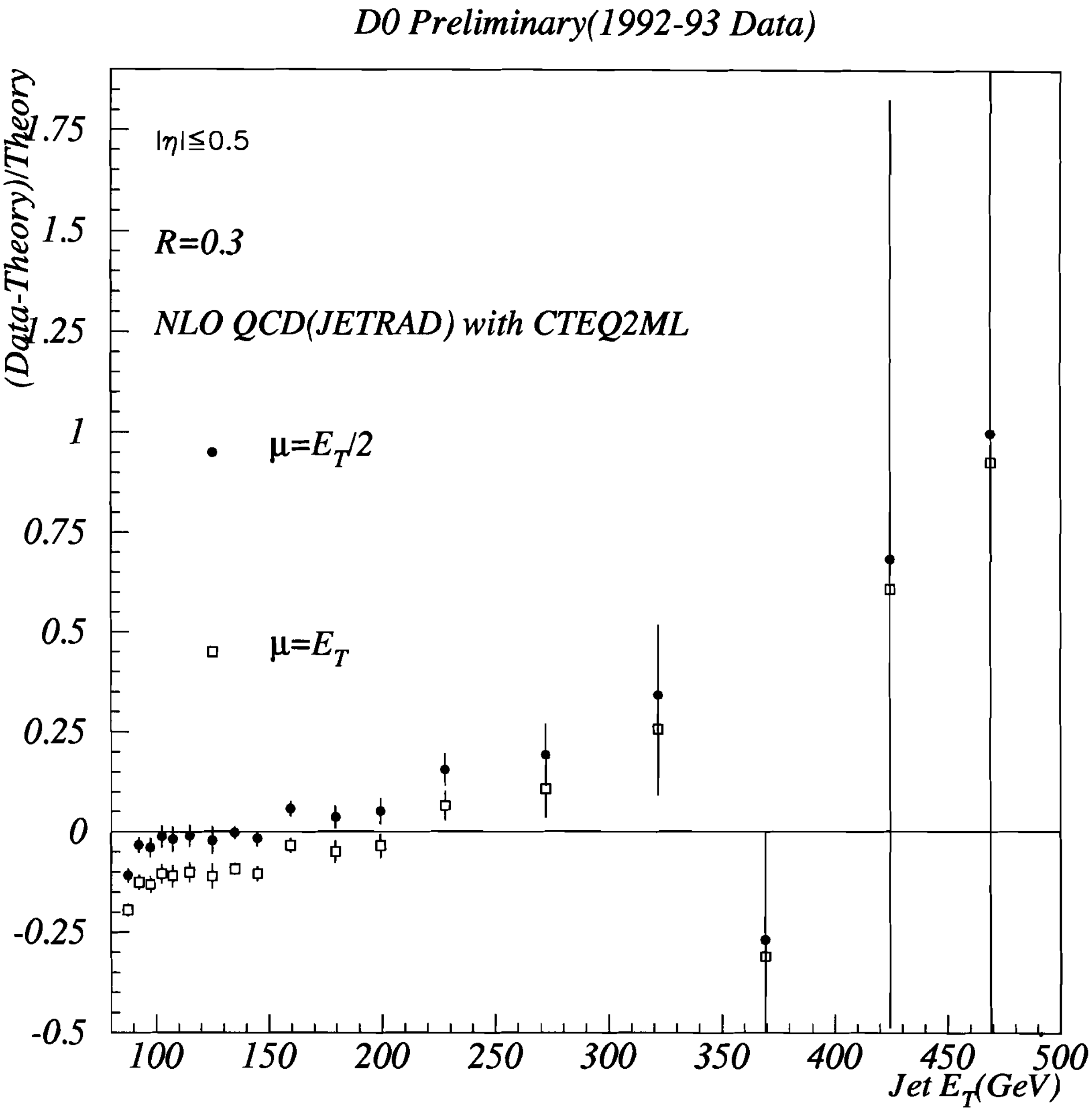

Figure 8.10: (Data-Theory)/Theory vs. Jet E_T for 0.3 cone jets in $|\eta| \leq 0.5$. The theory is NLO QCD (JETRAD) evaluated with CTEQ2ML, but for two different values of the μ scale. Apart from a normalization uncertainty, shape is well described by NLO QCD.

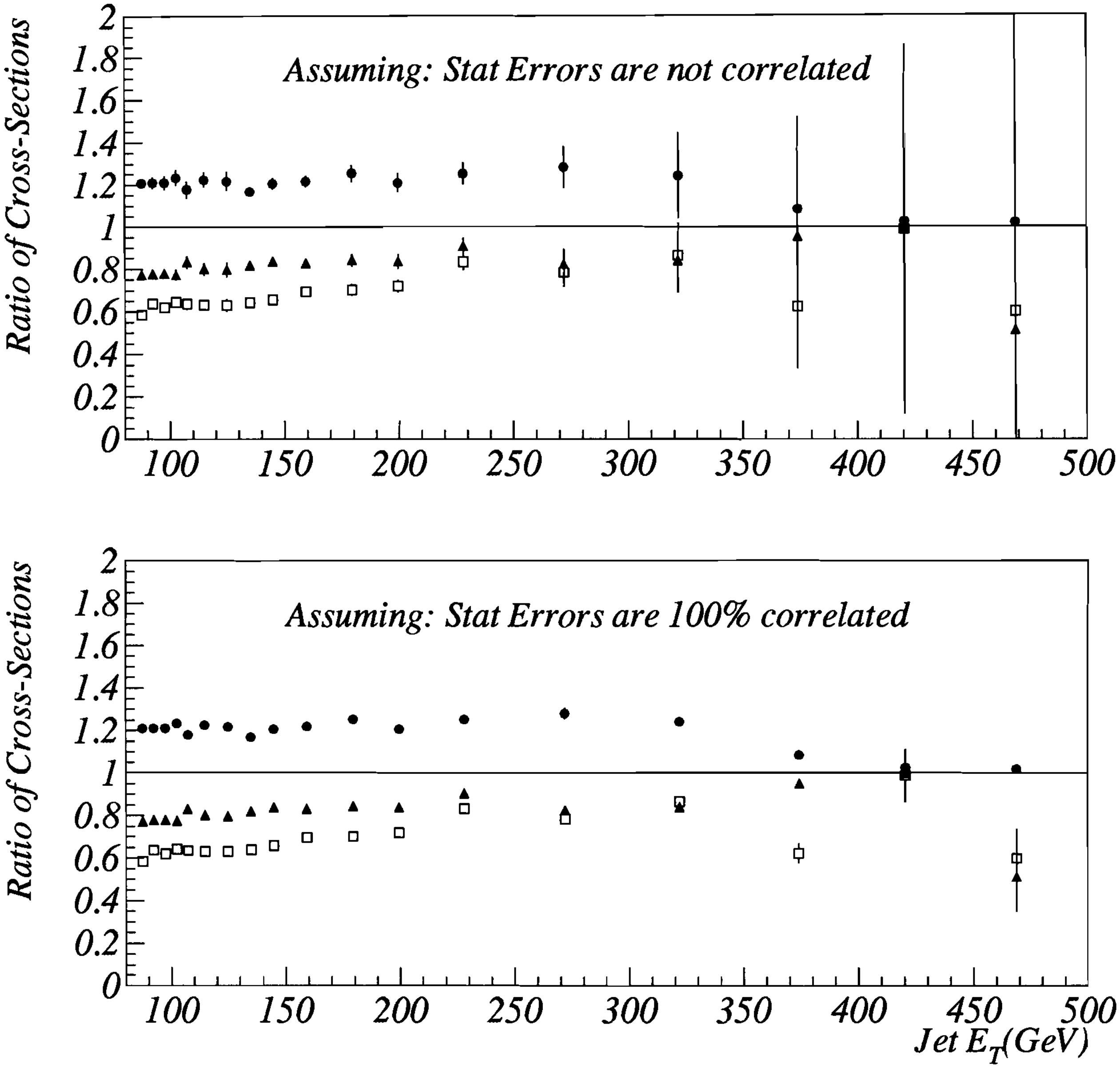

Figure 8.11: Ratio of cross sections in $|\eta| \leq 0.5$. **Top** plot is with statistical errors evaluated assuming no correlation between data points at various cone sizes and **bottom** plot is with statistical errors evaluated assuming 100% correlation between data points at various cone sizes.

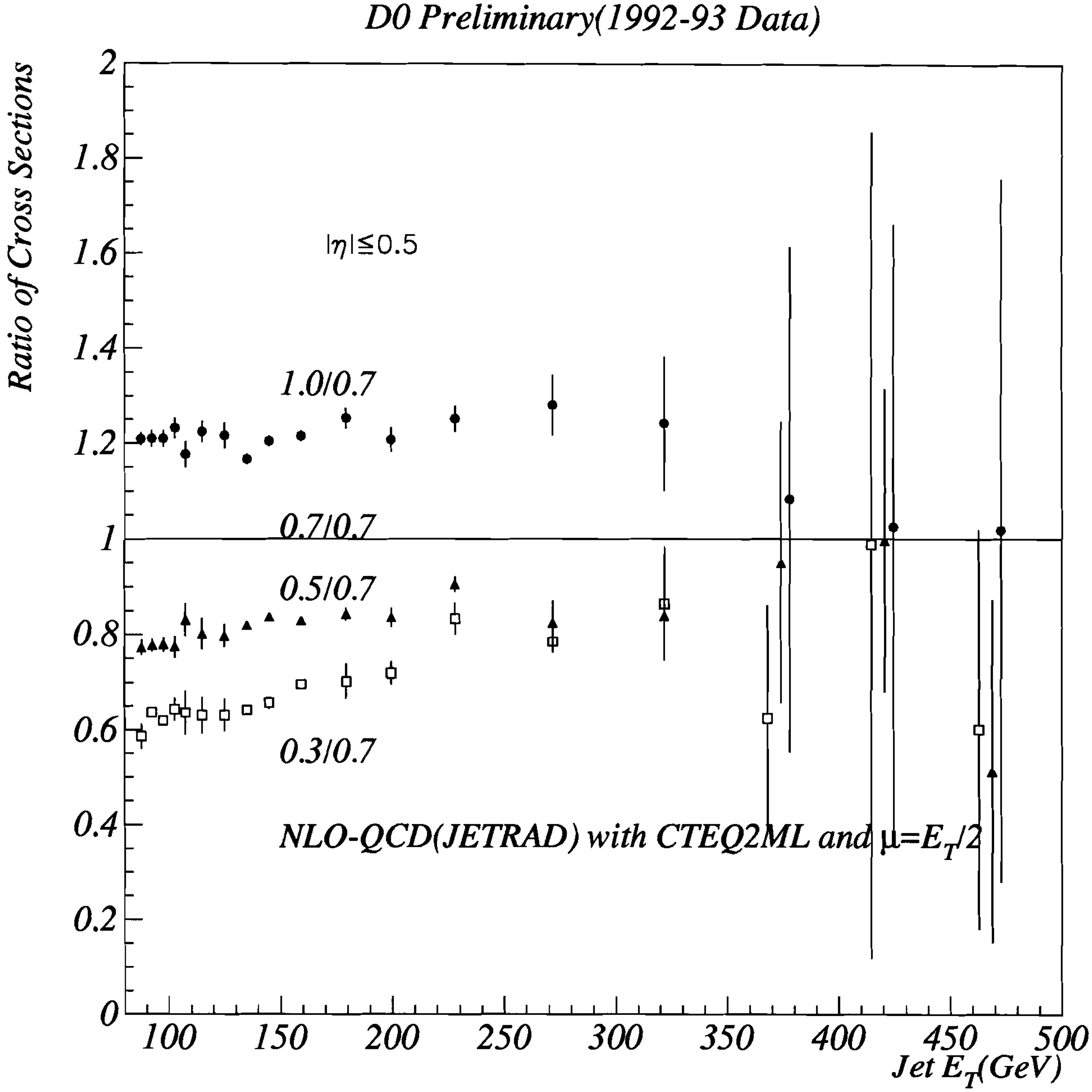

Figure 8.12: Ratio of Cross Sections of 1.0, 0.5 and 0.3 cone jets to that of 0.7 cone jets as a function of jet E_T in $|\eta| \leq 0.5$.

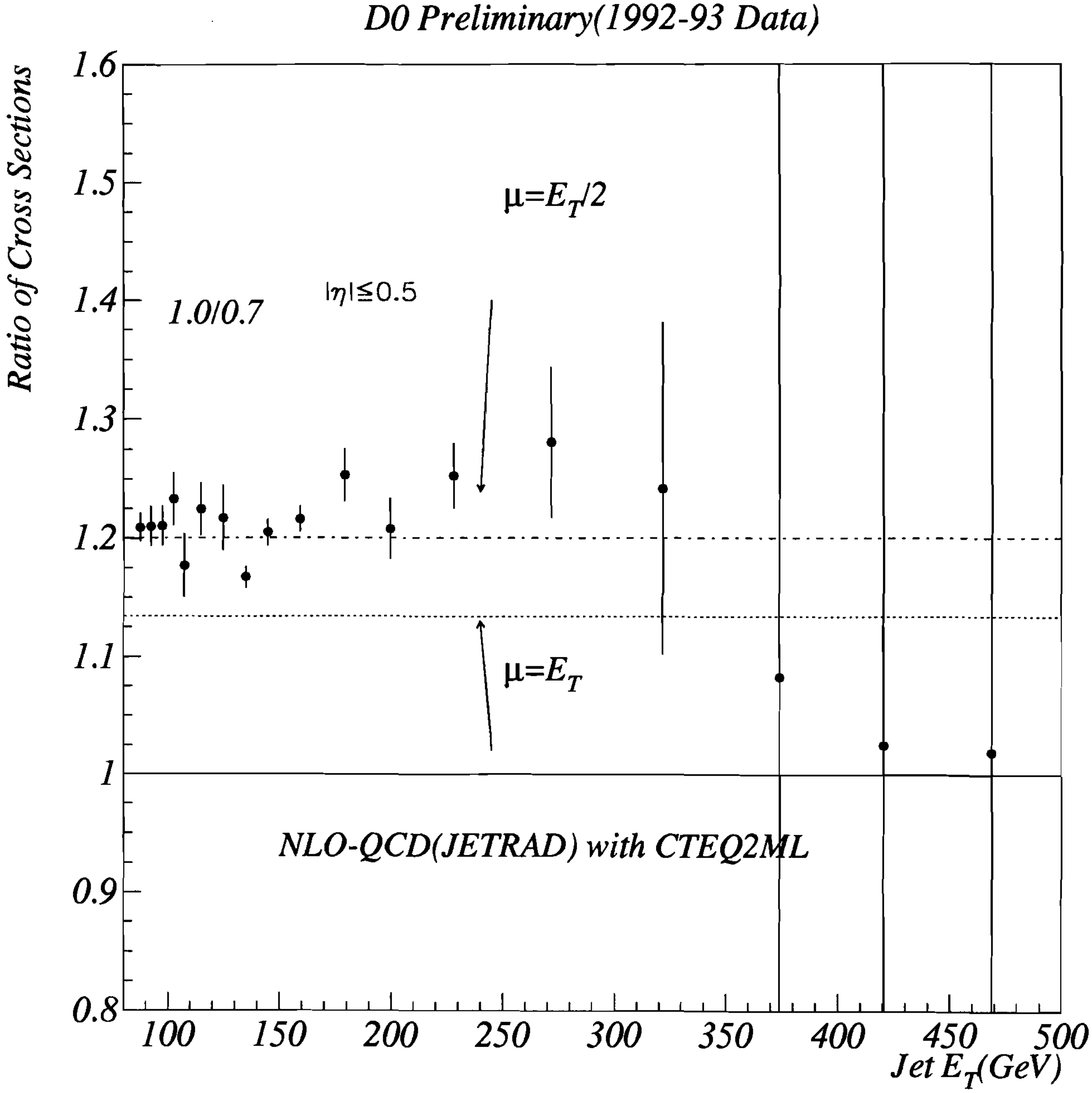

Figure 8.13: Ratio of Cross Section of 1.0 cone jets to that of 0.7 cone jets vs. Jet E_T in $|\eta| \leq 0.5$ compared to NLO QCD evaluated with CTEQ2ML pdf at two different values of μ scale, namely, E_T and $E_T/2$ of the leading jet in the event. Data prefers $\mu = E_T/2$.

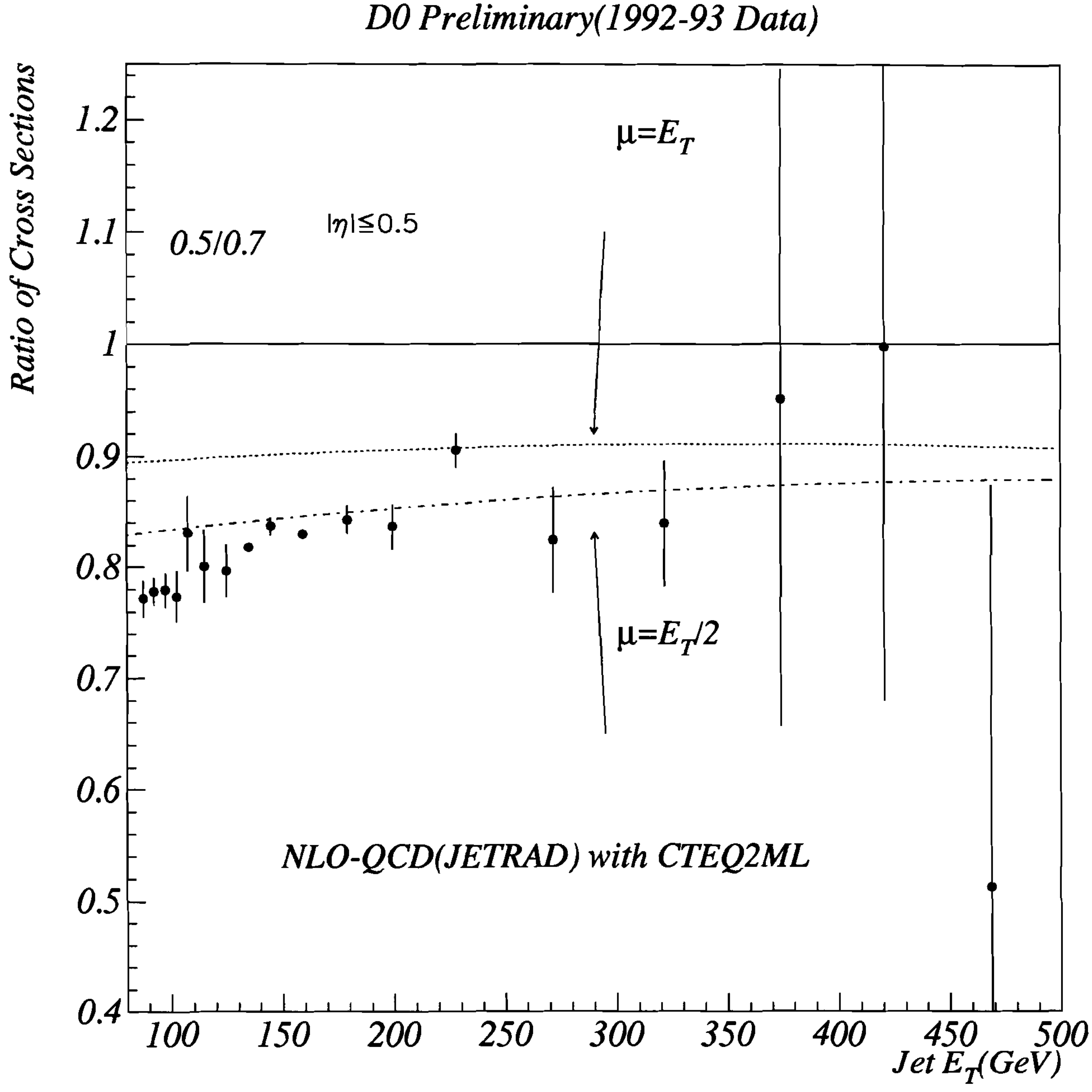

Figure 8.14: Ratio of Cross Section of 0.5 cone jets to that of 0.7 cone jets vs. Jet E_T in $|\eta| \leq 0.5$ compared to NLO QCD evaluated with CTEQ2ML pdf at two different values of μ scale, namely, E_T and $E_T/2$ of the leading jet in the event. Data prefers $\mu = E_T/2$.

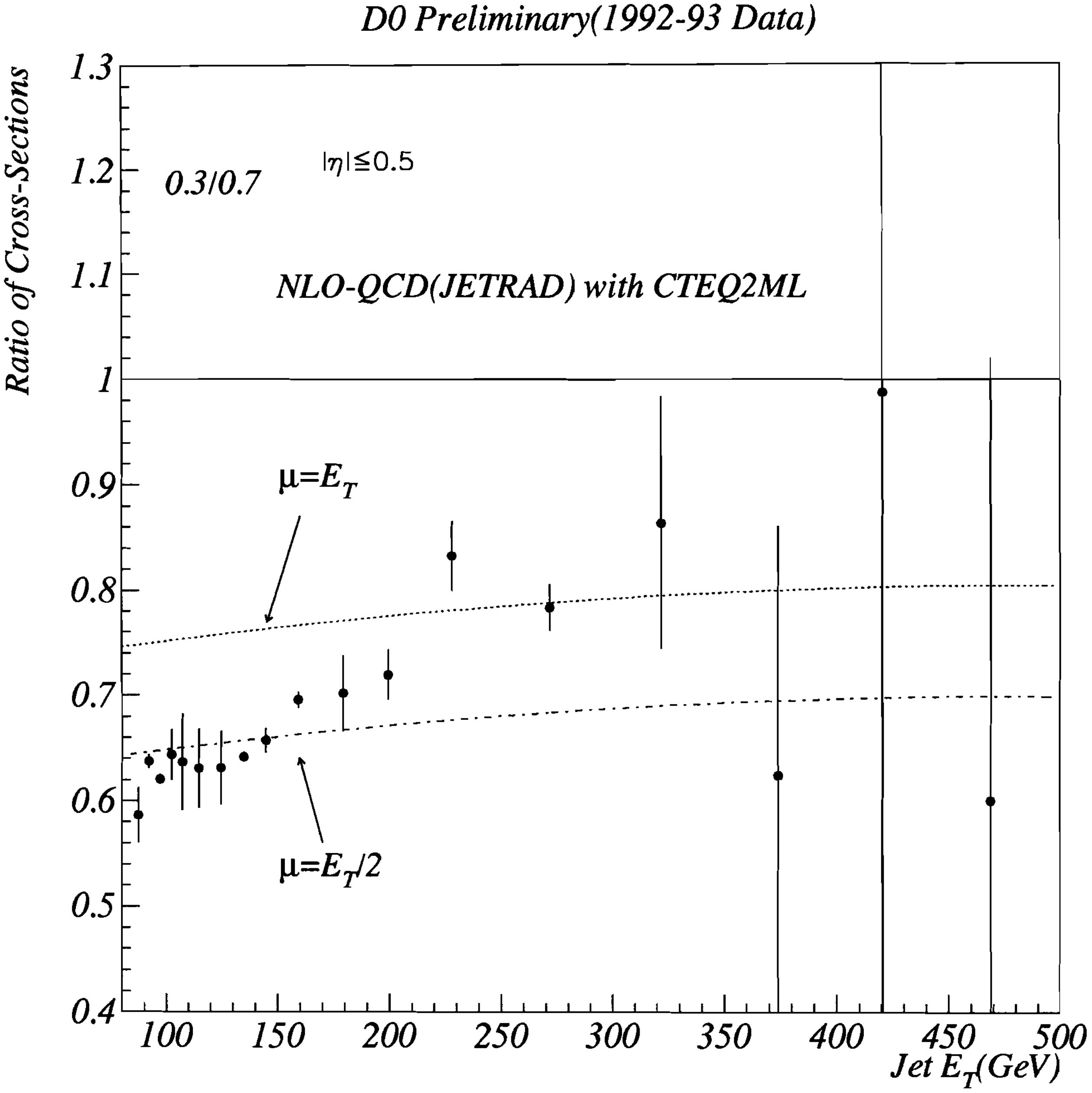

Figure 8.15: Ratio of Cross Section of 0.3 cone jets to that of 0.7 cone jets vs. Jet E_T in $|\eta| \leq 0.5$ compared to NLO QCD evaluated with CTEQ2ML pdf at two different values of μ scale, namely, E_T and $E_T/2$ of the leading jet in the event. Data prefers $\mu = E_T/2$.

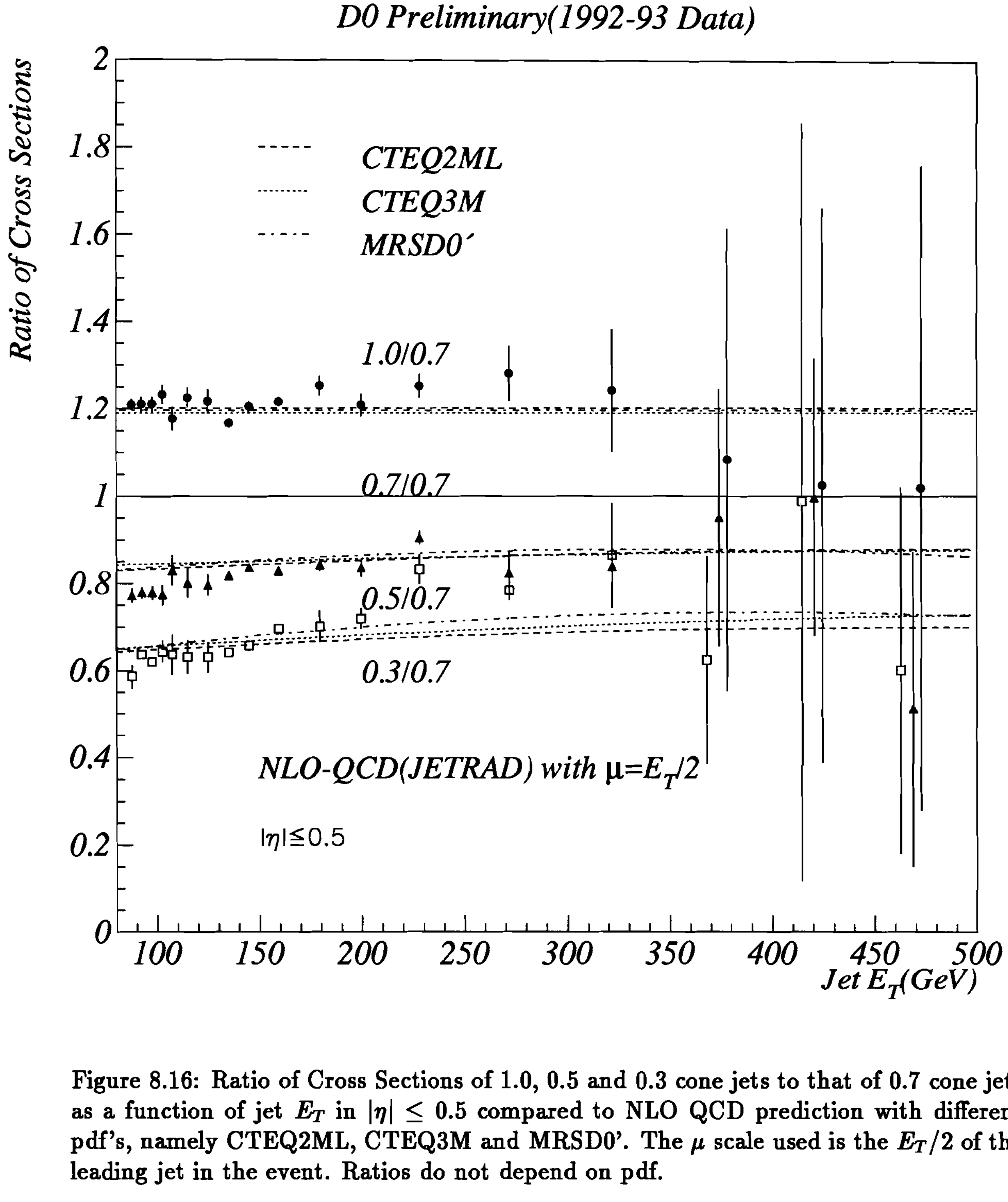

Figure 8.16: Ratio of Cross Sections of 1.0, 0.5 and 0.3 cone jets to that of 0.7 cone jets as a function of jet E_T in $|\eta| \leq 0.5$ compared to NLO QCD prediction with different pdf's, namely CTEQ2ML, CTEQ3M and MRSD0'. The μ scale used is the $E_T/2$ of the leading jet in the event. Ratios do not depend on pdf.

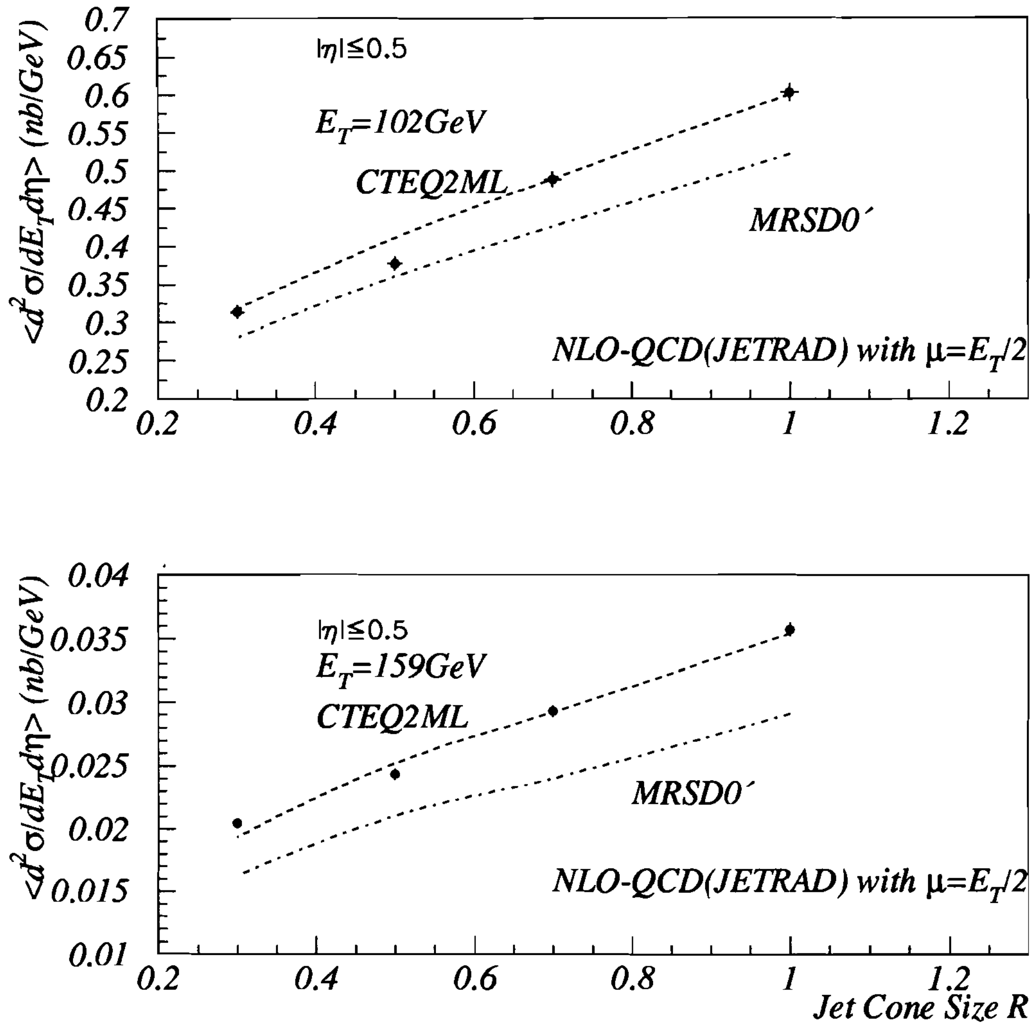

Figure 8.17: Cone size dependence of the inclusive jet cross section compared to NLO QCD (JETRAD) with CTEQ2ML and MRSD0' evaluated at $\mu{=}E_T/2$, given by the dotted lines, in $|\eta| \leq 0.5$ at a fixed E_T. **Top** plot is at 102 GeV and the **bottom** plot is at 159 GeV.

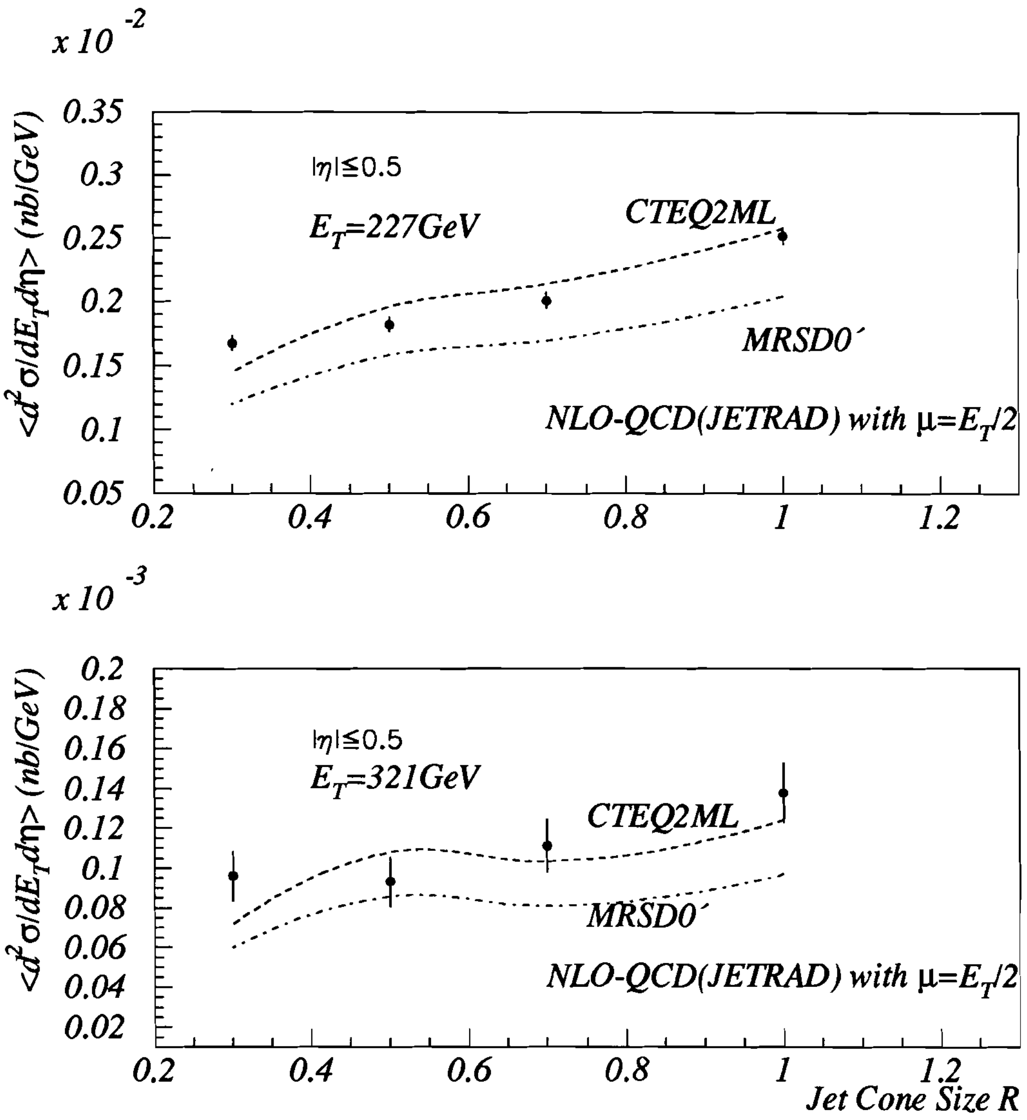

Figure 8.18: Cone size dependence of the inclusive jet cross section compared to NLO QCD(JETRAD) with CTEQ2ML and MRSD0' evaluated at $\mu = E_T/2$, given by the dotted lines, in $|\eta| \leq 0.5$ at a fixed E_T. Top plot is at 227 GeV and the bottom plot is at 321 GeV.

BIBLIOGRAPHY

[1] T. Akesson et. al. (AFS Collaboration), Phys. Lett. **B 123** 133(1983).

[2] J. Alitti et. al. (UA2 Collaboration), Phys. Lett. **B 257** 232(1991).

[3] F. Abe et. al. (CDF Collaboration), Phys. Rev. Lett. **61** 613(1988);
F. Abe et. al. (CDF Collaboration), Phys. Rev. Lett. **62** 613(1989);
F. Abe et. al. (CDF Collaboration), Phys. Rev. Lett. **68** 1104(1992);
F. Abe et. al. (CDF Collaboration), Phys. Rev. Lett. **70** 1376(1993).

[4] S. D. Ellis, Z. Kuntz, D. E. Soper, Phys. Rev. D **64** (1990).

[5] W. Giele, N. Glover, D. Kosower, Phys. Rev. Lett. **73** (1994) – JETRAD.

[6] F. Aversa et. al., Phys. Rev. Lett. **65** 401(1990).

[7] M. Bhattacharjee, G. C. Blazey *Inclusive Jet Cross Section as a Function of Jet Cone Size at DØ* , DØ internal note DØ 3128, (1996).

[8] F. Abe et. al. (CDF Collaboration), Phys. Rev. Lett. **77** 438(1996).

[9] J. D. Bjorken, Phys. Rev. **179**, 1547(1969); Phys. Rev. **163**, 1547(1967).

[10] A. Bodek et. al., Phys. Rev. **D20**, 1471(1979).

[11] R. D. Field, *Applications of Perturbative QCD,* Frontiers in Physics, Addison Wesley, (1989).

[12] V. D. Berger, R. J. Phillips, *Collider Physics,* Frontiers in Physics, Addison Wesley, (1987).

[13] J. Collins, D. Soper, G. Sterman *Factorization of Hard Processes in QCD,* Editor A. H. Mueller, Perturbative Quantum Chromodynamics, (1989).

[14] F. Halzen, A. Martin, *Quarks and Leptons,* John Wiley & Sons Inc., (1984).

[15] E. Levin, *Lectures at LAFEX, CBPF, Rio De Jenerio,* CBPF-NF-010/95, (1994).

[16] L. N. Lipatov, Sov. J. Nucl. Phys. **23**, 338(1976);
E. A. Kuraev, L. N. Lipatov, V. S. Fadin, Sov. Phys. JETP **44**, 443(1976); Sov. Phys. JETP **45**, 199(1977);
Ya. Ya. Balitsky, L. N. Lipatov, Sov. J. Nucl. Phys. **28**, 882(1978).

[17] D. E. Soper, *Jets and Partons,* Talk presented at 28th. International Conference on High Energy Physics, Warsaw, (1996).

[18] S. D. Ellis, Z. Kuntz, D. E. Soper, Phys. Rev. D **64** (1990).

[19] W. Giele, N. Glover, D. Kosower, Phys. Rev. Lett. **73** (1994) – JETRAD.

[20] B. Abbott, M. Bhattacharjee, V. D. Elvira, F. Nang, H. Weerts, *Fixed Cone Jet Defination at DØ and* R_{sep}, DØ internal note DØ 2885 (1996).

[21] J. Huth et. al., *Research Directions for the Decade, Snowmass 1990,* Editor E. L. Berger, World Scientific, Singapore, (1992).

[22] A. D. Martin et. al., Phys. Lett. B **306** 145(1993).

[23] J. Botts et. al., Phys. Lett. B **304** 159(1993), now superseded by CTEQ2, J. Botts et. al., (unpublished).

[24] H. L. Lai et. al., Phys. Rev. D **51** 4763(1995).

[25] FNAL, *A report of the design of the Fermi National Accelerator Laboratory superconducting accelerator,* FNAL internal note, (1979).

[26] FNAL, *Design Report Tevatron 1 Project,* FNAL internal note, (1984).

[27] Leon L. Lederman, *The Tevatron* Scientfic American, **263(3)**, (1991).

[28] M. P. Chruch et. al., *The antiproton source: Design and operation,* Ann. Rev. of Nucl. and Part. Sci., **43**, (1993).

[29] S. van der Meer et. al., *Physics and Techniques of Stochastic Cooling,* Physics Reports, **C58**, (1980).

[30] S. Abachi et. al., *The D0 Detector,* Nucl. Instr. and Meth. **A 338**, (1994).

[31] V. Radeka, IEEE Trans. Nucl. Sci. **21, No.1**, 51(1974).

[32] K. Kleinknecht *Detectors for Particle Radiation,* Cambridge University Press, (1987).

[33] S. Abachi et. al., Nucl. Instr. and Meth. **A324**, 53(1993).

[34] P. C. Bhat, FERMILAB-Conf-93/049-E, (1993).

[35] J. Bantly et. al., *The level-0 Trigger for the D0 Detector,* IEEE Trans. on Nucl. Sci. **41, 1274**, (1994).

[36] N. J. Hadley, *Cone Algorithm for Jet Finding,* D0 internal note D0 904, (1989).

[37] N. Amos et. al., *Luminosity Calculations for D0* , D0 internal note D0 2031, (1994).

[38] N. Amos et. al., *Change to the D0 Luminosity Monitoring Constant,* FERMILAB TM-1911, (1995).

[39] R. Rubenstein et. al., *Status of Fermilab E710,* FERMILAB Conf-93/216-E, (1993).

[40] V. D. Elvira, Ph.D. Thesis, Universidad de Buenos Aires, Argentina, (1995).

[41] R. V. Astur, *Study of Fake Jets in the D0 Detector,* D0 internal note D0 1662, (1993).

[42] M. Bhattacharjee, V. D. Elvira, G. C. Blazey, *Efficiencies of the Standard Jet Cuts for Cone Sizes: 0.3, 0.5, 0.7,* D0 internal note D0 2197, (1994).

[43] B. Abbott, G. C. Blazey, D0 internal note D0 1845, (1993).

[44] A. Milder, R. V. Astur, D0 internal note D0 1595, (1989).

[45] R. Kehoe, R. V. Astur, *Determination of the Hadronic Energy Scale of D0 Calorimetry,* D0 internal note D0 2908, (1996).

[46] U. Heintz, *A Measurement of the Calorimeter response Using π^0 Decays,* D0 internal note D0 2268, (1994);
I. Adam, *Observation of J/ψ to ee decays at D0 and calibration of the central electromagnetic scale,* D0 internal note D0 2298, (1994);
S. Rajagopalan, *An Estimate of the Energy Scale Offset at D0* , D0 internal note D0 2481, (1995).

[47] R. Hirosky, Ph.D. Thesis, University of Rochester, (1992).

[48] G. Marchesini et. al., Nicl. Phys. **B310**, (1988).

[49] S. Abachi et. al., Phys. Rev. Lett. **B 357** (1995).

[50] R. V. Astur et. al., D0 internal note D0 2135, (1994).

[51] T. Geld, D0 internal note D0 2474, (1995).

[52] V. D. Elvira, G. C. Blazey, M. Bhattacharjee, *Smearing Correction to the Jet Cross Sections,* D0 internal note D0 2247, (1994).

[53] M. Bhattacharjee, G. C. Blazey, R. Hirosky, *Jet Energy Resolution,* D0 internal note D0 2557, (1994).

[54] M. Bhattacharjee, Su Y. Choi, V. D. Elvira, S. Grinstein, R. Hirosky, *Jet Energy Resolutions,* D0 internal note D0 2887, (1996).